Eindhoven University of Technology

MASTER

Fabry-Perot interferometry : a proposal for a high-density plasma diagnostic

van de Kerkhof, M.A.

Award date:
1995

bewerking figuren

Summary

Radiofrequent discharges are widely used in industry, for the anisotropic etching of microstructures. A modern variant is the radiofrequent inductively coupled discharge (RFI), in which power is coupled into the plasma inductively. RFI plasmas feature a high electron density at low plasma pressures, and independently controlled low ion energies.

During this project a RFI plasma source has been built at the group EPG to gain more insight into the physical processes behind the generation of these plasmas. The main parameter of interest is the electron density, and the central focus of this project has been to develop an in situ electron density diagnostic.

For this purpose an infrared Fabry-perot interferometer has been designed, in which variations in electron density are measured through their effect on the refractive index of the plasma. The plasma is included in the optical cavity of the Fabry-Perot, and the entire interferometer is situated within the vacuum vessel. Because of the large separation of the mirrors, spherical mirrors were used. The effect of thermal and mechanical instabilities was reduced by mounting the mirrors on a solid Invar ring.
Using a wavelength of 5 μm, the Fabry-Perot is able to measure variations in the electron density below 10^{17} m^{-3}. This detection limit would be even lower for higher wavelengths, but the absorption within the reflecting gold coating of the mirrors tends to become prohibitive above 5 μm.

However, due to insuperable problems with the mirrors we did not succeed in realizing a working interferometer. Although this means no real experimental results can be presented, hopefully this project will serve as a basis for further research and as an introduction to Fabry-Perot interferometry.

Besides the building of the interferometer, work was also done on the plasma source itself. The source was adapted and installed, and some preliminary experiments were performed. The automatic tuning proved to be not fully reliable, even after optimizing all the control settings. Leaving the Farady shield out, we managed to create a plasma, although this was not inductively coupled, but capacitively. After installing the slotted Faraday shield to short out the capacitive field, the plasma glow became much brighter, indicative of an inductively coupled plasma.

10^{-4} cm^{-1} 5μ.

Contents

Part 3: Realization of the Fabry-Perot

Glossary of symbols and constants

optical symbols:

$\underline{E}$	electric field vector
$\underline{B}$	magnetic field vector
ε	dielectric constant, also called permittivity
ε_0	dielectric constant of vacuum
ε_r	relative dielectric constant
μ	magnetic permeability
μ_0	magnetic permeability of vacuum
μ_r	relative magnetic permeability
c	speed of light in vacuum; $c=1/(\varepsilon_0.\mu_0)$
n	refractive index
I	intensity of radiative energy
K	absorption coefficient
λ	wavelength
σ	wave number; $\sigma=1/\lambda$, also conductivity
$\underline{k}$	wave propagation vector
ν	frequency (Hz), also collision frequency
$\delta\nu$	frequency spread or bandwidth
ω	angular frequency (rad/s)
OPL	optical path length
τ	optical delay
$\underline{r}_i$	position vector relative to source i
ε_i	epoch angle of source i
δ	phase difference
$\underline{P}$	polarization
α	polarizability
γ	damping coefficient

properties of multiple-beam interferometers:

T	transmittance of the reflecting surfaces
R	reflectance of the reflecting surfaces
A	absorption of the reflecting surfaces
d	separation between the surfaces
θ	angle of incidence
F	coefficient of finesse
$A(\delta)$	Airy function
C	contrast ratio
F	finesse
F_r	reflectivity finesse
$(\Delta\lambda)_{FSR}$	free spectral range
$(\Delta\sigma)_{FSR}$	free spectral range
$\delta\lambda_{1/2}$	half-width at half maximum of fringe
$\delta_{1/2}$	half-width at half maximum of Airy peak
R_0	resolving power
ρ_s	maximum mirror aperture

plasma properties

v	particle velocity
T	temperature
E_k	particle kinetic energy
λ_D	Debye length
ω_{pe}	electron plasma frequency
ω_{pi}	ion plasma frequency

Fundamental physical constants

(taken from CRC94)

speed of light in vacuum	c	299792458	ms^{-1}
permeability of vacuum	μ_0	$4\pi.10^{-7}$	NA^{-2}
permittivity of vacuum	ε	$8{,}8541878.10^{-12}$	Fm^{-1}
elementary charge	e	$1{,}6021773.10^{-19}$	C
electron mass	m_e	$9{,}1093897.10^{-31}$	kg
proton mass	m_p	$1{,}6726231.10^{-27}$	kg
atomic mass unit	u	$1{,}6605402.10^{-27}$	kg
Boltzmann constant	k	1,380658.10_23	~~$Wm^{-2}K^{-4}$~~ bij σ

1 Introduction

Radiofrequent (RF) discharges have been used in industry since the early 1970s for the etching of integrated circuits and other microstructures. Nowadays, structures with dimensions below 1 μm can be etched anisotropically using RF plasmas. The pace of the developments and the competitiveness of the business have forced many etching processes into production before the physics behind them was fully understood. Arguably, with such a heuristic approach, these techniques are not used to their full potential, and a more fundamental understanding of the relevant plasma physics and processes is still required.
At this moment, there is a trend in industry to switch from capacitively coupled to inductively coupled plasmas, which feature a higher electron density and allow for independent control of the ion energy (*hopwood92*).

In the group Elementary Processes in Gas Discharges (EPG) at the Department of Physics at the Eindhoven University of Technology, a radiofrequent inductive (RFI) plasma source is being built, in order to attain a more thorough understanding of the inductive power coupling mechanisms.

The main parameter of interest is the free electron density, and experiments are to be conducted to monitor the effect of several parameters, such as power level, pressure, gas composition on the electron density. For this, a fast and non-intrusive diagnostic is required.
The electron density can be deduced from the refractive index of the plasma. The effect of electron density on the refractive index increases with the wavelength, indicating use of long wavelength light for electron densities of order 10^{17} m^{-3}. Variations in the index of refraction can be measured to great precision by an interferometer.

The central focus of this graduation project was to design and implement an infrared Fabry-Perot interferometer as an in-situ diagnostic for the free electron density. Because the separation of the mirrors is large, they should be spherical in shape, and they should be placed at their confocal separation. The mechanical construction should be insensitive to vibrations and thermal instabilities.

Furthermore, a lot of effort has gone into the realization of the plasma source itself, on which I have worked with David Vender. The power generator and the matching network have been adapted and installed, and some preliminary experiments have been performed to get acquainted with the computer control of the vacuum system and the generation of plasma. The settings of the matchbox control have also been optimized.

The first part of this thesis consists of a discussion of electromagnetic wave propagation and dispersion processes in plasmas in chapter 2, and a discussion of interferometry in chapters 3 and 4. Chapter 3 provides a global overview of interferometry, while chapter 4 concentrates on Fabry-Perot interferometers. Several geometries of the Fabry-Perot are described, and a discussion of the effect of mirror imperfections and misalignment is included.

In the second part, etching plasmas are discussed in chapter 5, and the experimental set-up in chapter 6. Chapter 6 also contains the experiments on the vacuum system and the plasma source.

The third part consists of a discussion on the practical considerations for the interferometer design in chapter 7, and a discussion of what went wrong in practice in chapter 8.
Chapter 9 contains the concluding remarks, along with some suggestions for further research.

The reader is assumed to have a basic understanding of optics. The standard works of Hecht (*hecht79*) and Born and Wolf (*born75*) are recommended for a more comprehensive discussion of the concepts underlying dispersion and interferometry.

2 Propagation of light and dispersion

In this chapter the theoretical background of interferometry as a plasma diagnostic is given. Section 2.2 discusses the physical processes underlying dispersion and section 2.3 deals with the application of dispersion as a plasma diagnostic tool. In section 2.3 some practical considerations of appropriate wavelength and parasitic dispersive effects of the plasma are also given. Firstly, the relevant optical concepts are introduced in section 2.1.

2.1 Wave equations and index of refraction

Light can be represented as an electromagnetic wave phenomenon, and as such its propagation and its interaction with matter is described by the Maxwell equations. The intensity of the light follows from the amplitude of the electromagnetic fields and its wave characteristics are given by its frequency ω and its propagation number k. Instead of the propagation number, the wavelength $\lambda=2\pi/k$ is often used. In the optical range the wavelength corresponds with a certain color. I.e. light of λ=400 nm is equivalent to violet light, while λ=600 nm corresponds to red light.

Electromagnetic fields are described fully by the Maxwell equations. In vacuum, away from charges and currents, the time dependent Maxwell equations can be written as (*jackson75*):

$$\nabla^2\overline{E} - \varepsilon_0\mu_0\frac{\partial^2\overline{E}}{\partial t^2} = 0 \qquad (2.1)$$

and

$$\nabla^2\overline{B} - \varepsilon_0\mu_0\frac{\partial^2\overline{B}}{\partial t^2} = 0 \qquad (2.2)$$

These are wave equations, solutions of which are harmonic plane waves:

$$\overline{E}(\overline{r},t) = \overline{E}_0.\exp(i\overline{k}.\overline{r}-i\omega t) \qquad (2.3)$$

and

$$\overline{B}(\overline{r},t) = \overline{B}_0.\exp(i\overline{k}.\overline{r}-i\omega t) \qquad (2.4)$$

The frequency ω and the propagation number k are related by $k^2=\varepsilon_0\mu_0\omega^2$. The plane wave propagates in the direction of $\underline{k}$ with phase velocity:

$$v = \frac{\omega}{k} = \frac{1}{\sqrt{\varepsilon_0\mu_0}} \equiv c \qquad (2.5)$$

However, these plane waves are only solutions to all the Maxwell equations if both the electric and the magnetic field are perpendicular to the propagation vector: electromagnetic waves are transversal.

The net effect of a medium on an electromagnetic wave is a change of the permittivity and the permeability in the Maxwell equations: $\varepsilon=\varepsilon_r\varepsilon_0$ and $\mu=\mu_r\mu_0$. Within the medium the phase velocity of the waves will be:

$$v = \frac{1}{\sqrt{\varepsilon\mu}} \tag{2.6}$$

The absolute index of refraction *n* of a medium is defined as the ratio of the phase velocity of the electromagnetic wave in vacuum to that in the medium:

$$n \equiv \frac{c}{v} = \sqrt{\varepsilon_r\mu_r} \tag{2.7}$$

Except for paramagnetic materials, for most media the change in magnetic permeability will be negligible, $\mu_r=1$, and *n* will depend only on the relative dielectric constant ε_r:

$$n = \sqrt{\varepsilon_r} \tag{2.8}$$

The index of refraction plays a crucial role in geometrical optics, as it governs the way a beam of light is affected by a transition between two media. It determines the angle of refraction in Snell's law, as well as the reflectivities and transmissivities in the Fresnel equations.
The wavelength inside a medium is also a function of *n*, through the relation between wavelength and frequency: $\lambda=2\pi/k=(2\pi nc)/\omega$. To satisfy continuity requirements (*hecht79*), the frequency must be the same in every medium as it is in vacuum, so within a medium of refractive index *n* the wavelength decreases by a factor *n*: $\lambda=\lambda_0/n$.

This means that for a medium of higher refractive index, more waves fit into a given length. The optical path length (O.P.L.) is defined as the spatial path length times the index of refraction. If the light traverses a path along which the index of refraction changes gradually, we get an integral representation for the O.P.L.:

$$O.P.L. = \int n(s)\,ds \tag{2.9}$$

2.1.3 Conduction, absorption and attenuation

If the medium contains charges, that are able to move around within the medium, the Maxwell equations have to be modified to include charge and current effects on the electric and magnetic fields. This is the case for conducting media like metals or plasmas. Both metals and plasmas however are quasi-neutral: the positive and negative charges cancel each other out over a macroscopic volume. This means no net charge is present and only currents have to be taken into account.

The current is proportional to the electric field:

$$\bar{J} = \sigma\bar{E} \tag{2.10}$$

with σ the ohmic conductance of the medium, and the wave equations now become:

$$\nabla^2\bar{E} - \varepsilon\mu\frac{\partial^2\bar{E}}{\partial t^2} - \mu\sigma\frac{\partial\bar{E}}{\partial t} = 0 \tag{2.11}$$

and

$$\nabla^2\bar{B} - \varepsilon\mu\frac{\partial^2\bar{B}}{\partial t^2} - \mu\sigma\frac{\partial\bar{B}}{\partial t} = 0 \tag{2.12}$$

A real metal or plasma will have a finite conductance, because the moving charges undergo collisions, in which electromagnetic energy is irreversibly dissipated. This absorption of energy from the field is expressed by the damping term in the wave equation, leading to an imaginary component in the propagation vector:

$$\bar{k} = \bar{k}_I + i\bar{k}_{II} \tag{2.13}$$

The solution to these wave equations are attenuated plane waves:

$$\bar{E} = \bar{E}_0.\exp(-\bar{k}_{II}.\bar{r})\exp(i\bar{k}_I.\bar{r}-i\omega t) \tag{2.14}$$

and

$$\bar{B} = \bar{B}_0.\exp(-\bar{k}_{II}.\bar{r})\exp(i\bar{k}_I.\bar{r}-i\omega t) \tag{2.15}$$

The intensity of light is defined by:

$$I = \varepsilon v<|\bar{E}|^2> \tag{2.16}$$

The intensity decays exponentially as the light propagates through the medium, with an absorption coefficient K=2k$_{II}$:

$$I(d) = I_0\exp(-Kd) \tag{2.17}$$

where I_0 is the intensity at the interface and d is the distance traveled within the medium. The distance corresponding to a reduction in intensity of e^{-1} is called the skin depth. For strongly absorbing media, the skin depth can be extremely small. Gold for example, has k_{II}=4,1.10^6 m^{-1} for HeNe laser light (632,8 nm), and its penetration depth is 0,12 μm, which is a fraction of the wavelength.

So far, the permittivity of the medium has been taken to be real. As we shall see in the next section however, in an absorbing medium it will have an imaginary part, representing finite conduction as well as other energy loss processes. A complex permittivity leads to an imaginary component in both the refractive index and the propagation vector.
Under normal conditions, Im(ε)>0, the amplitude of the electromagnetic fields will decrease, and the wave will be attenuated. In a laser cavity on the other hand, Im(ε)<0. The medium then gives off energy to the field, and the wave will be amplified.

In optical literature, the refractive and absorbing properties of a medium are usually expressed by specifying the real and imaginary parts of the refractive index. The absorption coefficient can be computed from the imaginary part of *n* by:

$$K = \frac{2\omega}{c}\,\mathrm{Im}(n) \tag{2.18}$$

2.2 Dispersion: physical processes

Dispersion is defined as the dependence on frequency of material properties, like conductance, permittivity and the index of refraction. If the permittivity of the medium is a function of frequency, the medium is called dispersive. We have to consider the Maxwell equations for each frequency individually, by splitting the electric and magnetic fields into their Fourier components. This gives the Helmholtz equations:

$$\nabla^2\overline{E} - \varepsilon\mu\omega^2\overline{E} = 0 \tag{2.19}$$

and

$$\nabla^2\overline{B} - \varepsilon\mu\omega^2\overline{B} = 0 \tag{2.20}$$

which yield a plane wave solution for each separate frequency, and the total wave is a superposition of all frequency components.
Each frequency component will have its own phase velocity

$$v(\omega) = \frac{\sqrt{\varepsilon_r(\omega)}}{c} \tag{2.21}$$

so the wave profile will distort as its propagates through a dispersive medium.

Every medium (except total vacuum) is dispersive to a greater or lesser degree, because the physical processes which determine the permittivity are frequency dependent. These processes will be discussed in the following sections.

2.2.1 Polarization processes

A gas is essentially a collection of individual neutral molecules or atoms, which move freely with a thermal distribution. Although the atoms as a whole are electrically neutral, they consist of a positively charged nucleus surrounded by a negative cloud of bound electrons.
In a molecule, several atoms are chemically bonded. If one atom is more electronegative than the other, it exerts a somewhat higher attraction on the electrons, and it will become slightly negatively charged with respect to the other atom. The molecule as a whole remains neutral.

If an electromagnetic field is applied, the internal charge structure of the gas particles will be changed because of the force exerted by the electric field. Forces arising from the associated magnetic field are generally negligible, as B=E/c. The redistribution of internal charges by the electric field corresponds to the generation of electric dipole moments, which in turn contribute to the total internal field. For normal isotropic media the polarization is given by:

$$\overline{P} = (\varepsilon - \varepsilon_0)\,\overline{E} \tag{2.22}$$

This expression is correct for rarefied media, like gases or plasmas. For dense media it needs to be corrected, as the induced field of neighbouring atoms will moderate the electric field locally.

The gas molecules interact with the electric field by way of the following mechanisms:

- electronic polarization of bound electrons.
- ionic polarization of asymmetric molecules.
- orientational polarization of polar molecules.

The applied field will distort the electron cloud of the atoms in the gas, shifting it relative to the nucleus to produce an induced dipole moment. This effect is called electronic polarization. Electronic polarization is experienced by all atoms in the gas, also when they are ionized or part of a molecule.
Asymmetric molecules will experience an additional effect, called ionic or atomic polarization. Here a dipole moment is induced by a shift of the electropositive and the electronegative constituent atoms with respect to each other. This effect does not occur for symmetric molecules like O_2 or N_2.
Another molecular effect is the alignment of polar molecules by the electric field. Polar molecules possess a permanent dipole moment, due to an asymmetrical sharing of valence electrons. The individual dipoles are randomly orientated, because of thermal agitation. With the introduction of an electric field however, the dipoles are (partially) aligned and the gas takes on an orientational polarization.

A plasma can be considered as a gas with an appreciable density of charged particles. The charged particles can be free electrons, atomic ions and molecular ions. These charged particles interact with the electric field through the Coulomb force. Because of their large mass difference we will distinguish between the free electrons and the ions.

The interaction of the electromagnetic wave with the ions and free electrons is much stronger than that with the neutral particles. In plasmas with a low degree of ionization however, the number of charged particles is small with respect to the number of neutrals, and it will not be clear a priori, which polarization effect determines the response of the plasma as a whole.

2.2.2 Time-varying electromagnetic fields

Light is an electromagnetic field, varying harmonically in time. When such a time-varying field passes through a medium it will exert a time-varying force on the atoms, molecules, ions and electrons. However, molecules, atoms (and ions) are relatively heavy objects and have appreciable moments of inertia. At high driving frequencies therefore they will be unable to follow the rapid variations of the field and their contribution to the total polarizability will drop markedly.
In contrast, electrons have little inertia and can follow the field variations even at optical frequencies (about 10^{15} Hz). For bound electrons however, matters will be complicated by the binding force between the electron and the nucleus.

It is obvious, that the relative contribution of different polarization mechanisms is a function of the frequency or wavelength of the light. We will confine our present discussion to light with a wavelength in the range of the near infra-red to the red, corresponding to frequencies of the order of 10^{14} Hz. In this frequency range the only polarization process of interest is electronic (or ionic) polarization. In a plasma or metal, perturbations of the distribution of charged particles also contribute to the polarization.

2.2.3 Electronic polarization

A rigorous theory of the interaction between electromagnetic waves and matter at the atomic level should be founded on quantum mechanics. We will instead use a classical treatment, which yields essentially similar results. In this classical model, the bound electrons are assumed to move in a harmonic potential, with a restoring force $F_{osc}=-m_e\omega_0^2$, where ω_0 is the natural frequency of the oscillator. When a harmonically varying electric field is applied, the electron will experience a force $F_{el}=-eE$. Here the magnetic force is again neglected. Assuming an additional phenomenological damping term, the equation of motion becomes:

$$m_e\left[\frac{d^2}{dt^2}\bar{r}+\gamma\frac{d}{dt}\bar{r}+\omega_0^2\bar{r}\right] = -e\bar{E}(\bar{r},t) \qquad (2.23)$$

with damping constant γ. Solving this differential equation yields an expression for $\underline{r}(t)$:

$$\bar{r}(t) = \frac{-e/m_e}{\omega_0^2-\omega^2-i\gamma\omega}\,\bar{E}(t) \qquad (2.24)$$

And the dipole moment due to this one electron will be:

$$\bar{p}(t) = -e\bar{r} = \frac{e^2/m_e}{\omega_0^2-\omega^2-i\gamma\omega}\,\bar{E}(t) \qquad (2.25)$$

Within each atom the electrons are arranged in shells, with a different binding force for each shell. Thus not all electrons will have the same natural frequency. The phenomenological damping term too can vary.

Assume the number density of the medium is N molecules (or atoms) per unit volume, each containing f_j electrons with ω_{0j} and γ_j. f_j is called the oscillator strength; Σf_j is the number of electrons per molecule.

The total electronic polarization now becomes:

$$\bar{P}(t) = \frac{Ne^2}{m_e}\sum_j\frac{f_j}{\omega_{0j}^2-\omega^2-i\gamma_j\omega}\bar{E}(t) \qquad (2.26)$$

And the permittivity of the medium is:

$$\varepsilon(\omega) = \varepsilon_0+\frac{Ne^2}{m_e}\sum_j\frac{f_j}{\omega_{0j}^2-\omega^2-i\gamma_j\omega} \qquad (2.27)$$

A quantum-mechanical approach would have yielded this same result, with merely a different interpretation of the terms: ω_{0j} would be the characteristic frequency of an atomic excitation, and $f_j/\Sigma f_j$ the corresponding transition probability.

Using the relation $n^2=\varepsilon_r$, we find the dispersion relation:

$$n^2(\omega) = 1+\frac{Ne^2}{\varepsilon_0 m_e}\sum_j \frac{f_j}{\omega_{0j}^2-\omega^2-i\gamma_j\omega} \tag{2.28}$$

The damping constant is generally small compared to the natural frequencies. The index of refraction is thus approximately real, except for those regions where the frequency approaches a natural frequency. At resonance $\omega^2-\omega_{0j}^2=0$, only the damping term remains for the j-th term, and the term will become large and purely imaginary. The damping constant γ is a positive entity, so Im(ε) too will be positive, corresponding to absorption of electromagnetic energy. These frequency regions are called regions of resonant absorption, or absorption bands.
If the light frequency lies far below the lowest natural frequency, $\omega^2<<\omega_{0j}^2$, and ω can be neglected. The index of refraction is then essentially constant and little dispersion is observed.

The theoretical derivation of the dispersion equation above contains some idealisations, which need to be corrected for in real gases or plasmas. In practice therefore, often experimental values of the atomic and molecular polarizability from reference books are used to compute the effect of the bound electrons on the refractive index. These values are listed in reference works like the Handbook of Chemistry and Physics (*CRC95*), but care should be taken about the different units used. In this thesis the SI unit, $CV^{-1}m^2$ will be adopted. The polarizability of unlisted molecules can be estimated by combining the polarizabilities of its constituent electron groups (*sanders85*).

The polarizability is related to the dielectric constant by:

$\vec{P} = N\alpha\vec{E}$ $\quad \vec{P} = \varepsilon_0\chi\vec{E}$ $\quad \chi \geq$

$$N\alpha = \varepsilon-\varepsilon_0 \tag{2.29}$$

$= \varepsilon_0(\varepsilon_r - 1) = \varepsilon_0\varepsilon_r - \varepsilon_0 = (\varepsilon_q - \varepsilon_0)$

with N the number density of atoms and molecules. If the gas contains more than one species, or if several excited states exist, the polarizabilities of all these different states and species must be taken into account.
The refractive index in terms of polarizability is:

$$n^2 = 1+\frac{1}{\varepsilon_0}\sum_j N_j\alpha_j \tag{2.30}$$

where N_j is the density of each specific state and species. For small deviations this can be approximated by:

$$n = 1+\frac{1}{2\varepsilon_0}\sum_j N_j\alpha_j \tag{2.31}$$

In this formula the static polarizability is used, which is valid for the low frequency limit, $\omega^2<<\omega_{0j}^2$. If the frequency approaches the lowest natural frequency, a correction factor needs to be applied:

$$\alpha(\omega) = \frac{\alpha_0}{1-(\frac{\omega}{\omega_{0j}})^2} \tag{2.32}$$

In many plasmas of interest, one species will often be predominant, along with its associated ion. The equation for the refractive index then reduces to:

$$n = 1+\frac{\alpha_x}{2\varepsilon_0}N_x+\frac{\alpha_i}{2\varepsilon_0}N_i \tag{2.33}$$

In this we have assumed all particles to be in the ground state. In many plasmas however this does not hold. Ionization and recombination processes leave ions and atoms in excited states; they return to the ground state mostly by collisions. At low pressures and high temperatures, collisions are much less frequent than ionization and recombination processes, and the excited states will be densely populated (*baum75*).
Generally, the polarizabilities of the excited atoms or molecules will be larger than the ground state polarizabilities, and their effect on the resulting polarizability will be significant in low-pressure plasmas (*sanders85*).

2.2.4 Ionic polarization

By analogy to the electron model given above, ionic polarization can be described by considering the atoms within a molecule to resemble harmonic oscillators. The frequencies ω_{0j} would then be the characteristic frequencies of the rovibrational levels of the molecule, and the electron mass is replaced by the much larger ion mass. With N again the number density of molecules and Σf_j the number of atoms the dispersion equation becomes:

$$n^2(\omega) = 1 + \frac{Ne^2}{\varepsilon_0 m_i} \sum_j \frac{f_j}{\omega_{0j}^2 - \omega^2 - i\gamma_j \omega} \tag{2.34}$$

As the ion mass is 3 to 5 orders higher than the electron mass, electronic polarization will be predominant, and ionic polarization will only significantly affect the refractive index in its regions of resonance.
For most molecules the natural frequencies lie in the infrared, and ionic polarization causes many materials that are transparent in the visible range to become opaque in the infrared. This means for instance that glass or quartz cannot be used for optical elements at wavelengths above 2 µm (*optics guide 5, melles griot*). Ionic polarization of ozon molecules is also the mechanism which shields the earth's population from harmful solar UV radiation.

2.2.5 Free electrons

In a plasma, ionization processes create a number of free electrons, which can move freely through the plasma unbound to any nucleus. The difference with bound electrons within an atom is that these free electrons have no binding force, so $\omega_0=0$, and there are no resonances. Damping occurs because of collisions of the electrons with other particles, and the damping constant γ is equal to the total electron collision frequency ν. The permittivity then becomes:

$$\varepsilon(\omega) = \varepsilon_0 - \frac{N_e e^2}{m_e(\omega^2 + i\nu\omega)} \tag{2.35}$$

with N_e the free electron density. The dispersive equation becomes:

$$n^2(\omega) = 1 - \frac{N_e e^2}{\varepsilon_0 m_e} \frac{1}{\omega^2 + i\nu\omega} \tag{2.36}$$

For high frequencies the effect of collisions can be neglected and the dispersive equation simplifies to:

M

$$n^2(\omega) = 1 - \left(\frac{\omega_p}{\omega}\right)^2 \tag{2.37}$$

where we have introduced the plasma frequency ω_p (also called the cut-off frequency):

$$\omega_p^2 = \frac{N_e e^2}{\varepsilon_0 m_e} \tag{2.38}$$

For frequencies below the plasma frequency, the refractive index and the propagation number become purely imaginary: the amplitude of the electromagnetic field falls off exponentially and light incident on the plasma will be totally reflected.

When using light to probe a plasma, the plasma frequency sets a lower limit on the probe frequency, or equivalently an upper limit to the wavelength, which is given by:

$$\lambda_{max}^2 = \frac{(2\pi c)^2 \varepsilon_0 m_e}{N_e e^2} \tag{2.39}$$

Conversely, for any particular probing wavelength there is a critical density, above which the probing beam cannot propagate through the plasma and will be reflected:

$$N_{ec} = \frac{(2\pi c)^2 \varepsilon_0 m_e}{e^2 \lambda^2} \tag{2.40}$$

2.2.6 Free ions

The positively charged ions respond to the electric field much like free electrons. However, due to their large masses, their contribution to the index of refraction will be negligible. This remains true over the entire frequency range, as free ions do not have any resonant frequencies. Of course, the ions still display electronic polarization effects. the internal charge structure will however be changed by the missing electron(s). The polarizability of an ion will therefore be higher than that of its corresponding atom.

2.3 Dispersion as an electron density diagnostic

2.3.1 Free electron contribution vs atomic polarization

In the previous section we saw that the free electron density influences the refractive index of a plasma. Conversely, measurement of the refractive index, can yield the electron density. In fact, this is considered to be the most suitable technique for determining N_e (*hutchinson87*).
However, the refractive index depends not only on N_e, but also on the neutral atoms and ions in the plasma. As discussed in the previous section, free electrons result in a lowering of the refractive index. Bound electrons on the other hand have their lowest natural frequencies in the ultraviolet, leading to a positive change in refractive index for optical frequencies. The net effect depends on the ionization degree, the polarizability and the probe wavelength.
Note: for wavelengths in the infrared region care must be taken to avoid molecular resonance bands, as these will give rise to strong absorption in the plasma.

If the wavelength is large enough (far red and beyond) the atomic contribution is approximately constant:

$$(n-1)_{at} = \frac{1}{2\varepsilon_0}\sum_j N_j\alpha_j \qquad (2.41)$$

with the summation over all the possible excitation and ionization states of the atoms in the plasma; $N_{at}=\Sigma N_j$ is the density of atoms and ions combined. The free electron contribution on the other hand, shows considerable dispersion:

$$(n-1)_{el} = -\frac{e^2}{8\varepsilon_0 m_e c^2\pi^2}\lambda^2 N_e \approx (4{,}485.10^{-16})\,\lambda^2 N_e \qquad (2.42)$$

with N_e the electron density.

$$\Delta n = (4{,}485.10^{-16})\lambda^2 N_e \cdot \frac{2\pi}{\lambda}$$

The ratio between the electron and atomic contributions is proportional to λ^2, the ionization degree N_e/N_{at} and inversely proportional to the atomic polarizabilities. However, for a given plasma, only the wavelength can be varied, and a large wavelength should be used to measure the electron density.

To illustrate this effect, we look at an argon plasma. Assuming excitation and ionization effects on the atomic polarizability can be ignored, the atomic contribution becomes:

$$(n-1)_{at} = \frac{\alpha_{Ar}}{2\varepsilon_0}N_{at} \qquad (2.43)$$

With $\alpha_{Ar}=1{,}8.10^{-40}$ CV^{-1}m^2 (*CRC94*) and for a typical ionization degree of 10%, the atomic contribution will be less than 1% of the electronic contribution for

$$\lambda \geq \sqrt{100.\frac{(2\pi c)^2 m_e\alpha_{Ar}}{e^2}.\frac{N_{at}}{N_e}} \approx 4{,}8\,\mu\text{m} \qquad (2.44)$$

The electron density of this particular plasma can thus be deduced directly from a measurement of the refractive index with a 5 μm diode laser.

Measurement of the refractive index of a plasma is usually done by interferometry, where the change in the optical path length through the plasma is measured, or equivalently the phase shift. In a Mach-Zehnder interferometer the phase shift $\Delta\phi$ due to a variation in the electron density Δn will be:

$$\Delta\varphi = \frac{2\pi}{\underset{me}{\lambda}}\int_L \Delta n(x)\,dx \approx (-2{,}818.10^{-15})\,\lambda\int \Delta N_e(x)\,dx \qquad (2.45)$$

In such an experiment, the line-integrated electron density along a chord is measured, instead of the true local density. In combination with an appropriate plasma model however, this average line density can still be used meaningfully to monitor the electron density.

3

5,636 10 · λ

2.3.2 Wavelength considerations

In the previous section it was demonstrated that the probe wavelength should be high, in order to reduce the relative effect of the atomic contribution on the refractive index.

Furthermore, there is another reason for using large wavelengths: small wavelengths are more sensitive to vibrations and thermal instabilities, and require a very high mechanical stability.
In a Michelson interferometer for instance, displacement of one of the mirrors by d introduces a phase shift $\Delta\phi_{mech}=4\pi d/\lambda$, which can not be distinguished from a phase shift due to a change in electron density $\Delta\phi_{el}=-(5,636.10^{-15})\lambda\Delta N_e$. The sensitivity of this interferometer to mechanical instabilities is thus inversely proportional to the square of the wavelength.
Even if the vibrational stability is of the order of 0,1 nm, which is feasible (*kroesen91*), a wavelength of 100 µm is required to measure a change in electron density of 10^{17} m^{-3}.
Lower probe wavelengths require some form of modulation to separate the electron density effect from thermal and vibrational effects. The most widely used modulation techniques are frequency modulation and pulsing of plasma power.

The problem of mechanical stability is largely avoided when working with microwaves, but then the spatial resolution is lost: only the average electron density can be deduced.
Using visible or infrared light allows measurement of the average electron density along a chord. The radial density profile can be deduced from measurements over a set of chords by Abel inversion (*hutchinson87*). For continuous monitoring of the density profile a multi-channel set-up can be used (*luhmann84*)

Aside from the spatial resolution, a fundamental upper limit to the wavelength of the probe comes from the plasma frequency of the electrons:

$$\lambda_{max} = \sqrt{\frac{2\pi c\,\varepsilon_0 m_e}{N_e e^2}} \approx (3,34.10^7)\,/\sqrt{N_e} \qquad (2.46)$$

In an etching plasma, $N_e<10^{20}$, corresponding to a maximum wavelength in the microwave region: $\lambda_{max}\approx 3$ mm

3cm kan ook wel.

Not really fundamental, but often more troublesome, are the problems in optical technology at very high wavelengths in the infrared: most transparent materials are opaque above a few microns, and few suitable laser sources are available for the far infrared.
The main problem however lies in the infrared detectors. A higher wavelength means a lower photon energy, which is harder to distinguish from thermal noise. A typical liquid nitrogen cooled Germanium detector has a detection limit of about 20 µm.

If the electron density is very high, as for thermonuclear plasmas, refraction by the plasma will become a problem at high wavelengths. The plasma acts like a negative lens because of radial density gradients in the plasma, and the probe beam will be somewhat deflected. If the deflection angle is too large, the beam will not pass through the apertures anymore. As the deflection is proportional to the wavelength, this sets an upper limit on the wavelength.
In etching plasmas however, the density remains relatively low and refraction effects can be neglected.

2.3.3 Separating the atomic and electronic contributions

If the electronic and atomic contributions are of the same magnitude, their separate effects can be isolated by measuring the refractive index of the plasma at two different wavelengths. Each wavelength yields a different refractive index, because the electron contribution is strongly wavelength dependent, and the atomic contribution is approximately constant.
Assuming quasineutrality $N_i=N_e$, and neglecting the effect of excited states the refractive indexes are given by:

$$(n-1)_{\lambda_1} = \left(\frac{\alpha_a}{2\varepsilon_0}N_a + \frac{\alpha_i}{2\varepsilon_0}N_e\right) - (4,485.10^{-16})\,\lambda_1^2 N_e \qquad (2.47)$$

and:

$$(n-1)_{\lambda_2} = \left(\frac{\alpha_a}{2\varepsilon_0}N_a + \frac{\alpha_i}{2\varepsilon_0}N_e\right) - (4,485.10^{-16})\,\lambda_2^2 N_e \qquad (2.48)$$

with α_a and α_i the polarizability of respectively the neutral and ionized atoms.
Solving these equations, yields the electron density N_e:

$$N_e = \frac{(n-1)_{\lambda_2} - (n-1)_{\lambda_1}}{(4,485.10^{-16})\,(\lambda_2^2 - \lambda_1^2)} \qquad (2.49)$$

A scheme for this, utilizing the two wavelengths of a HeNe laser (λ_1=632,8 nm, λ_2=3,3912 μm), is outlined in the Ph.D. thesis of Rosado (*rosado81*).
Rosado used this technique to obtain the electron and atomic densities in an Argon plasma, from interferometric measurement of the refractive index. Argon has polarizabilities α_a=1,83.10^{-40} CV^{-1}m^2 and α_i=1,15.10^{-40} CV^{-1}m^2 (*rosado81)*.
Inserting these numerical values, we get:

$$(n-1)(\lambda_1) = (1,03.10^{-29})N_a - (1,73.10^{-28})N_e \qquad (2.50)$$

and:

$$(n-1)(\lambda_2) = (1,03.10^{-29})N_a - (5,15.10^{-27})N_e \qquad (2.51)$$

The electron density N_e follows from:

$$N_e = (2,01.10^{26}).[(n-1)(\lambda_2) - (n-1)(\lambda_1)] \qquad (2.52)$$

So far, static polarizabilities were used in this discussion. For relatively small wavelengths however, especially in the optical range, the dispersive correction factor should be taken into account (in the above example, Rosado used a factor $\alpha_a(\lambda_2)/\alpha_a(\lambda_1)$=1,01, which makes no significant difference).

2.3.4 Reflectometry

An alternative technique to measure the electron density is reflectometry (*hugenholtz90, hutchinson87*).
Although it is generally less accurate, reflectometry is especially suited to thermonuclear plasmas with extremely large electron densities. Another advantage of reflectometry is that it offers a direct measurement of the radial density profile, without Abel inversion.

The basic principle of reflectometry comes from the reflection of waves with a frequency lower than the plasma frequency.
The electron density increases towards the centre of the plasma and the plasma frequency increases along with it. A probe beam, directed at the heart of the plasma, will penetrate into the plasma until it reaches the point where the electon density is critical for that frequency. The beam will then be reflected back onto a detector and the signal is compared to a reference signal. From the phase shift, the place at which the reflection occurred can be deduced.
A major problem in accurately determining the point of reflection is the effect of the refractive index of the plasma in front of the reflecting layer. For a normal density profile it can be approximated by an average density $<n>\approx 0,6$ (*hugenholtz90*), but for a more accurate treatment the Wentzel-Kramers-Brillouin approximation method should be used (*gasiorowitz74*).
By sweeping the probe frequency, the radial electron density profile of a steady plasma can be established. If the plasma is not stationary, the changes in radial position of a several density layers can be monitored by applying several fixed frequencies simultaneously in a multi-channel set-up.

Reflectometry is also used as a diagnostic for the earth's ionosphere, where a pulsed probe is used, and the time interval between emission and detection is measured (*sturrock94,jackson75*).

3 Interference and interferometry

Interference is the physical phenomenon which occurs when two wave trains of (nearly) equal frequency cross. Their separate effects will then combine to form a new wave pattern, with a resulting complex amplitude that is the sum of the complex amplitudes of the contributant waves. Generally, the waves will reinforce each other in some regions while cancelling out in others. This is best observable when the original waves have comparable amplitudes.
Contrary to what the term interference implies however, the waves do not actually interfere with one another. After they have crossed each wave continues on undisturbed by the encounter.

An everyday example of interference can be seen when a ship passing through a canal makes waves which subsequently reflect off a steep shore, creating a much more pronounced disturbance in which the regions of maximum and minimum follow lines that remain fixed. Light also commonly displays interference effects, as the beautiful colour patterns of oil slicks spilled on tarmac roads demonstrate all too often.

Because light is an extremely rapid undulation, all interference effects are averaged out and only the resulting intensity distribution will be observed. This averaging process imposes strict conditions on the light waves for observable interference to occur: the waves have to be monochromatic and coherent. Another condition for optical interference arises from the transversal wave nature of light, which gives rise to polarization. Only parallel polarization states can create an interference pattern. These conditions are discussed in section 3.2. First, in section 3.1, the basic equations for interference are outlined. In section 3.4 the principles of optical interference will be applied to interferometry.

3.1 Optical interference: basic equations

In this section the basic equations of optical interference will be derived assuming an ideal source of coherent, monochromatic light. The conditions for interference will be treated in the next section.

As stated previously light can be thought of as an electro-magnetic wave. Starting from Maxwell's equations we get the following wave equation for the electric field:

$$\nabla^2\overline{E} = \epsilon\mu \frac{\partial^2\overline{E}}{\partial t^2} \quad , \qquad (3.1)$$

A similar equation can be written for the magnetic field. This would however not contain any additional information, as, far from the source, the magnetic field is completely determined by the electric component.

In the optical range, measurement of the fields themselves is virtually impossible because of the extremely high frequencies (10^{14}-10^{15} Hz). Light is experienced as a flux of radiative energy, with an intensity defined by:

$$I = \varepsilon v < |\bar{E}|^2 > \tag{3.2}$$

As the fields are solutions to a second degree linear differential equation, the superposition principle applies. The total field in a given point is thus the vectorial sum of all the fields in that point.
We speak of optical interference when this vector summation gives rise to a redistribution of intensity over space.

Limiting ourselves to the interference of just two waves, we find:

$$\bar{E} = \bar{E}_1 + \bar{E}_2 \tag{3.3}$$

and for the intensity:

$$I = \varepsilon v < |\bar{E}|^2 > = \varepsilon v \left(< |\bar{E}_1|^2 > + < |\bar{E}_2|^2 > + 2 < \bar{E}_1 . \bar{E}_2 > \right) \tag{3.4}$$

The last term in this equation contains the interference information, and is called the interference term.

If the vectors E_1 and E_2 are perpendicular, the waves are orthogonally polarized, their cross product is always zero and thus no interference occurs: this is the mathematical basis of the polarization condition.
If the vectors are parallel however, the vector summation simplifies to a scalar summation.

As we are only interested in the intensity the precise shape of the wavefront does not really matter. The conclusions drawn from a particular wave form will apply generally. We will look in more detail at the interference pattern of two monochromatic point sources, with parallel polarization. In a point far from the sources the wavefronts can be approximated by plane waves and the fields take the form:

$$\bar{E}_i(\bar{r}_i,t) = \bar{E}_{0i} . \exp[i(\bar{k}_i . \bar{r}_i - \omega t + \varphi_i)] \tag{3.5}$$

And:

$$< |\bar{E}_i|^2 > = \frac{1}{2} |\bar{E}_i|^2 = \frac{1}{2} E_{0i}^{\,2} \tag{3.6}$$

Because of the parallel polarizations the vector nature of the field is no longer relevant and the interference can be described by a scalar wave theory in terms of complex amplitudes. The amplitude of the resultant field becomes:

$$|\bar{E}|^2 = E.E^* = E_{01}^{\,2} + E_{02}^{\,2} + 2E_{01}E_{02}\cos\delta \tag{3.7}$$

And its time-averaged value:
Where for monochromatic light the total phase difference δ is a combination of the difference in optical path length and the difference in epoch angle:

$$<|\bar{E}|^2> = E_{01}^2 + E_{02}^2 + 2.E_{01}.E_{02}<\cos\delta> \tag{3.8}$$

$$\delta = \bar{k}_1.\bar{r}_1 - \bar{k}_2.\bar{r}_2 + (\varphi_1 - \varphi_2) \tag{3.9}$$

Coherence implies that δ is a constant, and the time-averaging of the cosine term then has no effect:

$$<\cos\delta> = \cos\delta \tag{3.10}$$

However, if the waves are not fully coherent the phase difference will not be constant, and the averaging of cos Δ will result in a blurring of the interference pattern. In the case of completely incoherent waves $<\cos\delta>=0$, the interference term will vanish altogether, and no interference will occur.

So far we have limited our discussion to ideal interference. The non-idealities that will be discussed in the next section merely come down to corrections in equation 3.10.

For coherent light with parallel polarization the resulting intensity thus becomes:

$$I = \frac{\varepsilon v}{2}\left(E_{01}^2 + E_{02}^2 + 2E_{01}E_{02}\cos\delta\right) \tag{3.11}$$

Or:

$$I = I_1 + I_2 + 2\sqrt{I_1 I_2}\cos\delta \tag{3.12}$$

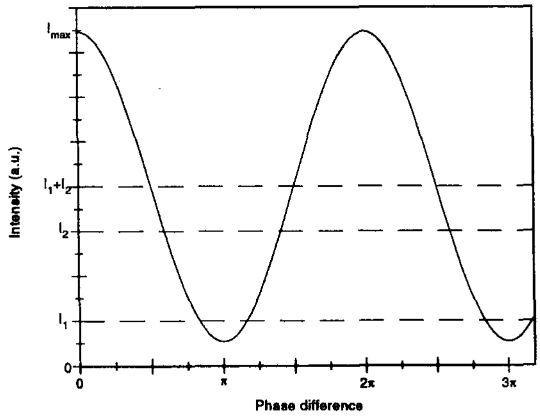

Figure 3.1: intensity as a function of phase difference

The interference does not change the total intensity integrated over all space, it merely redistributes the intensity, creating brighter and darker spots. These represent regions of constructive ($I>I_1+I_2$) and destructive ($I<I_1+I_2$) interference.

Maximum contrast is obtained for $I_1=I_2=I_0$, in which case the intensity is doubled at the peaks and becomes zero in the troughs (total destructive interference):

$$I = 4I_0\cos^2\left(\frac{\delta}{2}\right) \tag{3.13}$$

3.2 Conditions for optical interference

As has already been mentioned in the previous sections, interference between light waves can only be observed or measured if several conditions are met. In this section the concepts of coherence, monochromaticity and polarization states shall be discussed.

3.2.1 Emission and coherence

Light emission occurs when an excited atom returns spontaneously to a lower-lying state (usually the ground state) under radiation of a photon, which can be thought of as a finite wave train of about 10^{-8} s. The epoch angle difference between two emitters has to be constant for a steady interference pattern to be observable. If the relative epoch angle remains constant we speak of coherent waves.

Because atomic transitions are purely stochastic events, two distinct emitters will not maintain a constant epoch angle difference for longer than 10^{-8} s, after which their interference pattern will shift in a random way. Therefore, two distinct emitters will not display observable interference effects, and in practical interferometry one single primary source is used to create two coherent secondary sources.

However, a macroscopic thermal light source is a collection of individual atoms, which act as point sources, all radiating incoherently. The coherence of even a single light source is thus limited, and the coherence length is determined by the frequency spread of the source, as will be shown below.

A laser is fundamentally different from a thermal light source as it emits light by stimulated emission instead of spontaneous emission. This means the emission process is no longer stochastic, and the atoms in a laser will radiate coherently. Lasers therefore have much longer coherence lengths than other sources, making them especially suitable for interference applications.

3.2.2 Monochromaticity and degree of coherence

Monochromatic light is defined as light of one single, constant frequency. A monochromatic beam would thus contain only photons of exactly the same energy.

However, in a thermal source, photons are created by transitions between atomic states, and this process introduces a frequency spread because of the Heisenberg uncertainty principle. This states that the finite lifetime of an excited atomic state gives rise to a finite spread in its energy, inversely proportional with the lifetime.

This fundamental frequency spread may further be broadened by collisions and other interatomic interactions. Moreover, since the atoms are in random thermal motion the frequency distribution of the source will be broadened by the Doppler effect. At room temperature Doppler broadening is normally the dominating process.

The spectrum of a realistic monochromatic source will thus show a very narrow frequency range, containing most of the energy. The full width at half maximum of the line profile is called the bandwidth.

As truly monochromatic light is physically unattainable, monochromatic light is often defined more loosely as light having a small bandwidth relative to its mean frequency.

An individual wave train emitted by a (quasi-)monochromatic source is a coherent superposition of wavelets of all the frequencies within the spectral line. Because of dispersion, the phase velocity is different for each frequency or wavelength, and such a composite wave will lose its ideal sinusoidal shape gradually. The separation between the individual wave crests will grow larger with time, and the wave train will expand.
Initially, each wave train has a spread in time of $\Delta t=1/\Delta\nu$; Δt is called the coherence time. This leads to the concept of coherence length, which is the distance light travels in the coherence time interval:

$$\Delta x = \frac{c}{\Delta\nu} \tag{3.14}$$

In terms of the mean wavelength and the wavelength spread, the coherence length becomes:

$$\Delta x = \frac{\lambda_0^2}{\Delta\lambda} \tag{3.15}$$

If, in an interference experiment, wave trains from a single source are made to follow different paths and then recombined, they will only be coherent if the relative optical delay $\tau=(OPL_1-OPL_2)/c$ is smaller than Δt.
In other words, there will be no interference pattern if the optical path length difference between the two paths exceeds the coherence length.

For a light bulb, emitting white light, the bandwidth is of the same order as the principal frequency, and the coherence length will be typically below 1 μm. With special provisions to keep the bandwidth small, for a Hg discharge lamp a coherence length of a few cm can be attained, which is as high as thermal sources go.

To reach even higher coherence lengths (which are required for instance in Fabry-Perot interferometry, see chapter 4) laser sources must be used. Employing sophisticated stabilization techniques, coherence lengths of many km have been achieved.

3.2.3 Polarization

Another interference condition comes from the transversal nature of the electro-magnetic waves. In the previous section we derived the basic interference equations assuming field vectors, which were linearly polarized and parallel. Nonetheless, the results apply regardless of the polarization state of the waves, whether linear, circular, elliptical or unpolarized. This follows from the fact that any polarization state can be synthesized out of two orthogonal linear polarization states, which may be either mutually coherent or not (as in the case of unpolarized light). Thus every plane wave, polarized or not, can be written as $\bar{E}=\bar{E}_\perp+\bar{E}_\parallel$.
The superposition of two such waves, would result in a intensity distribution consisting of two overlapping, independent interference patterns $<(\bar{E}_{\parallel 1}+\bar{E}_{\parallel 2})^2>$ and $<(\bar{E}_{\perp 1}+\bar{E}_{\perp 2})^2>$.
$\bar{E}_\perp$ and $\bar{E}_\parallel$ are defined relative to the common reference plane spanned by their respective propagation vectors. It is obvious that $\bar{E}_{\perp 1}$ and $\bar{E}_{\perp 2}$ are always parallel, and a scalar theory will suffice for the interference of the perpendicular components. The components parallel to the reference plane, however, can make the same angle as the propagation vectors, so we have to take into account the vector nature of the fields. Still, in many cases the propagation vectors may be taken to be parallel and the scalar theory of the previous section will apply.

3.3 Interferometry

In its broadest sense, an interferometer is defined as a device that uses optical interference as a basis for measurements. Interferometers are divided roughly into two classes by the number of interfering beams: two beam and multiple beam interferometers. Multiple beam interferometry will be treated in chapter 4, while this section deals with two beam interferometers.

An interferometer can basically be operated in two ways. Traditionally, the actual fringe pattern was photographed and analyzed. Nowadays however, photoelectric detectors have for the most part taken the place of photographic plates and the intensity of the central spot of the fringe pattern is monitored. As the phase difference between the interfering beams is increased, new fringes appear at the central spot; if the phase difference decreases fringes disappear there.
The techniques discussed in this thesis all employ central-spot scanning, so the details of the fringe pattern shall not be discussed here.

3.3.1 Michelson and Mach-Zehnder interferometers

The most widely used designs for two beam interferometry are the Michelson and the Mach-Zehnder interferometers.

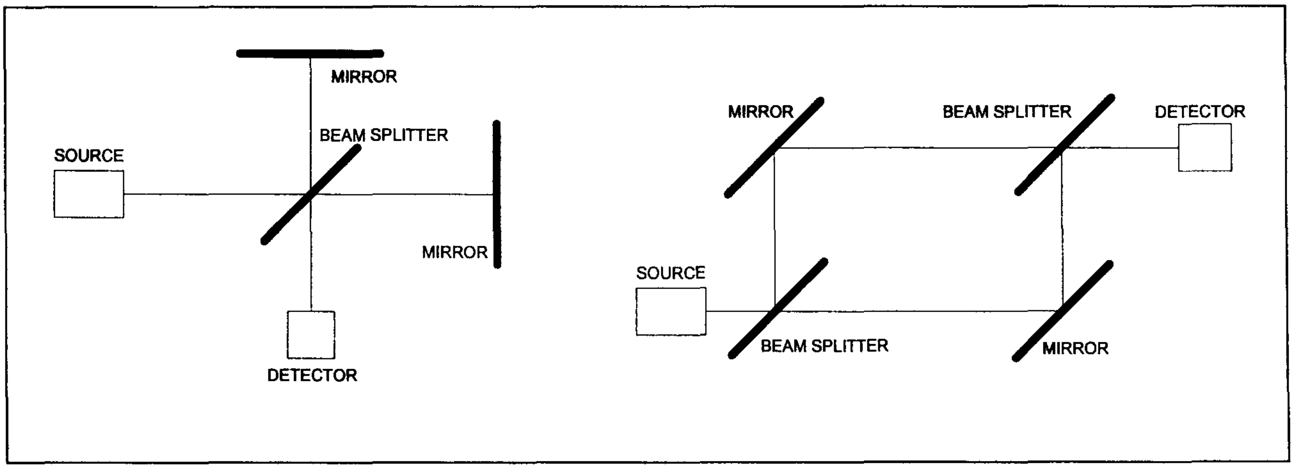

Figure 3.2: Michelson and Mach-Zehnder interferometers

The Michelson interferometer uses just one beamsplitter, both for separating and recombining the beams, and two mirrors for reflection. If necessary, dispersion and other parasitic effects can be countered by a more sophysticated design for the mirrors, focusing lenses and compensator plates.

Michelson interferometers are well suited for accurate absolute wavelength measurements. Typically, in such an experiment one of the mirrors is moved over a distance d, and the number of fringes created or annihilated (m_f) is counted. From this we find the wavelength by:

$$\lambda = \frac{2d}{m_f} \tag{3.16}$$

If the wavelength is known, as in the case of a HeNe laser, a similar procedure can be used for displacement measurements.

The Mach-Zehnder interferometer differs from the Michelson in this respect that the beam is split at one beamsplitter and recombined at another identical beamsplitter. The two paths are optically symmetric and no compensator plates are required. The optical replacement scheme of the Mach-Zehnder is basically the same as that of the Michelson, and so the interference patterns are similar.

Generally, the Mach-Zehnder has more degrees of freedom, and is therefore more flexible than the Michelson. A disadvantage of the Mach-Zehnder is that one can not vary the path length difference between the two beams, inhibiting simple wavelength measurements. Replacing the mirrors by mirror pairs removes this drawback.

3.3.2 Two-beam interferometry as a plasma diagnostic

When using a two beam interferometer as a plasma diagnostic the plasma is introduced in one arm, while the other arm serves as a reference. A variation of the refractive index of the plasma changes the optical path length along the plasma arm. This results in a phase shift between the plasma arm and the reference arm of

$$\Delta\Phi = \frac{2\pi}{\lambda}\int_{L_p} \Delta n(x)\mathrm{d}x \qquad (3.17)$$

with L_p the length of the plasma and $\Delta n(\mathrm{x})$ the local change in n.

If we are to see fringes with high visibility the optical delay $\tau=\Delta\Phi/c$ between the two arms of the interferometer should be small compared to the bandwidth of the source: $\tau.\delta\nu<1$. Thus the source bandwidth sets an upper limit on the relative path length difference between the two arms. Maximum contrast is obtained if the two arms of the interferometer transmit equal intensities and if the two beams do not undergo any relative polarization state changes. These conditions suggest the use of a compensating device in the reference arm.

In a simple interferometer, a beam of monochromatic light is split; one part is sent through a plasma and the other part forms a reference beam. Both beams are subsequently recombined to create an interference pattern. The electric fields associated with these two beams are E_p and E_r respectively:

$$E_p(t) = E_1\exp(i\omega t+i\Phi) \qquad (3.18)$$

$$E_r(t) = E_2\exp(i\omega t) \qquad (3.19)$$

and the total field is given by:

$$E_T(t) = [E_1+E_2\exp(i\Phi)]\exp(i\omega t) \qquad (3.20)$$

The output intensity consists of a constant component plus an interference term, depending on the cosine of the phase difference:

$$I = \varepsilon v < |E_T|^2 > = \varepsilon v \left[E_1^2 + E_2^2 + 2 E_1 E_2 \cos \Phi \right] \tag{3.21}$$

In determining the change in plasma parameters from the measured change in intensity, the above equation gives rise to some ambiguity and inaccuracies.

These inaccuracies are due to the occurrence of the amplitudes in the interference term and the cos(Φ) dependence on the phase shift.
Variations in amplitude of one of the beams are interpreted as phase shifts. This effect can be corrected for, though with some difficulty, by monitoring the separate intensities of both beams. The cos(Φ) term results in a non-linear relation between the phase shift and the resulting output intensity, which can be a problem, especially at the extrema, where $dI/d\Phi$ is zero. This problem can be solved by employing a feedback loop to keep the output signal constant (*kroesen90*). Another problem is that the cos(Φ) term introduces ambiguities in the sign of the phase change. This can be solved by using a polar interferometer, in which a second reference beam, with π/2 phase difference, is employed in order to yield a cos(Φ) and a sin(Φ) signal simultaneously. This method however, is hard to implement in practice (*hugenholtz90*).

3.3.3 Phase modulation

Both these problems can be simultaneously resolved by phase modulation. As the frequency of a wave is simply the rate of its phase change, phase modulation is equivalent to frequency modulation. We can thus turn to heterodyne detection techniques, and we speak of a heterodyne interferometer.

The expressions for E_p and E_r now become:

$$E_p(t) = E_1 \exp(i\omega_1 t + i\Phi) \tag{3.22}$$

$$E_r(t) = E_2 \exp(i\omega_2 t) \tag{3.23}$$

and the output intensity becomes:

$$I(t) = \varepsilon v \left[E_1^2 + E_2^2 + 2 E_1 E_2 \cos((\omega_1 - \omega_2)t + \Phi) \right] \tag{3.24}$$

Without modulation, if the rate of change of phase difference $d\Phi/dt$ is zero, the output intensity is constant. When a phase change occurs, the intensity is modulated with a frequency $\omega_m = |d\Phi/dt|$, and the sign of the phase change remains unresolved.
In a heterodyne interferometer, the output intensity is modulated with a frequency $\omega_m = \omega_1 - \omega_2$. A change in phase difference increases or decreases the modulation frequency, depending on its sign: $\omega_m = \omega_1 - \omega_2 + d\Phi/dt$.

A second advantage of the heterodyne interferometer is that the phase shift is not determined from absolute output intensities. Because only the frequency shift is measured, the changes in amplitude in either the plasma or the reference beam have no effect on the phase shift.
In practice, phase modulation has been realized by a moving mirror, a rotating grating or by using two separate lasers, with slightly different frequencies (*veron79,hugenholtz90*).

3.3.4 Feedback control

Another way to improve the interferometer, is to introduce a feedback loop to keep the output intensity signal constant. Any phase change in the plasma beam will then be compensated by a corresponding change in the reference path length.
In the case of a Michelson interferometer, this can be done by mounting the reference mirror on a piezo-element driven by an electronic control circuit. Since the voltage-displacement characteristic of the piezo-element is linear, measurement of the driving voltage yields a signal that is proportional to the phase shift in the plasma (*sanders85*).
In this set-up the sign of the phase shift remains ambiguous. It can however be resolved by introducing a deliberate change in some parameter, the effect of which is known.
Feedback control cannot be applied in a Mach-Zehnder configuration, as the path length difference of the interferometer arms cannot be easily varied.

Is dit niet mogelijk door een brekingsindex van
kristal te laten moduleren met drukvariaties.

4 Fabry-Perot interferometers

The Fabry-Perot interferometer is based upon the interference of multiply reflected waves. Originally, Charles Fabry and Alfred Perot employed a set of two plane parallel reflecting surfaces, but other geometries can be used as well. A Fabry-Perot is in effect simply a resonant optical cavity, and as such it forms the basis of all modern laser cavities.

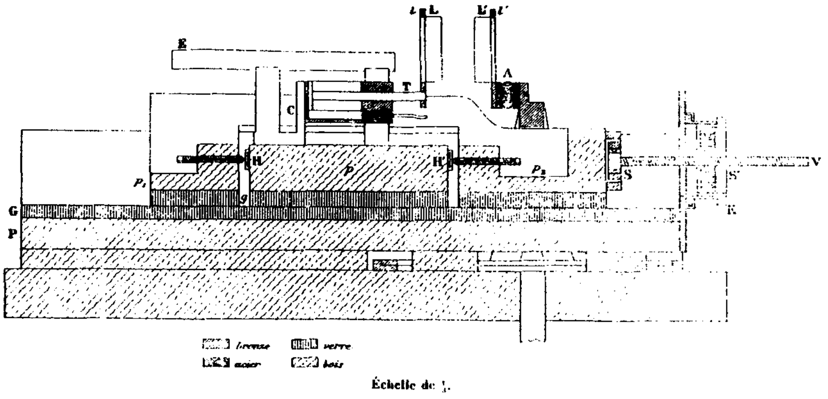

Figure 4.1: the original interferometer as designed by Fabry and Perot

Essential to the Fabry-Perot is that the reflecting surfaces should have a high reflectance and at the same time a finite transmittance. Such surfaces can be produced by applying a thin metal film or a dielectric coating. In section 4.1 their respective advantages and disadvantages are elucidated.

The characteristics of an ideal Fabry-Perot are a function only of the optical parameters of the mirrors, and their separation. This is discusses in section 4.2 for plane mirrors, and in 4.4 for spherical mirrors.
Imperfections and misalignment will broaden the instrumental profile, and set an upper limit on the resolving power of the instrument. In section 4.3 a general broadening theory is given.

4.1 Reflecting films

The reflecting surfaces are the heart of the Fabry-Perot instrument. The interferometer performance is largely defined by its finesse, and its transmittance (see also sections 4.2 and 4.4). Both quantities should be made as high as possible. However, increasing the finesse means an increase in the reflectance of the mirrors, which usually leads to reduction in transmittance. Suitable reflecting surfaces can be metal coatings, or (multilayer) dielectric coatings.

Dielectric mirrors are produced by evaporating a layer of dielectric material onto a substrate. Dielectric coatings can be produced with reflectances close to unity, while keeping absorption losses low. Dielectrics are the most efficient mirrors for visible and near-infrared radiation, but they are specific to a small range of wavelength.
By employing multiple layers of appropriate refractive indices, a high reflectance can be attained

over a greater range of wavelengths.

For broadband measurements metal-coated surfaces are most suitable. The reflectance of these mirrors will increase with increasing thickness of the metal layer. However, so will the absorption, and the transmittance will drop with increasing finesse.
The reflectance and the peak transmission can be calculated as a function of wavelength and layer thickness from values of the refractive index and absorption coefficient of the coating metal. Remarkably, for a given reflectance, a higher absorption coefficient gives a higher transmittance.
For very thin films (≥50 nm) care should be taken, as the optical constants may differ from the bulk values. The film structure will be more or less spongy, and isolated aggregates of metal are observed for extremely thin layers (≥10 nm). This leads to a decrease in the effective conductivity of the metal layer, and the reflectance will drop sharply.

Metal films have the advantage that they are typically much thinner than dielectric coatings, which makes it easier to maintain the original mirror shape. Furthermore, a metal film can be easily removed and replaced by another coating if the Fabry-Perot is used in another set-up.

4.2 Plane Fabry-Perot

Typically, multiple beam interference occurs when light is reflected many times between two surfaces of high reflectivity. The effect was first described by George Airy in 1831 for light transmitted through a system of glass slides separated by a very small interval of air. He calculated the phase retardation between successive orders of reflections and he also derived formulas for the brightness of the transmitted and the reflected light which he noted to be complementary in the absence of absorption.
It took many years for optical technology to advance to a level where the Airy formulas could be used to describe actual fringe systems, as was first done in 1893 by Boulouch. From 1897 on Fabry and Perot performed a number of brilliant experiments with their particular design of multiple beam interferometer, which firmly established their instrument as the most accurate spectral filter available. Nowadays for instance, a Fabry-Perot interferometer is used to measure and define the unit of length, the meter.

4.2.1 Transmission fringe profile

The accurate experiments of Fabry and Perot, using highly reflective silvered glass plates, allowed them to rederive Airy's expression for the transmitted intensity in a form containing the reflectivity of the surfaces (*vaughan89*):

$$I_t/I_i = \left(\frac{T}{1-R}\right)^2 \cdot \frac{1}{1+[4R/(1-R)^2]\sin^2(\delta/2)} \tag{4.1}$$

In which δ is the phase shift between successive orders of reflection, which for plane surfaces is given by:

$$\delta = \frac{2\pi}{\lambda}(2nd\cos\theta) \tag{4.2}$$

Here d is the separation between the mirrors and θ is the angle of incidence. Assuming no absorption, R+T=1 and the equation simplifies to:

$$I_t/I_i = \frac{1}{1+F\sin^2(\delta/2)} \equiv A(\delta) \tag{4.3}$$

Where we have introduced the coefficient of finesse

$$F = \frac{4R}{(1-R)^2} \tag{4.4}$$

and the Airy shape function

$$A(\delta) = [1+F\sin^2(\delta/2)]^{-1} \tag{4.5}$$

The Airy function is the basic relationship describing the instrumental function of an ideal multiple beam interferometer with reflectivity R. In practice the Airy profile will be modified by mirror imperfections and other broadening mechanisms.

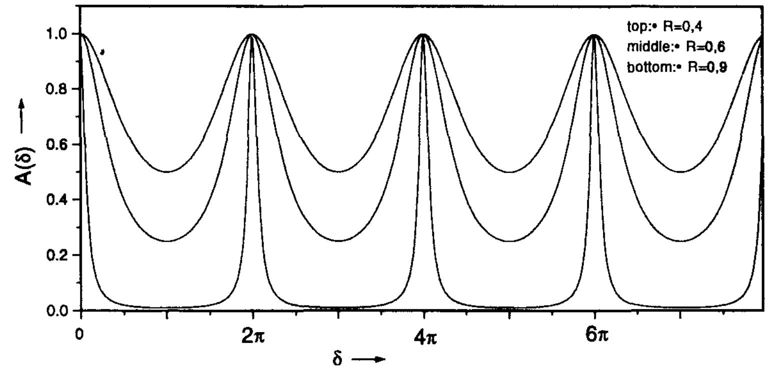

Figure 4.2: Airy profiles for different values of R

For small values of R, we get essentially the situation of only two interfering beams. The fringes will be broad and the minima will not approach zero. With increasing R however, the coefficient of finesse F will rise rapidly, and the Airy function will become ever more sharply peaked. The fringes will then also become sharper and the background intensity between the peaks will be nearly zero. The transmitted fringe system will thus consist of a series of sharp bright fringes against a dark background.

The reflected intensity also forms a system of fringes, which are complementary to the transmitted fringes. Without absorption, conservation of energy requires $I_r+I_t=I_i$ and so:

$$I_r/I_i = 1-A(\delta) \tag{4.6}$$

Even for low R the minima of intensity will be zero in the reflected system, and for larger R the reflected fringes will be visible as narrow dark rings on a bright background.

4.2.2 Optical losses

So far, we have neglected optical losses at the reflecting surfaces. There will however always be some losses, due to scattering and absorption. The energy conservation relation should then be extended to include A, the fraction of light absorbed or scattered:

$$R + T = 1 - A \tag{4.7}$$

The transmitted intensity now becomes:

$$I_t/I_i = [1 - A/(1 - R)]^2 \, A(\delta) \tag{4.8}$$

The principal effect of absorption or scatter on the transmitted fringe system is thus to reduce the fringe intensity by a factor $[1\text{-}A/(1\text{-}R)]^2$.

The peak fringe intensity in the transmitted system is given by:

$$I_{\max} = I_i[1 - A/(A+T)]^2 = I_i T^2/(1 - R)^2 \tag{4.9}$$

And the minimum intensity, halfway between the peaks:

$$I_{\min} = I_i[1 - A/(A+T)]^2/(1+F) = I_i T^2/(1+R)^2 \tag{4.10}$$

The ratio of peak to background is called the extinction or contrast ratio *C*. Remarkably, this measure of sensitivity is only dependent on R and is not affected by optical losses:

$$C = \frac{(1+R)^2}{(1-R)^2} \tag{4.11}$$

4.2.3 Finesse

As a measure of the sharpness of the peaks we take the half-width at half maximum $\delta_{1/2}$, given by:

$$F \sin^2(\delta_{1/2}/2) = 1 \tag{4.12}$$

or:

$$\delta_{1/2} = 2 \arcsin(1/\sqrt{F}) \tag{4.13}$$

For F large, the sine may be approximated by the angle.

$$\delta_{1/2} \approx 2/\sqrt{F} = (1-R)/\sqrt{R} \tag{4.14}$$

Clearly, the Airy profile is a periodic function, with a spacing between successive maxima of 2π. The ratio of peak separation to the full width at half maximum of the fringes is called the finesse F_0.

$$F_0 = \frac{2\pi}{2\delta_{1/2}} = \pi \frac{\sqrt{R}}{(1-R)} \tag{4.15}$$

More precisely, this is the reflectivity finesse, which would be found for an ideal Fabry-Perot with mirrors of reflectivity R. In practice, the finesse will be reduced because of mirror surface imperfections and other defects. This will be discussed in section 4.3.

The reduced finesse is an important quantity as it determines the spectral resolution of the interferometer, and thus is commonly used to define its performance. The reflectivity finesse can also be interpreted as the effective number of interfering beams.

4.2.4 Free spectral range

A monochromatic light beam generates a well-defined fringe pattern, which depends on the wavelength λ_0. If the source consists of two monochromatic components, two superimposed fringe systems would result. For light falling perpendicularly (θ=0) on parallel flat mirrors, the difference in phase delay for a wavelength λ_0 and another wavelength $\lambda_1=\lambda_0+\Delta\lambda$ amounts to:

$$|\Delta\delta| = 4\pi n d\frac{\Delta\lambda}{\lambda_0^2} \tag{4.16}$$

If the phase delay is equal to 2π the fringe systems overlap exactly, with the m_{th} order of interference of λ_0 matching the $(m-1)_{th}$ order of λ_1. The wavelength difference at which overlap occurs is called the free spectral range (FSR):

$$(\Delta\lambda)_{FSR} = \frac{\lambda_0^2}{2nd} \tag{4.17}$$

The free spectral range is often expressed in terms of wave numbers, leading to an expression containing only instrumental parameters:

$$(\Delta\sigma)_{FSR} = \frac{1}{2nd} \tag{4.18}$$

The above formulas describe the situation for light falling perpendicularly on parallel flat mirrors, where the optical path length is 2nd. The results however apply generally to all multiple-beam interferometers if the appropriate optical path length is substituted:

$$(\Delta\lambda)_{FSR} = \frac{\lambda_0^2}{\text{O.P.L.}} \qquad (\Delta\sigma)_{FSR} = \frac{1}{\text{O.P.L.}} \tag{4.19}$$

4.2.5 Resolving power

As the phase delay difference for two wavelengths becomes smaller, the peaks will start to overlap. We need a criterion to decide whether they remain individually discernible or not. This defines the chromatic resolving power of the interferometer.

Traditionally, the resolving power is derived from the Rayleigh criterion, which was originally conceived for diffraction patterns of gratings. The Rayleigh criterion allows direct comparison with other optical instruments such as prisms and gratings. The essential feature of the criterion is that two fringes of equal intensity are said to be just resolvable when the total intensity at the central saddle point of the combined peak is $8/\pi^2$ of the maximum intensity.

In the case of a multiple-beam interferometer the resolving power can be defined in a much simpler form: two fringes are just resolved when they meet at their half-intensity points: the separation between the maxima is then equal to the full width at half maximum of the fringes.

$$(\delta\lambda)_{\min} = 2\delta\lambda_{1/2} = \frac{\Delta\lambda_{FSR}}{F_0} = \frac{\lambda_0^2}{\text{O.P.L.}}\cdot\frac{1}{F_0} \tag{4.20}$$

And the resolving power is given by:

$$R_0 = \left|\frac{\lambda_0}{(\delta\lambda)_{\min}}\right| = \frac{\text{O.P.L.}}{\lambda_0}.F_0 \tag{4.21}$$

(Note: the exact Rayleigh criterion would give a 3% lower resolving power.)
Interpreting the finesse as the effective number of interfering beams, this result has universal validity in its statement that the resolving power of an optical instrument is given by the number of wavelengths within the optical path difference of the extreme rays.

Nowadays, the Rayleigh criterion has little meaning as a detection limit, as more advanced detectors and measurement techniques have made it possible to measure much smaller intensity differences. However, the resolving power remains useful for comparing different instruments (even of widely varying optical principle) and serves well as a first order estimate of spectroscopic performance.

4.3 Fringe profile, defect broadening and reduced finesse

The spectral resolution of an ideal Fabry-Perot is determined by its finesse, which is a function of the reflectivity of the mirrors. However, every practical Fabry-Perot set-up has imperfections or defects, such as surface roughness, shape errors, misalignment and mechanical vibrations. These impose a fundamental lower limit on the fringe width regardless of the reflectance of the interferometer mirrors. The reduced finesse of the interferometer is determined by a convolution of its theoretical Airy profile with the defect profiles.

Most theories of fringe broadening assume that the defect broadening can be treated as a relatively small perturbation. This is the case for low reflectances, giving broad natural fringes, and small defects. However, both reflectivity finesse and defects can be large. High reflectivity finesse is not always a blessing: the sensitivity to alignment errors is increased, and transmission drops due to cumulative scattering.

As a general rule of thumb, both finesse and signal level are optimized when the reflectance finesse is matched to the defect finesse. This means perturbation treatments are no longer valid and a more rigorous mathematical approach must be taken, in which the convolution of the main defect profiles with the unbroadened fringe is computed. This was first done by Sloggett (*sloggett84*). Assuming the defects are statistically uncorrelated this procedure is accurate for every defect form and magnitude.

4.3.1 Airy profile

The transmitted intensity profile of an ideal Fabry-Perot with plane mirrors of reflectance R is given by the Airy function:

$$A(\delta) = \frac{(1-R)^2}{1+R^2-2R\cos\delta} \tag{4.22}$$

The Airy function has maxima at multiples of 2π, which is the free spectral range in phase space. The half-width at half maximum $\delta_{1/2}$ of the fringe peaks is given by:

$$\delta_{1/2} = 2\sin^{-1}\left(\frac{1-R}{2\sqrt{R}}\right) \tag{4.23}$$

and the reflectivity finesse is:

$$F_0 = \frac{2\pi}{\delta_{1/2}} \tag{4.24}$$

As the Airy function is periodic, it can be represented by a function of the form:

$$A(\delta) = \sum_{n=-\infty}^{\infty} g(\delta - 2\pi) \tag{4.25}$$

where g(Ψ) is the profile of a single fringe.

Instead of calculating g(Ψ) by truncating A(Ψ) midway between the peaks, at ±π, we may approximate the fringe profile near its maximum by a Lorentzian function (*steel67*):

$$g(\delta) = I_{max}\frac{\ln^2(R)}{\delta^2+\ln^2(R)} \tag{4.26}$$

with peak intensity:

$$I_{max} = \frac{2(1-R)}{(1+R)(-\ln(R))} \tag{4.27}$$

and half-width at half maximum:

$$\delta_{1/2} = -\ln(R) \tag{4.28}$$

In the Lorentzian approximation the values for both the peak intensity and the half-width are slightly too low, but the errors are less than 1% for R>0,7 and decrease rapidly with increasing reflectance. For large R the Lorentzian function is an excellent approximation to the Airy fringe profile near a peak. For many mathematical operations, such as convolutions, the Lorentzian approximation is more convenient than the Airy function.

4.3.2 Defect broadening

The profile of a broadened fringe is determined by two functions: g(δ) representing the ideal reflectance fringe profile and h(ϕ) characterizing the distribution of defects. Here δ is the phase advance corresponding to a double passage of light within the interferometer, and ϕ is a perturbation in δ. h(ϕ) has the properties of a probability density function with a standard deviation σ defined by:

$$\sigma^2 = \int_{-\infty}^{\infty} \varphi^2 h(\varphi)\, d\varphi \tag{4.29}$$

The contribution of light passing the interferometer with phase shift ϕ is g(δ+ϕ)h(ϕ)*d*ϕ, and the total transmitted intensity is given by the convolution of g and h:

$$f(\delta) = \int_{-\infty}^{\infty} g(\delta+\varphi)\, d(\varphi)\, d\varphi \tag{4.30}$$

As convolutions are infinite integrals, generally there will not be any analytical solution. We are however not interested in the precise shape of the profile, but only in the reduced finesse, which follows directly from the width of the convolvent profile.

If both g(δ) and h(ϕ) are taken to be symmetric about 0 (even functions), f(δ) will also be symmetric about 0. Its maximum value will be given by f(0):

$$f(0) = \int_{-\infty}^{\infty} g(\varphi)\, d(\varphi)\, d\varphi \tag{4.31}$$

and its half-width at half maximum W is defined by:

$$f(W_{1/2}) = \frac{f(0)}{2} \tag{4.32}$$

4.3.3 Reduced finesse

The reduced finesse is 2π divided by the full width at half maximum:

$$F_{red} = \frac{\pi}{W_{1/2}} \tag{4.33}$$

For two Gaussian functions G_1 and G_2, the convolution is again a Gaussian G_{conv} with half-width at half maximum $W^2 = W_1^2 + W_2^2$, and the reduced finesse becomes:

$$F_{res}^{-2} = F_1^{-2} + F_2^{-2} \tag{4.34}$$

Analogously, for two Lorentzian functions L_1 and L_2, the convolution is again a Lorentzian L_{conv}, however with half-width at half maximum $W = W_1 + W_2$. The reduced finesse is:

$$F_{res}^{-1} = F_1^{-1} + F_2^{-1} \tag{4.35}$$

The convolution of a Gaussian with a Lorentzian function is called a Voigt profile. This is a well-studied profile, as it also describes the profile of a Doppler-broadened natural emission line. The convolution of a Voigt profile with either a Gaussian or a Lorentzian, or another Voigt profile, will again yield a Voigt profile. Computation of its width is not straightforward, but it can be deduced from tables and graphs, which can be found in literature. The reduced finesse again follows from the resultant half-width at half maximum.

For a rough estimate of the reduced finesse, the component functions are often considered to be Gaussian in shape. This estimate will be somewhat higher than the exact reduced finesse, and for a more conservative estimate Lorentzian addition would be more appropriate.
If one of the finesses is very much smaller than the other finesses, that finesse can be taken as the effective reduced finesse. Therefore it is not meaningful to increase the reflectivity finesse, if the reduced finesse is already determined by some defect. Increasing the reflectance of the mirrors then merely serves to make the interferometer more sensitive to

4.3.4 Specific broadening mechanisms

With the improvement of mirror reflectivity came the recognition that the quality of the mirrors could provide a limit on the attainable resolution. Since then, developments in surface finishing have made it possible to reduce the surface roughness to better than 3 nm over large mirror diameters. Such a level of precision is however extremely costly and not attainable for all materials. In practice, most mirrors still have appreciable surface roughness, and in many instruments it remains the limiting factor. Besides by the surface roughness, the instrumental function is also broadened by other imperfections.

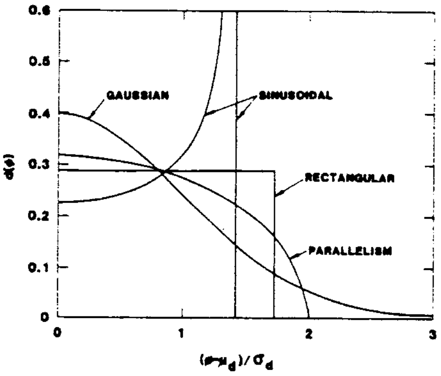

Figure 4.3: defect distributions (taken from sloggett84)

The most important broadening mechanisms are surface roughness, spherical shape defects, non-parallelism, and vibrations. The corresponding defect distributions are respectively Gaussian, rectangular, hemispherical and sinusoidal in shape. They will each be briefly discussed below.

Broadening due to surface roughness

Every surface has a finite roughness, however small. In a Fabry-Perot the surface roughness of the mirrors can be thought of as random variations in the mirror separation. The defect distribution of such a random phenomenon is a Gaussian distribution:

$$h(\varphi) = \frac{1}{\sqrt{2\pi}\,\sigma}\exp(-\varphi^2/2\sigma^2) \tag{4.36}$$

The standard deviation ς of the surface variations is usually expressed as a fraction of a wavelength λ/k; the higher k, the better the surface quality. The half-width of the phase distribution then becomes:

$$W = \frac{4\pi\sqrt{2\ln 2}}{q} \tag{4.37}$$

and the defect finesse follows from this:

$$F_D = \frac{q}{4{,}7} \tag{4.38}$$

This represents an upper limit on the attainable total finesse of the interferometer, regardless of the reflectance of the mirrors.
Convolution of the Gaussian defect distribution with the Lorentzian reflectivity profile gives a Voight profile. The width of the Voight profile can be determined from the graph in figure 4.4, given the widths of the unbroadened fringe and of the defect distribution.

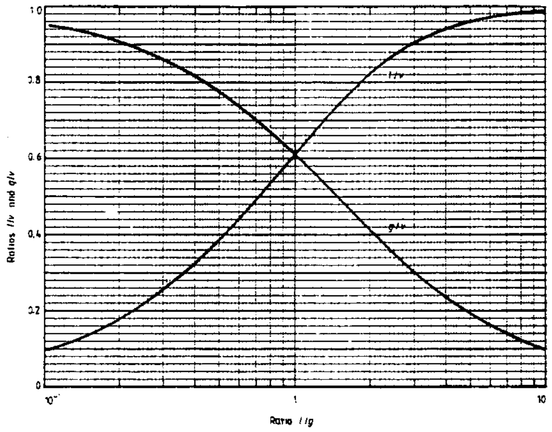

Voigt profile width as a function of the relative widths of its Gaussian and Lorentzian components

Broadening by a spherical shape error

Spherical shape errors give rise to an approximately rectangular phase distribution:

$$h(\varphi) = (2\varphi_{max})^{-1} \tag{4.39}$$

with ϕ_{max} half the width of the rectangular distribution. The corresponding standard deviation is:

$$\sigma = \varphi_{max}/\sqrt{3} \tag{4.40}$$

In the case of a rectangular distribution the convolution with the Lorentzian profile may be evaluated analytically:

$$f(\delta) = \frac{1}{2\varphi_{max}} \arctan\left(\frac{2\varphi_{max}/\delta_{1/2}}{1 + (\frac{2\delta}{\delta_{1/2}})^2 - (\frac{\varphi_{max}}{\delta_{1/2}})^2} \right) \tag{4.41}$$

The half-width at half maximum of the convolvent is given by:

$$W^2 = (\delta_{1/2})^2 + 4(\varphi_{max})^2 \tag{4.42}$$

and the reduced finesse becomes:

$$F_{red}^{-2} = F_0^{-2} + \left(\frac{\pi}{\varphi_{max}} \right)^{-2} \tag{4.43}$$

Spherical shape errors have become an important broadening mechanism since the improvements in surface microfinish. These imperfections are often caused by mechanical stress, induced by faulty mounting of the mirrors.

Broadening because of non-parallelism

Non-parallelism of the mirrors has two effects on the interferometer: the instrumental profile is broadened, but often more importantly it will result in loss of light intensity. The optical loss caused by the tilt of the mirror is a function of the reflectivity finesse, as this determines the effective number of interfering beams.

The defect distribution for non-parallelism is hemispherical in shape:

$$h(\varphi) = \frac{2}{\pi \varphi_{max}} \sqrt{1 - (\varphi/\varphi_{max})^2} \tag{4.44}$$

with a standard deviation:

$$\sigma_D = \varphi_{max}/2 \tag{4.45}$$

If the difference in plate separation from one side to the other is λ/k, the half-width at half maximum of the distribution is $W = k\sqrt{3}/8$.

Parallelism especially becomes a problem when the mirror separation is varied, by mechanical displacement of one of the mirrors. This degree of freedom introduces a kinematic instability, which must be minimized by careful design and construction of the interferometer.

Broadening by mechanical instabilities

Vibrations will appear as a variation in mirror separation in time instead of across the mirror surface. These temporal fluctuations will result in a broadening of the instrumental profile, which can be treated with the same mathematical tools as apatial defects.

A harmonic vibration is equivalent in phase distribution to a sinusoidal undulation in mirror separation, and its phase distribution is:

$$h(\varphi) = \frac{1}{\pi\sqrt{\varphi_{\max}^2 - \varphi^2}} \qquad (4.46)$$

with standard deviation:

$$\sigma = \varphi_{\max}/\sqrt{2} \qquad (4.47)$$

Vibrations are potentially rather dangerous for high finesse interferometers, as their particular phase distribution can give rise to subsidiary maxima in the intensity profile.

Approximation for small defects

For a spherical shape error with a rectangular defect distribution, the convolution integral was solved analytically to yield a profile with half-width:

$$W^2 = W_0^2 + 4\Phi_{\max}^2 \qquad (4.48)$$

Since for a rectangular distribution $\sigma = \phi_{\max}/\sqrt{3}$, we can also write:

$$W = W_0^2 + 12\sigma^2 \qquad (4.49)$$

And the reduced finesse may then be written as:

$$F_{res}^{-2} = F_0^{-2} + \frac{3}{\pi^2}\sigma^2 \qquad (4.50)$$

This equation is exact for the rectangular distribution but proves to be quite accurate for other distributions as well, provided their widths are not too large compared to the width of the Airy profile (*sloggett84*).

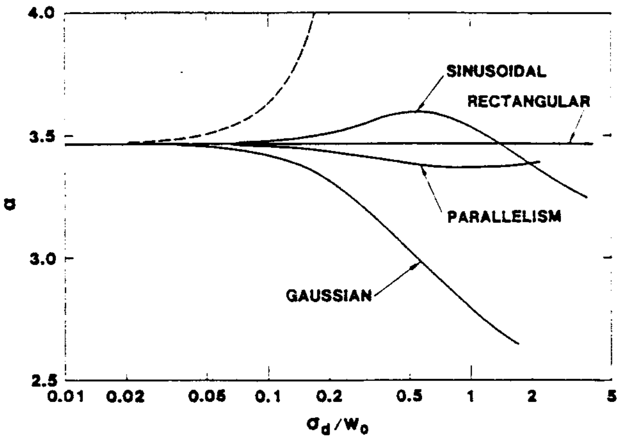

Figure 4.5: deviations from the approximation for several distributions (from sloggett84)

4.4 Confocal Fabry-Perot

The possibility of using spherical mirrors in a Fabry-Perot interferometer was first suggested by Connes in 1956. To avoid problems with mode-matching, the mirrors are placed at their confocal separation, which means that each mirror images the other mirror back upon itself. For identical spherical mirrors the confocal condition is fulfilled when the centre of the radius of curvature of each mirror is at the physical centre of the other.

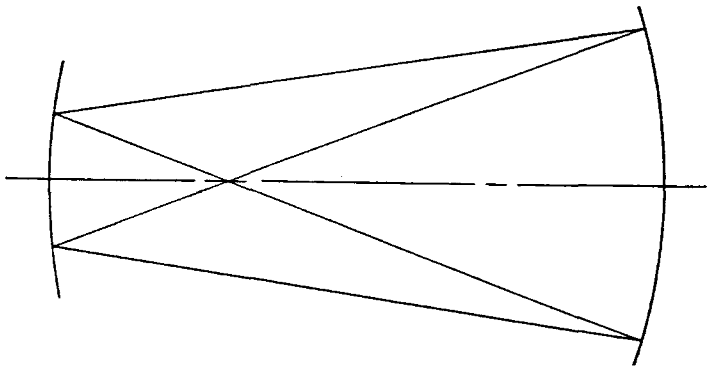

Figure 4.6: reentrant ray path in a confocal Fabry-Perot (from Herscher68)

Looking at the ray picture, we see that a paraxial ray is reentrant after traversing the interferometer four times, instead of after two transits as for the plane interferometer; the phase lag δ between beams of successive orders of interference is then approximately twice that of an otherwise identical plane interferometer.

The number of reflections between successive beams is also doubled, and R must be replaced by R^2 in the derivation of the transmission profile for plane mirrors. However, we see there is now a second set of transmitted rays, which have undergone two extra reflections, resulting in an extra factor R^2. The total transmitted intensity for spherical mirrors then becomes:

$$I_t/I_i = \left(\frac{T}{1-R^2}\right)^2 \cdot \frac{1+R^2}{1+[2R/(1-R^2)]^2 \sin^2(\delta/2)} \tag{4.51}$$

in which δ is the phase lag between successive orders of reflection.

To zeroeth-order approximation, the four-transit path is simply four times the mirror separation, and the phase lag becomes:

$$\delta = (2\pi/\lambda)4nd \tag{4.52}$$

Due to spherical aberration and small deviations from the exact confocal separation, the path length is changed for finite apertures. A ray from a small far-away source on the optical axis, entering a Fabry-Perot with mirrors exceeding the confocal separation by ε at a distance ρ from the optical axis, experiences a four-transit phase lag of (*herscher68*):

$$\delta = \frac{2\pi}{\lambda}\left[4(d+\varepsilon)-\left(\frac{\rho^4}{d^3}+\frac{4\varepsilon\rho^2}{d^2}\right)\right] \tag{4.53}$$

If the mirror apertures are small, a fraction of the incident light will not be transmitted. Increasing the mirror aperture leads to an increase in effective transmission. However, rays entering at different points will experience different phase lags, and this leads to a broadening of the fringes at finite apertures. For a small far-away source on the optical axis, the spread in path length follows from eq. 4.53:

$$\Delta_s = \rho^4/d^3 \tag{4.54}$$

At an aperture of λ/F most of the light is transmitted, with a reduction in finesse of about 30%. This gives a practical maximum for the aperture size:

$$\rho_s = \frac{\lambda d^3}{F} \tag{4.55}$$

The confocal separation needs to be set quite exactly, to within a few micrometers. A translation of the mirrors over $\lambda/4$ scans across the free spectral range, and a translation of $\lambda/(2F)$ across the half-width of a fringe peak. The maximum path length difference for rays entering at different points is:

$$\Delta_\varepsilon = 4\varepsilon\rho^2/d^2 \tag{4.56}$$

This should be smaller than the displacement required to scan across the fringe peak, and this gives the following condition for ε:

$$|\varepsilon| \le \frac{\lambda d^2}{8\rho^2 F} \tag{4.57}$$

By choosing a small negative value of ε, the higher order terms in eq. 4.53 are of opposite sign and the total fringe broadening due to the finite aperture will be reduced.

4.4.2 Finesse and free spectral range

Analogously to the plane Fabry-Perot, a finesse and a free spectral range can be defined for the confocal Fabry-Perot, where again the finesse is the ratio of the free spectral range to the fringe width.

The expression for the finesse of a confocal Fabry-Perot follows from the plane mirror finesse (eq. 4.15) by substituting R^2 for R:

$$F_0 = \pi\frac{\mathbf{R}}{1-\mathbf{R}^2} \tag{4.58}$$

The free spectral range is found by substituting the four-transit path length into eq. 4.19:

$$(\Delta\lambda)_{\mathrm{FSR}} = \frac{\lambda_0^2}{4n}(d+\varepsilon-\tfrac{1}{4}\rho^4/d^3-4\varepsilon\rho^2/d^2) \tag{4.59}$$

For a reflectivity close to unity the finesse of a confocal Fabry-perot is is approximately half that of an otherwise identical plane interferometer. However, as the free spectral range is also halved, the resolving power remains the same for both types.

In practice, the finesse of a confocal Fabry-Perot is reduced by defects. Bearing in mind that for a given reflectance of the mirrors the reflectivity finesse is smaller than for a plane interferometer, defect broadening is essentially the same as for the case of a plane interferometer.
The above holds true for surface imperfections, shape errors and vibrations. The effect of angular misalignment however, is radically different for plane and confocal Fabry-Perots.

For a plane Fabry-Perot, non-parallelism appears as a variation in mirror separation over the aperture, and significantly broadens the profile even for a misalignment of just a few mrad. For spherical mirrors this is not the case: a small angular misalignment merely redefines the optical axis, and appears as a perturbation in the exact confocal separation.

5 Plasma etching

In the microelectronics industry, there is a constant demand for faster and smaller Integrated Circuit (IC) devices, which has led to a continuing reduction in feature sizes. This sets high standards for all the production stages, and especially for the etching process, which has become the defining step for the attainable feature size.

In section 5.1 the requirements on the etching process are outlined. It will be shown that RF plasmas are well suited for anisotropic etching. These plasmas are very complex systems, in which the electrode geometry, gas nature, pressure, power are all important parameters. In section 5.2 and 5.3 general plasma characteristics and processes will be discussed. In section 5.4 the RFI etching plasma is described. Finally, in section 5.5, several plasma diagnostics for the determination of the electron density are discussed.

5.1 Dry etching

Traditionally, microstructures were applied by wet etching. A mask pattern is reproduced in the surface layer by exposing the uncovered material to a chemically reactive liquid.
The main drawback of this technique is that the liquid has no preferential etching direction. The etching process is isotropic, and as a result undercutting of the mask takes place. Undercutting is not a big problem, as long as the aspect ratio (heigth-to-width ratio of the features) remains small. Reducing the feature sizes however meant larger aspect ratios, and anisotropic etching techniques were needed.

In the early 1970s an alternative to wet etching was developed, in which radicals and atoms, formed in a plasma, reacted with surface atoms. If the reaction products are volatile, spontaneous etching will occur. This so-called dry etching offered better process control, but still the etching process remained isotropic.

Plasma etching can be made anisotropic by making use of the charged ions, instead of chemically active species. If an electric field is applied perpendicular to the surface, the ions are accelerated and they will strike the surface with a high kinetic energy, thereby removing atoms from the surface. This physical etching process is called sputtering. Due to the well-defined direction of the ions, sputtering will be anisotropic.
Drawbacks of sputtering are the low etching rates, and the risk of surface damage due to the impact of high-energetic ions.

Ion-assisted etching is the combination of these two dry etching mechanisms: the actual etching is chemical and the ions enhance the rate of the chemical surface reactions. Ion-assisted etching can thus have a very high etch rate in addition to being anisotropic. This process can also be used when the chemical reaction products are not volatile.

Etching requirements

Nowadays, ion-assisted etching is the standard technique in IC manufacture. In an industrial etching reactor, economic considerations of cost and speed require the reactor to be able to etch as many IC's as possible simultaneously, which has led to large wafer sizes, of 25 cm or more.

In summary, the following requirements are set for etching plasmas:

- high etch rate
- anisotropic etching
- uniform etching over the entire wafer
- high selectivity
- no surface contamination or damage

The etch rate of ion-assisted etching increases with higher ion energies. However, for very high ion energies, surface damage may occur. The ion energy distribution is determined mainly by the sheath conditions (*snijkers93*).
The anisotropy of the etching depends on the angular distribution of the incident ions, which is determined by the plasma conditions and most specifically by the sheath (*sambeek93*). In a collisionless sheath, the ions will strike the surface perpendicularly. If the ions undergo collisions in crossing the sheath however, they will be scattered under a given angle and lose energy; this decreases the etch rate and results in undercutting.
In section 5.4 the plasma sheath will be discussed in more detail, and it will be shown that to minimize the effect of collisions, etching plasmas should be operated at low pressure and high sheath potential.

If the etching is to be uniform over a large surface area, the plasma conditions also must be uniform. This places high demands on the geometry of the reactor and the coupling of power into the plasma.

As stated above, surface damage can be avoided by controlling the energy of the ions. To prevent thermal damage to the wafer, the overall temperature of the plasma should remain fairly low. In practice this means the use of cold plasmas, with a low degree of ionization.
Surface contamination can have many sources. Ion energies should remain low to prevent sputtering of the walls, and the reactor must be clean and completely dust-free. A complicating factor is that many etching plasmas generate dust particles themselves (*stoffels94*).

The selectivity of the etching process is the ratio of the etch rate of the wafer material to the etch rate of the mask material. The selectivity can be made almost arbitrarily high by a proper choice of etching gases and plasma conditions.

As silicon is not a good conductor, direct currents in the plasma will lead to charging of the wafer, which eventually will end the ion flux. This can be prevented by periodically alternating the current, i.e. by using an AC plasma. The most common excitation frequency is 13,56 MHz, which is sufficiently high to prevent direct heating of the ions, thus keeping the plasma cold.

5.2 Plasma definitions and classification

Plasma can be considered to be the fourth state of existence, besides solids, liquids and gases. Basically, it shows most resemblance to the gaseous phase, but is distinct in the respect that a plasma contains a significant amount of charged particles, namely free electrons and ions.
At first sight, one might think plasma is an exclusive state of matter found only in laboratories, but actually almost all the universe is filled with plasma. It is found in the interiors of stars and also in the interstellar hydrogen; on earth it occurs naturally in lightning bolts and flames, and artificially in lighting tubes.

The plasma state can be defined as follows (*chen84*):

"A plasma is a quasineutral gas of charged and neutral particles which exhibit collective behavior."

The collective behavior in this definition is a result of the Coulomb forces between the charged particles in a plasma. In a gas the particles move around, undisturbed until they actually collide with another particle. In contradistinction, in a plasma the movements of charged particles generate electromagnetic fields, which affect other charged particles far away by the long-range Coulomb interaction. Motion in a plasma thus not only depends on local conditions but also on the status in remote regions: aplasma displays collective behavior.

The notion of quasineutrality refers to the fact that although the plasma contains charged particles, it will be essentially free of potentials or fields. This is because the number of negative and positive particles will be approximately equal over any reasonably large volume, and the volume as a whole will be neutral. Significant deviations from neutrality will generate high electric fields, which will swiftly restore neutrality.

Temperature and velocity

The particles in a plasma, whether charged or not, obey the laws of gas kinetics, and in thermal equilibrium the velocity distribution of the particles is given by the Maxwell-Boltzmann distribution. The mean velocity can be found by integration of this (*roosmalen91*):

$$\langle v \rangle = \sqrt{\frac{8kT}{\pi m}} \qquad (5.1)$$

In thermal equilibrium the mean velocity of the electrons will be much higher than that of the ions, because of the large mass difference. A consequence of this is that the flux of electrons through a given area in unit time will be much higher than the ion flux, which plays an important role in the interaction of a plasma with the confining walls.

The average kinetic energy of the particles is:

$$E_k = \frac{1}{2}m\langle v^2 \rangle = \frac{3}{2}kT \qquad (5.2)$$

This relationship between kinetic energy and temperature defines the temperature of each kind of particle in the plasma. In plasma physics it is therefore customary to give temperatures in units of energy rather than kelvins. The energy corresponding to kT is then used to denote the temperature. The conversion factor is:

$$1\ \text{eV} = 1{,}6.10^{-19}\ \text{J} = 11600\ \text{K}$$

One has to bear in mind that a plasma can have several temperatures at the same time. Due to the large mass difference, impulse transfer between electrons and heavy particles is inefficient, and the electrons can have a much higher average kinetic energy under certain conditions. The electron temperature will then be much higher than the temperature of the atoms and ions.

Debye length

Each individual charged particle will disturb quasi-neutrality in its immediate vicinity. It will therefore be surrounded by charged particles of opposite sign. Their combined electrostatic field will be a multipole field, which falls off much more swiftly with distance than the monopole field generated by an isolated particle. The distance at which this fall-off becomes significant is called the Debye length.

The Debye length is a measure of the shielding distance in the plasma; charge fluctuations can only occur within this length. The Debye length is a function of electron density n_e and temperature T_e (*sijde89*):

$$\lambda_D = \sqrt{\frac{\varepsilon_0 k T_e}{N_e e^2}} \qquad (5.3)$$

plasma frequency

An important parameter, especially in AC discharges, is the plasma frequency of the charged particles. This is the angular frequency of the oscillation brought about by a deviation of charge neutrality. Assuming charge separation cannot occur over a distance greater than the Debye length we find for the plasma frequencies (*sijde89*):

$$\omega_{pe} = \sqrt{\frac{N_e e^2}{m_e \varepsilon_0}} \qquad (5.4)$$

and:

$$\omega_{pi} = \sqrt{\frac{N_i e^2}{m_i \varepsilon_0}} \qquad (5.5)$$

These are exactly the same as the plasma frequencies defined in the section on dispersion in this thesis! This is as should be, since both results are obtained from the effect of oscillations under the influence of an electric field. In the case of dispersion the electric field was externally applied, whereas here the field is generated by the motion of the particles themselves.

plasma criteria

From the Debye length two criteria for a true plasma can be deduced. Firstly, there must be enough particles in the vicinity of the charge for the equation for the Debye length to have statistical validity. This condition relates electron density and temperature (*chen84*):

$$(1{,}38.10^6)\sqrt{T_e^3/n_e} \gg 1 \qquad (5.6)$$

A second plasma condition is that the Debye length should be small compared to the characteristic length of the plasma L_p: $L_D \ll L_p$.

Finally, we demand that in a plasma particle motion should be governed by electromagnetic forces rather than collisions, which is expressed by the condition:

$$\omega_e > \nu_e = \frac{e}{m_e \mu_e} \qquad (5.7)$$

where ν_e is the electron-neutral collission frequency, and μ_e the elctron mobility.

classification

From the criteria above, a classification of plasmas can be derived. Both the Debye length and the plasma frequency are functions of two parameters, the electron density N_e and temperature T_e. A plasma can thus be characterized by these two parameters.

However, the neutral particles should not be ignored, as in many plasmas these neutrals are in the majority. The ratio of charged particles to neutrals is called the degree of ionization α:

$$\alpha = \frac{N_e}{N_e + N_a} \tag{5.8}$$

If the ionization degree is low ($\alpha<10^{-2}$), there are so few charged particles that collisions of charged particles with each other are less frequent than collisions with neutrals. The electron temperature wiil then be much higher than the temperature of the atoms and ions.
Because the heat capacity of the plasma is determined by the most populous species, which for $\alpha<10^{-2}$ are the neutrals, the plasma as a whole is termed "cold", despite the high electron temperature. In a fluorescent tube for instance, $T_e \approx 10^4$ K, but still the tube does not feel hot. Cold plasmas are well suited for etching (and deposition) because the low plasma temperature prevents thermal damage to the sample, while the high electron temperature increases the amount of reactive radicals.

For strongly ionized plasmas, the collisions between charged particles become dominant, and the electron and ion temperatures will quickly reach equilibrium. The ions furthermore will efficiently transfer energy to the neutrals, and a state of thermal equilibrium will be reached. we then speak of a "hot" or thermal plasma. Thermonuclear and welding plasmas fall into this category.

5.3 Plasma processes

5.3.1 plasma generation

The simplest way to generate a plasma, is to apply a large potential difference over a region of gas. Charged particles in the gas will be accelerated by the electric field and thereby gain momentum. When they reach a sufficiently high energy, a collision with a neutral particle will lead to ionization. With every such collision more charged particles are created, and if the electric field is high enough, an avalanch effect occurs. We then speak of electrical breakdown or discharge.
The insulating gas will then become electrically conductive, and a current of charged particles will flow through it. If the applied potential difference is constant in time, the direction and magnitude of the current too will be constant. Therefore this type of plasma is called a DC discharge.

The basic mechanism for establishing and maintaining a plasma is thus ionization:

$$e^- + A \Rightarrow 2e^- + A^+ \tag{5.9}$$

The reverse process is three-body recombination:

$$e^- + A^+ + B \Rightarrow A^* + B \tag{5.10}$$

where the newly formed neutral will generally be in an excited state, denoted by A^*. A third particle B is needed to carry off the excess momentum. If the recombination occurs at one of the confining walls this momentum can be absorbed by the wall and B is not needed. In most low-pressure plasmas, wall recombinations will be predominant.

5.3.2 Plasma chemistry

The plasma chemistry is determined by molecule-molecule interactions and by collisions of electrons with molecules. Electron-molecule collisions are a specific feature of the plasma state; in such collisions molecules can be ionized, but also dissociated. Dissociation leads to the formation of chemically reactive radicals, which play a major role in etching as well as in deposition.

Apart from these surface processes, radicals are lost from the plasma by association, in which they again form molecules. The probability of radical formation is proportional to the number of free electrons in the plasma, while the association rate depends on the particle density.

Low plasma pressure and a high electron density will thus lead to a large concentration of radicals and a chemically active plasma.

5.3.3 Sheath formation

The discharge is usually generated between two electrodes. The bulk of the plasma (called the glow region) will be quasineutral, but near the electrodes a region of positive space charge will be formed, called the sheath.

The formation of a sheath is caused by the difference in thermal velocity between electrons and ions. When ions and electrons strike the electrode surface they recombine and are lost from the plasma. Electrons have a higher velocity and are removed from the plasma faster, leaving the plasma with a net positive charge. By this process, each electrode will develop a negative potential with respect to the plasma. The resulting electric field will slow down the electrons and accelerate the positive ions, until an equilibrium is reached. Because of shielding, the potential drop will be confined to a few Debye lengths, and this region is called the sheath.

If a voltage is applied over the electrodes, the potential drop will be accomodated entirely within the sheaths. The plasma glow will have a constant potential because of its quasineutrality; this constant potential is called the plasma potential. The plasma potential will always be higher than the potential at either electrode, regardless of the absolute value of the electrode potential.

The bulk of the plasma will be approximately field-free, so the charged particles move around randomly with thermal velocity. If they enter the sheath region however, the electrons will be reflected back into the plasma, while the positive ions are accelerated towards the surface.

In plasma etching, the kinetic energies of the ions striking the surface play an important role in etching rates, etching anisotropy, etching selectivity, and surface damage. In a cold plasma, the thermal velocity of the ions can often be neglected, and the kinetic energy of the incident ions is determined by the sheath characteristics, and particularly by the potential drop over it.

Another consequence of the sheath potential barrier is the repulsion of negative ions, effectively trapping them inside the plasma glow. This results in prolonged lifetimes for these negative particles, which plays an important role in the formation of dust in RF etching plasmas (*stoffels94*).

A basic model for the sheath region can be set up by solving the Poisson equation for the sheath region, assuming a Maxwell-Boltzmann velocity distribution in the plasma (*chen84*, *roosmalen91*, *snijkers93*).

5.3.4 Autobias voltage

If the surface areas of the electrodes are equal, the discharge will be symmetrical and the voltage drop over both sheaths will be the same. If the electrodes differ in area, an autobias voltage will be generated, which will depend on the surface ratio. The smaller electrode will develop a higher voltage drop over the sheath than the larger electrode. In industrial etching, this set-up is normally used with the substrate on the smaller electrode, as this leads to higher ion energies at the substrate and thus better etching results.

5.3.5 AC discharges

If the potential difference between the electrodes is varied harmonically in time, an alternating current will flow through the plasma and we speak of a AC discharge. A major difference with the DC discharge is that the net current through the electrodes will be zero, and the electrodes need no longer be conductive. This offers major advantages in the use of a plasma for the etching of dielectrics.

The behaviour of the plasma is largely governed by the sheath regions. The positive ions diffuse towards the sheath edge and are subsequently accelerated out of the plasma, whereas the electrons are repelled. The electrons which are accelarated into the plasma glow, are the driving mechanism of the plasma.
The sheaths vary in time with the applied RF voltage, changing in thickness from a certain maximum to zero, when the plasma potential equals the electrode potential. At zero sheath thickness electrons will be able to reach the electrode.
As there is no net current, the total number of electrons reaching the electrode in these short intervals equals the total number of positive ions, which bombard the surface continuously.

The frequency at which RF discharges are usually operated is 13,56 MHz, which is an internationally allowed industrial frequency. This is typically higher than the ion plasma frequency, and lower than the electron plasma frequency: $\omega_{pi}<\omega<<\omega_{pe}$. The electrons are able to follow the field oscillations, while the ions will only experience a time-averaged field with a time dependent perturbation.

By keeping the electric field lines in the sheath perpendicular to the substrate to be etched, excellent anistropy can be attained with RF discharges. The pressure should be kept low to avoid collisions of energetic ions within the sheath, as these reduce the etch rate and introduce a ion velocity component parallel to the surface. This gives rise to undercutting and isotropic etching.

5.4 Inductive coupling: the RFI discharge

To increase the etching rate of an RF discharge, the voltage over the electrodes has to be increased. This leads to high ion energies, and surface damage as well as increased wall sputtering might result. Replacing the capacitive coupling by inductive coupling results in a high electron density with relatively low loss. Moreover, plasma generation and ion energy can be independently controlled through RF biasing of the electrodes.
Modern radiofrequent inductively coupled (RFI) plasmas feature electron densities typically above 10^{17} m^{-3}, excellent uniformity over large wafer diameters, as well as low and controllable ion energies (*hopwood92*), using the well-known technology of capacitively coupled sources.

The principle of inductive coupling is that the time-varying magnetic field, generated by the RF current in an induction coil, induces a solenoidal electric field in the plasma. This electric field accelerates the free electrons and sustains the discharge.
Because the field is non-conservative, the electrons can gain energy from the field without collisions. This makes inductive coupling suitable for creating and sustaining plasma at very low pressures. This offers an advantage over other plasmas, as lower pressures give a better control of the etching process.

!!

The penetration depth of the RFI excitation field is (see appendix for a derivation):

$$\delta = \frac{c}{\omega_p}\left(1 + \frac{3\nu^2}{8\omega^2}\right) \qquad (5.11)$$

provided $(\nu/\omega)^2 \ll 1$, which is satisfied by a cold, low-pressure plasma.

The consequence is that the solenoidal electric field exists only in a very thin layer of plasma adjacent to the induction coil. This allows the sample to be placed very close to the source of the ions, without loss of anisotropy, which would be caused by ions with a velocity component parallel to the surface.
This means that relatively few ions are lost during transport to the substrate and high etching efficiencies can be attained. A drawback is that most of the heat will be dissipated close to the quartz window which separates the plasma from the induction antenna.

As high voltages will appear across the antenna coil, there will be some capacitive coupling to the plasma. This should be avoided, as it will decrease the efficiency of the coupling (*hopwood94*). The effects of capacitive coupling is most important at low power levels. A radially slotted Farady shield can be placed between the antenna coil and the discharge to short out the capacitive component.

Finally, the uniformity of the plasma can be further increased by using magnetic multipoles to achieve magnetic confinement. This becomes important when large wafers (d>5 cm) are etched.

5.5 Determining the electron density

A plasma is an extremely complex system, and many parameters need to be taken into account to adequately describe its characteristics. Determination of these parameters is done by measurements of a wide variety of plasma phenomena. In the case of etching plasmas, extra complications arise, as typically several species are present in the plasma, along with their associated radicals and ions, and free electrons.

5.7.1 Plasma diagnostics

No one diagnostic technique is capable of measuring all these different parameters accurately at all plasma conditions: which diagnostic should be used, is decided by the specific plasma under study.
In the table below, the most fundamental plasma parameters are listed, along with their respective diagnostic principles (after *hutchinson87* and *kroesen93*):

- electron density N_e	interferometry, light scattering, probe
- electron temperature T_e	light scattering, probe
- electron energy distribution	probe, emission spectroscopy
- ion density N_i	probe, light emission
- ion energy dustribution	probe, laser induced fluorescence
- neutral density N_a	interferometry, gas pressure
- ion temperature T_i	probe, light emission
- electric field	ion beam deflection, probe
- magnetic field	interferometry, hall probe

This thesis is concerned only with the determination of the electron density in a RFI plasma, which is probably the most important parameter in an etching plasma. Free electrons can be considered to be the motor of the plasma, as key plasma processes like ionization, excitation and dissociation are mostly caused by electrons, which are accelerated in the electric field.
Below, some current techniques to determine the electron density are discussed in more detail: the Langmuir probe, Thomson scattering, microwave resonance and interferometry.

5.7.2 Langmuir probe

The Langmuir probe is a very useful and versatile plasma diagnostic. In its most elemental form the Langmuir probe is simply a small conducting surface, which is inserted into the plasma. An adjustable bias voltage is applied to the probe, and the current-voltage characteristic is measured. Its main advantage is that it gives local values of several plasma parameters in the vicinity of the probe, which cannot be obtained by other techniques. The plasma parameters which can be measured with a Langmuir probe include the electron density and temperature, the ion density and temperature, the plasma potential, and the velocity distribution functions for both electrons and ions. The Langmuir probe has a large dynamic range, with a detection limit for N_e around $10^{16}m^{-3}$.
A major drawback of the Langmuir probe is that it is an intrusive method, and in order to interpret the probe measurements correctly, one must have a realistic theoretical model to convert the measured probe data to the plasma characteristics. This holds especially true in the case of RF plasmas, where the time-varying plasma potential needs to be taken into account.

Insertion of the probe into the plasma leads to a local perturbation of plasma conditions and the formation of a sheath around the probe tip. If the pressure is low, collision-less sheath theory can be used to deduce the plasma parameters (*hutchinson87*). The electron density follows from the saturation ion current I_S, which occurs for sufficiently negative bias voltages (*chen84*):

$$N_e = \frac{2 I_S}{eA\sqrt{kT_e/m_i}} \tag{5.12}$$

in which A is the surface area of the probe, and T_e the electron temperature, which can be deduced from the slope of the current-voltage characteristic. Inaccuracies in determining T_e can result in significant errors in the electron density, as a comparison of a probe with Thomson scattering has shown (*meulenbroeks94*).
The above equation only holds under severe conditions: the plasma is stationary, the probe surface remains clean, the sheath thickness is small compared to the probe dimensions and there are no collisions within the sheath.
Collisions within the probe sheath and other problems can be overcome by incorporating them into the sheath model, which is not trivial however. Modification of the probe surface can be a problem in thermal plasmas, but also in cold, chemically reactive plasmas, such as etching plasmas.

In an RFI discharge, the plasma is definitely not stationary. This causes severe problems for probe interpretation, as the variations in electron current are anharmonic. The best solution then is to drive the probe with its own RF bias voltage. The phase and amplitude of the probe RF voltage are adjusted to give a maximum floating potential: the probe voltage can then be assumed to be equal in both phase and amplitude to the local RF plasma potential, and one may interpret the probe characteristic as if the plasma was stationary.

5.7.3 Thomson scattering

Thomson scattering is the elastic scattering of light by free electrons. This technique is non-intrusive, has a good spatial resolution, and requires no model assumptions on plasma equilibrium etc. A good spatial resolution can be attained by detecting the scattered light at right angles to a narrow laser beam directed through the plasma.
One of the drawbacks of Thomson scattering is the low signal level, necessitating the use of a powerful laser. Its detection limit is determined mainly by stray light and lies around 10^{18} m^{-3}(*meulenbroeks94*). If need be, spatial resolution can be traded off against signal level by imaging the entire laser-irradiated plasma volume.

The wavelength will show a Doppler shift due to the thermal motion of the electrons. Measuring the broadening of the scattered profile thus yields the electron temperature.
The measured profile will also contain a contribution from elastic scattering at bound electrons (Rayleigh scattering). At low degrees of ionization the Thomson scattering profile needs to be isolated from this Rayleigh contribution by deconvolution.

In order to determine the electron distribution in the plasma, one has to be able to shift both the laser beam and the detector with respect to the plasma. When working with a closed plasma cavity however (as is the case in the ETS-I set-up, see chapter 8), the access to the cavity will be limited to a few slots, and the Thomson scattering technique can only be used to monitor a radially fixed position.

5.7.4 Microwave resonance

If the electrodes around the plasma are extended to form a hollow conductive enclosure, we speak of a plasma cavity. Such a cavity has a set of discrete resonance frequencies, which depend on the index of refraction inside, and thus on the electron density in the plasma.

If the electron density is changed the resonant frequency will shift, and the change in electron density can be determined from measurements of the shift in the resonant frequency of the cavity (*stoffels94*):

$$N_e = \frac{2 m_e \varepsilon_0 \omega^2}{e^2} \frac{\Delta\omega}{\omega_0} \qquad (5.13)$$

Here N_e is the electron density, averaged over the electric field within the cavity. There is no spatial resolution, which is a major drawback of this technique. To lessen the effect of the exact geometry of the cavity, a convenient electromagnetic mode, like the TM_{020} mode, can be used, so the observed frequency shift will reflect mainly the electron density in the central part of the plasma.

The equation is valid only when the electron density is small (N_e<5.10^{16} m^{-3}, *stoffels94*). For higher electron densities, the electromagnetic mode will deform too much because of polarization effects.

5.7.5 Interferometry

The possibilities and problems of optical interferometry in establishing the electron density of a plasma, have been thoroughly discussed in section 2.3. It was shown there that for spatially resolved measurements of the electron density in etching plasmas, infrared light should preferably be used. The upper wavelength limit is set by technological considerations, and the lower limit is determined by either mechanical stability or atomic contributions to n.
Using infrared light the detection limit can be of the order of 10^{16} m^{-3}, while maintaining a good spatial resolution (as shall be demonstrated in section 7.5.2).

It is not possible to measure truly local densities with interferometry, as in effect the line-integrated density over a spatially resolved chord is measured. From these chord densities, a radial density profile can be determined by Abel inversion.

If microwaves are used instead of infrared light, we speak of microwave interferometry. In that case vibrations become unimportant, and the refractive index of the plasma depends only on the free electrons. However, the spatial resolution is poor. Microwave interferometry is discussed at length in the PH.D. thesis of Hugenholtz (*hugenholtz90*), and in Plasma Diagnostics, vol 1A (*meuth89*).

6 The experimental set-up

During the project the ETS-I etching reactor was modified to a RFI plasma source. In this chapter, the reactor and the plasma source are described. Section 6.1 and 6.2 deal with the vacuum system, and section 6.3 and 6.4 descibe the plasma source. An operation manual for the set-up can be found in the appendices.

6.1 Vacuum theory

Typical operating pressures for RF-HD plasmas lie in the range of 1-100 mtorr. To ensure a clean and reproducible plasma, background gas effects should be negligible. Moreover, the etching reactor should remain free of dust particles and other contaminants. A good vacuum system, capable of attaining a base pressure below 10^{-5} torr, is therefore an essential part of a plasma etching installation.

6.1.1 Pumping and pressure

To attain and maintain a vacuum, pumps are attached to the reactor vessel. For the high vacuum range, one basically has the choice between oil diffusion pumps and turbo molecular pumps. Both require roughing pumps. For this, rotary vane pumps are commonly employed, sometimes in series with a Roots blower. Together with the reactor vessel, connecting tubes, valves and other vacuum components, these pumps form the vacuum system.

In a high vacuum system the attainable end pressure is limited by outgassing and (small) leaks. Outgassing is the slow desorption of (mainly) water molecules from the walls of the vacuum system. This process is strongly temperature dependent and the walls can be largely cleared of adsorbed molecules by temporarily heating the entire vacuum system (baking). The system has to be baked after each exposure to air, else water desorption will severely limit the high vacuum quality, even in a perfectly leak-tight system.
The end pressure in the vacuum system is determined by the equilibrium between leak rates, gas desorption and the pumping speed S_p of the pump.

If the pump is connected to the vacuum vessel with a tube of conductance C, the effective pumping speed is reduced to S_{red}:

$$\frac{1}{S_{red}} = \frac{1}{S_p} + \frac{1}{C} \qquad (6.1)$$

By varying the conductance of the connecting tube, the effective pumping speed and thus the equilibrium pressure in the vessel will be changed. This principle is often used in pressure control, where the conductance is usually regulated by the partial closing of a valve.

6.1.2 Pressure gauges

For vacuum systems, many different pressure measurement principles exist, each with its own specific pressure range. For many types of gauges the pressure reading depends on the nature of the molecules, atoms and ions present in the gas. This effect should always be borne in mind and if need be corrected for.

In most pressure gauges the pressure is derived from measurement of a pressure-dependent property of the gas, such as thermal and electrical conductivity or the ionization probability. These properties depend on the nature of the gas particles as well as on the pressure, and the instrument reading will generally not be the same for different gases. In the case of plasmas the ionization degree can also influence the reading of gauges. In the rough to high vacuum range, the most widely used indirect pressure gauges are the Pirani and the Penning.

A Pirani gauge measures the thermal conductivity of the gas, which is related to the pressure through the mean free path of the gas particles. Above 10 torr, thermal heat transfer by convection is independent of gas pressure, and at very low pressures, convective heat transfer will become small with respect to radiative losses, and again the heat flow will be independent of pressure. This limits the working range of the Pirani to pressures of 10 to 10^{-3} torr.

The Penning, or cold-cathode ionization gauge, measures the discharge characteristics of the low-pressure gas. Above 10^{-2} torr, the discharge changes to a glow discharge in which the current no longer depends on pressure. Sorption and cathode sputtering effects limit the accuracy of the Penning and set a practical lower limit of about 10^{-8} torr.

6.1.3 Direct pressure gauges

In a direct (or absolute) pressure gauge the force of the gas particles acting on a known area is measured. By definition the quotient of this force to the area is equal to the pressure of the gas. An absolute pressure gauge is thus essentially independent of gas nature. Direct pressure gauges are mostly limited to the rough vacuum range, as fundamental mechanical considerations limit their accuracy at lower pressures. One of the most accurate direct pressure gauges for the high vacuum range is the Baratron.

The Baratron capacitance manometer consists of a fixed electrode and a diaphragm. One side of the diaphragm is exposed to the pressure to be measured, while the other side is kept at zero reference pressure.
The diaphragm is pushed towards the electrode by the pressure, and this results in a change in capacitance between electrode and diaphragm. The capacitance can be measured electronically with great precision, enabling accurate determination of the pressure.
As the Baratron is very sensitive to variations in ambient temperature the entire gauge, including the electronics, should be mounted in a temperature-stabilized housing. Mechanical vibrations are interpreted as pressure variations by the Baratron, so the gauge should be isolated from vibration sources.
If temperature and vibration effects are suppressed, the Baratron can measure pressures down to 10^{-5} torr, dependent on the reference pressure. For higher pressures the deformation of the diaphragm becomes strongly non-linear. This determines the upper limit; the dynamic range is typically 5 decades. Apart from its low measurement limit, another major advantage of the Baratron over other absolute pressure gauges is its electronic output signal. This means the Baratron can easily be incorporated in an automated monitoring system.

6.2 The vacuum system

6.2.1 The etch reactor

The plasma cavity is situated inside a cylindrical stainless steel vacuum vessel, the etch reactor. In the side walls of the vessel several ports and windows are available for pumping, viewing and diagnostical purposes. The vessel itself is open both at the top and the bottom end. The top side is closed by a mass spectrometer unit, the detector chamber of which is connected to the plasma cavity by a pinpoint hole (40 µm across) in the centre of the sample electrode. The bottom side is closed off by a specially designed flange, with a recess to accomodate the RFI-antenna, and a quartz window to allow the coupling of RF power into the reactor.

During operation the reactor vessel rests on a platform, which can be moved in 2 dimensions by stepper motors. This makes it easier to perform spatially resolved optical diagnostics as the alignment of the optical components remains undisturbed. The interior of the vessel can be accessed by lifting it off its bottom flange with a chain pulley. An alternative way to work inside the vessel is to remove the large front window.

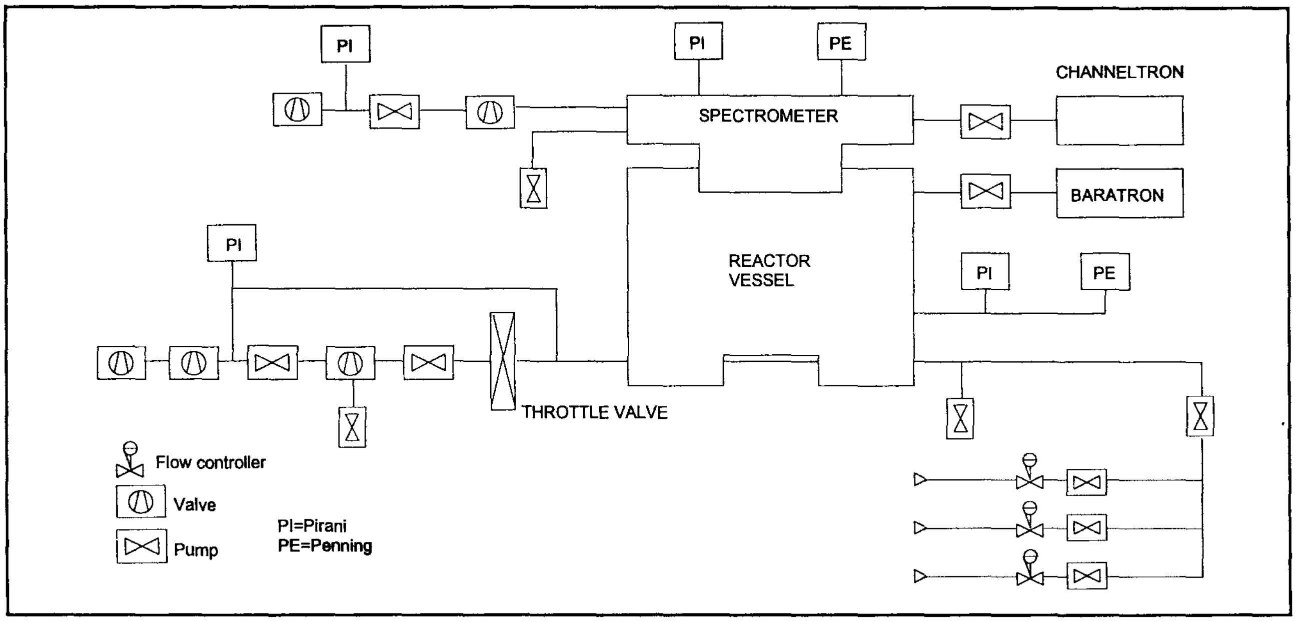

Figure 6.1: the vacuum vessel

The reactor chamber is pumped by a Balzers TPH-510 turbo molecular pump in series with a Pfeiffer WKP 250 roots blower and a Pfeiffer DUO 030A double stage oil diffusion pump during normal working conditions. When evacuating from atmospheric pressure, the turbo is by-passed, until the pressure is sufficiently low. The lowest attainable background pressure with the turbo at full speed is about 4.10^{-5} torr.

The detection chamber of the mass spectrometer is pumped by a Pfeiffer TPH 170 turbo molecular pump and an Pfeiffer UNO 012A primary pump, capable of reducing working pressure to below 10^{-6} torr. The pressure inside the mass spectrometer is not necessarily equal to the pressure in the main reactor chamber. This is possible because the connecting hole is extremely small and presents a huge pumping resistance. However, care should be taken to avoid bringing the reactor up to atmospheric pressure, with the mass spectrometer still at vacuum, as this might choke up the sample hole.

6.2.2 Computer control

In view of the complexity of the system and the fact that inexperienced students need to be able to operate it, the entire set-up has been automated: all components are controlled by PLCs (Programmable Logic Controllers). The PLCs are connected to a 486 PC, where dedicated software provides an interface to the experimenter. The program, Intouch Windowviewer, allows user-friendly control of the PLCs, and also provides a comprehensive overview of the actual state of the system.
The program has two modes of operation: manual and auto. The manual mode allows control of individual components through the PLCs. In auto mode two fully automated routines are available, namely 'pump down' and 'shut down', that are designed to take the system from atmospheric pressure to vacuum and back. In future other routines will be added.

Safety conditions are automatically monitored by the PLC unit. In case of a failure, the associated component will shut down automatically. Alarms are reported distinctly on the computer screen.

The PLCs can also be operated directly from the front panel of the PLC cabinet. In that case too the safety conditions will be monitored automatically. However, not all the relevant information will be available without a PC.

6.2.3 Pressure monitoring

The absolute gas pressure in the reactor chamber is measured with a MKS 370 HS-10 Baratron capacitance manometer, connected to a MKS 270A electronic/display unit. A Balzers TPR010 Pirani and a Balzers IKR020 Penning gauge are also connected directly to the vessel. The pressure in the pumping lines ia monitored by a TPR010 Pirani gauge at the Roots blower.

The Baratron was chosen as the reference pressure gauge because of its independence on gas composition. A drawback of the Baratron is its sensitivity to changes in the surroundings, necessitating daily recalibration of the electronic zero point. This is done by pumping the system down to as low a pressure as possible and subsequently adjusting the zero point so the Baratron reads the same pressure as the Penning gauge.
To reduce ambient effects upon the sensor, the Baratron is temperature-stabilized at 45 °C. It takes the sensor 4 hours to reach a stable thermal equilibrium, and in fact it is recommended to keep it powered continuously. The 370 HS-10 has a useable measuring range from 10 torr to 0,1 mtorr. The 270A display unit however, displays pressures down to 0,01 mtorr; the last digit thus should not be taken to be significant.
The pressure sensor is connected to the main chamber by a short, broad tube to avoid time delays in the monitoring of the system pressure. An isolation valve is installed to protect the sensor from overpressure and prolonged moisture contamination.

6.2.4 Pressure control

A set working pressure in the reactor can be maintained automatically, independent of gas flow rates. For this, an Alcatel VQ-6-ASA-T-SM throttle valve is placed between the chamber and the turbo pump, creating an adjustable pumping resistance. The pressure signal from the Baratron gauge is amplified by the MKS 270A and fed to a MKS 252 valve controller. The valve controller will compare the pressure signal to a preset value, and position the valve so that the actual pressure will be driven towards the set value.

The control circuit of the controller uses mainly proportional action, with an adjustable gain. Some derivative action can be added to the circuit to correct for the time delay. Initially however, one should aim to minimize the time delay by placing both the gauge and the throttle valve as close to the chamber as possible.

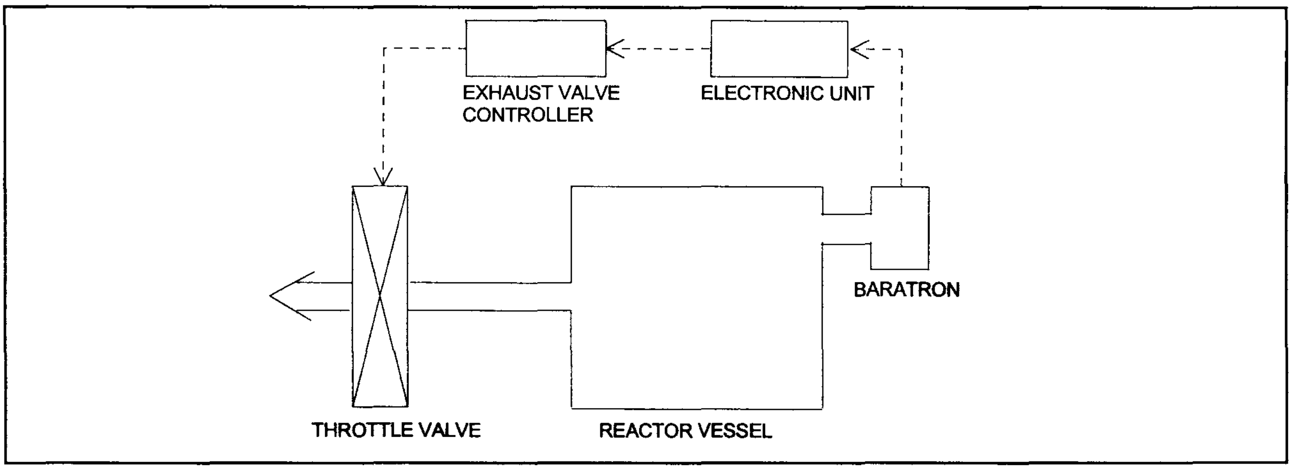

Figure 6.2: the pressure control circuit

Swift control action requires a high gain, but this might lead to pressure overshoots. These can be reduced by the derivative action. Too much derivative action however can lead to instabilities in the control circuit. Various pressures will generally require different control settings. Therefore, when using the system over a large pressure range, one needs to check the control performance for each pressure.

6.2.5 Gas handling

Up to three different gases can be combined in arbitrary proportions to create a large diversity of possible plasmas. In our initial experiments we will work with a simple single gas like argon, which gives a plasma that is fairly simple and well documented. Only in a later stage, when the dynamics of the plasma are better understood, real etching plasmas consisting of more than one component will be used.
The individual gas flows are regulated by Tylan FC 260 mass flow controllers, with a range of about 0-100 sccm. The gases are subsequently mixed by a manifold and the mixture is fed to the plasma cavity through 8 evenly spaced inlets in the lower electrode. The partial gas pressure in the gas mixture is proportional to its partial flow (*stoffels94*), provided the pumping speed is not gas-dependent.

Besides the installation for the process gases, a separate tubing system is installed to supply the system with nitrogen. Nitrogen is used for purging and venting purposes. If the vacuum vessel has been exposed to air for some time, repeated nitrogen venting and evacuating will be necessary to remove the bulk of the water residu from the system.

6.3 The plasma source

6.3.1 The antenna coil

The plasma is generated by inductive coupling of power from an antenna coil, consisting of three turns of hollow copper tube, through which cooling water flows. The coil is connected to the matchbox by 1 mm thick copper strips. The inductance of the coil is approximately L=1,2 μH (see appendix for a calculation of the inductance).

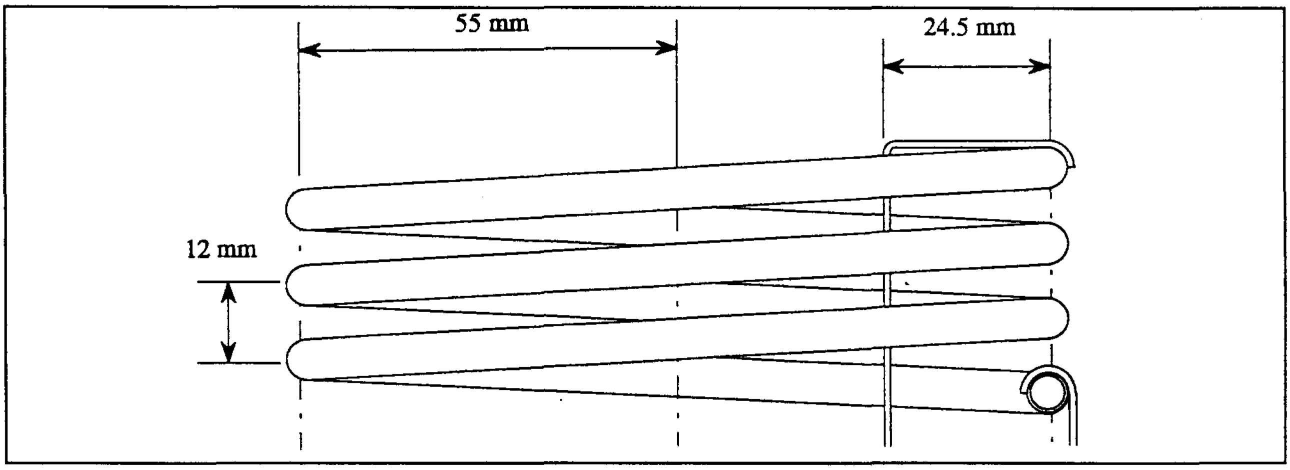

Figure 6.3: the coupling coil

To generate a RFI plasma large currents have to flow through the coil and the electrical circuit. These can lead to significant ohmic losses, which lead to a decrease in the power coupling efficiency. At RF frequencies, ohmic losses are even higher than at low frequencies, as the effective cross section of the conductors is reduced. This is caused by the small penetration depth of the electromagnetic fields and the resulting constrainment of currents to a thin surface layer (*jackson75*).

The copper coil is coated with a thin layer of silver to prevent the formation of CuO through corrosion. Otherwise, the ohmic resistance of the coil would be greatly increased due to surface currents, as CuO is a semiconductor with a large resistivity. Silver oxides are insulators and no such effect occurs.

The power coupling efficiency is a function also of the distance from coil to plasma. As their separation increases, the mutual inductance between the coil and the plasma decreases, and a larger current is required for the same plasma parameters. This gives rise to increased ohmic losses. To optimize the coupling efficiency, the coil should be as close to the plasma as possible. Therefore, the coil is placed directly adjacent to the vacuum window, which is 12 mm thick.

6.3.2 Electrode geometry

Large RF voltages exist on the antenna coil and this gives rise to a certain degree of parasitic capacitive coupling, especially at lower power levels. This results in a lowering of the coupling efficiency. To eliminate capacitive coupling from the antenna, a radially slotted metal Farady shield is installed directly on top of the window.

The sample to be etched is placed on an electrode, hanging upside down about 5 cm above the window. The separation between the window and the upper electrode is about 5 cm. A plasma cavity is formed by extending the Faraday shield with upright side walls. The cavity is cylindrically symmetrical. Eight vertical slots are machined into the side walls at equal intervals to accomodate the gas feedthroughs and provide access to the plasma for diagnostics.

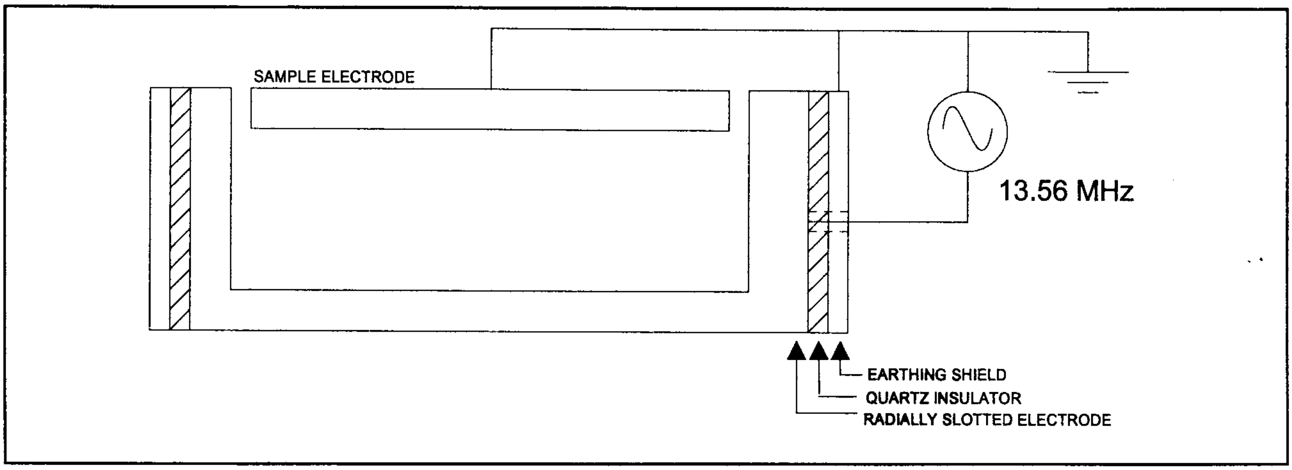

Figure 6.4: the electrode geometry

To control the plasma potential relative to the sample a bias potential is supplied to the electrodes. This bias has to be in phase with the plasma potential, so an adjustable RF source of 13.56 MHz is required to generate this potential. One can either bias the sample electrode, leaving the other electrode grounded (normal cavity), or one can ground the sample electrode, and drive the shield electrode with an RF bias (inverted cavity). As will be explained below, an inverted cavity is used, because of the mass spectrometer.

In our present experimental etch reactor, instead of a sample we have a tiny hole in the upper electrode, behind which a mass spectrometer is placed. This gives us the opportunity to study the ion energy distributions of the particles that would have hit the sample under normal operation. It is essential that the mass spectrometer potential is matched to the electrode potential. In practice, this means the sample electrode will be grounded along with the mass spectrometer, which gives an inverse cavity geometry (*snijkers93*).

6.3.3 The plasma source

The RF excitation voltage to sustain the inductive plasma is generated by a RFPP RF-20 power supply, with a maximum rated power of 2000 W. The mains power supply of the generator is PLC-controlled, so the generator shuts down automatically in case of a failure or alarm. Apart from its mains connection, the generator is a stand-alone instrument, with direct front panel control.

The RF-20 is controlled by its own microprocessor, which can be programmed to perform some simple functions like ramping and scaling of the power and pulsing. Alternatively, the generator output can also be controlled by external analog devices, as well as by a serial computer connection. As yet neither of these possibilities have been used.

Pulsed mode experiments using the generator's internal processor show it does not behave very well for short duty cycles and for low power levels. This will be expatiated upon in section 6.4.

Forward and reflected power can be read off the front panel of the generator, but it proved more accurate to measure these with a Bird 4410 directional power meter placed between the generator and the matching network.

As it is difficult to distinguish the power dissipated in the plasma from losses elsewhere in the

system, the power level of the generator is not a very good measure of plasma conditions. To garantuee reproducibility of the measurements the electron density rather than the generator power should be used (*stoffels94*).
However, as the diagnostic for the electron density was not yet available, we have taken the generator output and the reflected power as a measure of the plasma state.

6.3.4 Matching network

The generator has a fully resistive output impedance of 50 Ω to match the 50 Ω coaxial transmission lines. The plasma however has a variable complex impedance which depends on plasma parameters like pressure and applied power. This gives rise to unwanted reactive currents that do not contribute to the net power transfer to the plasma. Furthermore, part of the RF power will be reflected, giving rise to standing waves, which can damage the equipment.
Therefore, a RFPP AM-20 matching network is installed to adapt the plasma impedance to the generator output impedance. The network is of the 'L'-type, with a shunt capacitor to adapt the load and a series capacitor to handle the tuning; a fixed coil is included to increase the working range of the matching network. In our particular set-up a coil is used to couple power into the plasma, and the original coil has been shorted out.

The variations in the plasma impedance are matched by variable vacuum capacitors. These are driven by servo motors, which are controlled by phase-magnitude detectors. The control circuit automatically seeks an optimum, creating a hands-off tuning procedure.
In practice however, the control circuit proved to be unreliable in some situations, and operator control remained indispensable. In 6.4 the efforts to improve the automatic matching control are discussed.

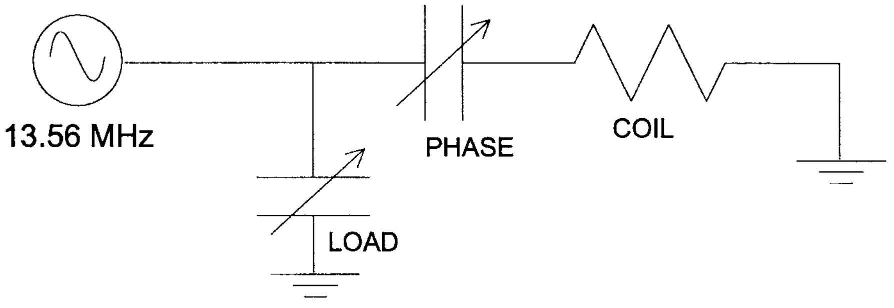

Figure 6.5: the electrical circuit

To achieve optimal matching, the network should be as close to the antenna as possible. This was achieved by connecting the antenna directly to its contacts in the box, without additional cables. A wide hole was drilled in the top cover plate of the matchbox to minimize field disturbances in the electromagnetic fields. The box was subsequently mounted directly underneath the bottom flange of the vacuum vessel.

6.3.5 RF radiation

When working with high-power RF sources, care must be taken to shield the laboratory environment from the RF radiation, which can interfere with computers and other sensitive devices. Furthermore, prolonged exposure can pose a significant health hazard. By connecting a simple wire loop to an oscilloscope we established there were small leaks of radiation from the windows in the reactor vessel, but these were sufficiently small.

However, significant stray RF radiation did come from the separating slit between the cover of the matchbox and the bottom flange. This problem was solved by replacing the screws in the matchbox cover by countersunk-headed screws, and inserting a viton ring with copper mesh wrapped around it between the two surfaces. By subsequently pressing the matchbox hard against the flange, a good electrical contact all around was created, and no further stray radiation was observed.

6.4 Practical plasma generation

After the plasma generator and the matching network were installed properly, some preliminary experiments were performed to get acquainted with the plasma source. These were done at low power levels without the Faraday shield in order to facilitate the ignition of plasma as much as possible. This means the coupling mechanism is predominantly capacitive.

At first, we did not manage to create a plasma at all. This was probably due to the fact that the matching network was originally designed to be used in conjunction with a capacitor, while we were using an inductor as a plasma source. Therefore we shorted out the fixed inductor, which we estimated to be approximately equal in inductance to our antenna coil. This resulted in the electrical circuit of figure 6.5.
We now did manage to create a plasma, with the fixed inductor shorted, but the automatic matching did not function properly. The series capacitor (for phase adjustment) always remained quite stable, but under some circumstances the shunt capacitor circuit (for load adjustment) became oscillatory. By carefully adjusting the gain settings of the magnitude control circuit, we managed to remedy this.
A more important problem however, was that the phase control circuit would sometimes become unstable and shoot through without returning to a stable point.

Although the automatic matching control did function most of the time, it was not fully reliable and operator control was still required. Controlling the matchbox by hand however, also posed some problems, as the load capacitor was extremely sensitive to the slightest variation. This might be caused by the shorting out of the fixed inductor in the matching network.

During one of these experiments at somewhat higher power (P=300 W), an electrical breakdown occurred within the matchbox, destroying one of the capacitor gear wheels and coating the matchbox interior, the antenna coil and the quartz window with soot. The soot was carefully cleaned off, and the capacitor gears were repaired with the help of Bob Sucharitkul of RFPP, who gave assistance by fax and telephone from England. The breakthrough was apparently caused by a weak soldering connection, which came loose and caused an arc to strike. As a precaution all unnecessary electrical components were disconnected, and the problem did not reoccur.

We also checked the heating of the quartz window, by taping a steel shielded thermocouple underneath the window. This is a vulnerable spot as a viton ring is used between the window and the flange as a vacuum seal, so the temperature should stay below 150 °C. It was found that even after prolonged plasma heating, the temperature did rise above 100 °C, but remained well below this limit. However, we did not use powers higher than 300 W, so the temperature should be carefully monitored if higher power levels are used.

Finally, we installed the Faraday shield to see if everything fit properly. As we did not have a bias generator, we had to keep the shield electrically floating in order to generate a plasma. Matching proved to be more difficult to achieve with the shield in place, but when a plasma was finally struck it was much brighter than without shielding. This is indicative of inductive coupling and apparently the shield does indeed reduce capacitive coupling, even when floating.

All in all, these experiments might seem somewhat incomplete, but the focus of this project was to design and build an optical diagnostic, rather than perfect the RFI plasma source. Therefore I did not pursue these experiments after the departure of David Vender, who left the university to return to Australia in the fall of 1994.

7 The Fabry-Perot interferometer design

A typical RFI plasma has electron densities in the range of 10^{16}-10^{19} m^{-3}, at a gas pressure of 1 to 100 mtorr. The considerations in section 5.5 indicate that the most promising method for determining the electron density in such a plasma would be infrared interferometry.

A Langmuir probe could be used to measure the local electron densities along the chord of the infrared laser beam, to establish the density profile; the integrated line density measured by the interferometer would then serve to normalize the probe data.

Thomson scattering does not seem to offer a good alternative to interferometry. It has the advantage of measuring the local density, but its detection limit is rather high at 10^{18} m^{-3}. Furthermore, due to the limited physical access to the plasma cavity, it will not be possible to use Thomson scattering to its full potential.

In interferometry, one can choose between several types, like the Michelson, the Mach-Zehnder or the Fabry-Perot. As the Fabry-Perot is the most sensitive of these interferometers, it was decided to design and build a Fabry-Perot, where the plasma is situated in between the mirrors.

The heart of a Fabry-Perot interferometer consists of the two mirrors, forming the optical cavity. For stable operation the optical path length between them should remain constant. This not only requires that the position of the mirrors relative to one another should remain stable, but also that the index of refraction (except for the plasma index, which we want to measure) should be kept constant.

In practice this means that the entire Fabry-Perot should be placed in vacuum, inside the reactor vessel. If the mirrors would be placed outside of the vacuum a layer of atmospheric air would be included within the optical cavity, and the variations in room temperature and air pressure would mask out any plasma effects. Furthermore, the optical losses because of repeated reflections at the vacuum vessel windows would greatly reduce the peak transmission of the interferometer. Another reason for placing the mirrors within the reactor is that this reduces the overall size of the construction, which is advantageous in view of mechanical and thermal stability. The inner dimensions of the etching reactor lead to a mirror separation 20 and 25 cm.

The interferometer will be used to determine and monitor the electron density of a RFI etching plasma, by measuring the refractive index of the plasma. The experimental technique is very sensitive to mechanical and thermal effects, which appear as variations in the electron density. These effects will be discussed in section 7.2.
The characteristics of the interferometer are mainly determined by the shape, reflectance and surface quality of the mirrors, and by their separation and alignment. In section 7.3 the design of the mirrors and the mirror mountings is described. The optical instrumentation is described in section 7.1, while in section 7.4 a scheme is outlined to increase the coherence length by stabilization of the laser frequency. Finally, in sections 7.5, the operating principle of the interferometer is discussed, its measuring range as an electron density diagnostic and its accuracy.

7.1 Optical instrumentation

In chapter 2 and section 6.7 it was demonstrated that for determination of electron densities of the order of 10^{17} m^{-3} or more, infrared light should be used. At the university a Laser Photonics infrared tunable diode laser system is available, which at present has a wavelength range of 5 to 20 µm.

In a diode laser, electrons and holes are trapped within an active layer set between the p and n doped layers of a semiconductor diode. This trapping occurs when the band width of the active layer is smaller than that of the surrounding layers. The electron density in the conduction band is further increased by sending a current through the diode. Above a critical current, population inversion occurs, resulting in laser action. The reflectivity at the polished crystal-air interface is high, and the laser cavity is further bounded by the adjoining layers which have a higher index of refraction.
By varying the crystal composition of the active layer, diode lasers can be made to radiate light with wavelengths ranging from the infrared to the ultraviolet.

A diode laser typically has several modes, with wavelengths determined by the length of the cavity L, and the refractive index of the laser medium n:

$$m\lambda = 2n(T)L \tag{7.1}$$

As the refractive index is strongly temperature dependent, the laser wavelength can be tuned by changing the diode temperature.

In our diode laser system, the temperature is controlled by a combination of liquid helium cooling with electrical heating. Fine tuning can be achieved by varying the current through the diode, which gives a small temperature change due to ohmic heating.
Four different diodes can be used, giving an effective wavelength range of 5 to 20 µm. The temperature can be set to an accuracy of 10^{-3} K, and the current can be controlled with an accuracy of 0,001 mA. The diameter of the laser beam is about 5 mm, and its divergence is approximately 0,1 mrad.
The infrared light is detected by liquid nitrogen cooled MCT detectors, with a dynamic range up to 16 µm. To maintain an acceptable signal-to-noise ratio the maximum attenuation factor due to optical losses is about 10^3; this will prove to be a severe condition in the practical operation of a Fabry-Perot interferometer.

As infrared light is invisible, alignment of the set-up is not trivial. For visual alignment of the optical components, a HeNe laser (λ=632,8 nm) is included in the laser set-up, the beam path of which can be made to coincide with the diode laser beam path.

7.2 Mechanical stability

In the discussion of finesses in chapter 5, it was shown that the separation between the mirrors is a critical parameter in the operation of a Fabry-Perot. Vibrations and thermal instabilities result in a degradation of the instrumental profile, while heating of the interferometer leads to a shift in fringe position, because of thermal expansion.

Because of mechanical and design considerations, the construction materials are mostly metals

and alloys. The thermal stability of a construction is determined by the coefficients of expansion and the thermal inertia of the materials used, as well as by the mechanical configuration. If materials with different thermal inertias are employed, they will not follow temperature changes with the same speed, which can lead to mechanical stress and instability.
The use of low expansion coefficient materials ensures low thermal drift as well as minimal thermal inertia effects. These considerations lead to Invar as the main material for the interferometer. Invar is the commercial name of a nickel-iron alloy of 64% Fe and 36% Ni. With proper thermal and mechanical treatment, its thermal expansion coefficient can be made as low as $1{,}0.10^{-6}$ K^{-1}. This is a factor 10 lower than that of steel, and in fact it is the lowest thermal expansion coefficient of all metals and alloys. The rigidity of Invar is comparable to that of steel, and its tensile strength lies between the values for steel and brass.

7.2.1 Thermal effects

When the plasma is switched on, the electrical power will be dissipated into heat. The vessel as a whole and especially the interferometer ring will be heated by the plasma and expand. The mirror separation will increase and the Fabry-Perot fringe position will shift. This effect has to be separated from the fringe shift due to the electron density. As the time constant of the thermal expansion is much larger than that of the change in refractive index, the plasma effects can be extracted by modulating the plasma (*sanders85*).

There is however an additional problem: in our particular experimental technique the optical path length between the mirrors is held constant by controlling the mirror separation (see section 7.5). This is done by applying a voltage over a piezoelectric element. Thermal expansion results in a slowly increasing mirror separation, which will be compensated by a steady increase in piezo voltage. At low gas pressures however, electrical breakdown can easily occur at higher piezo voltages (see section 7.3.4). For a piezo plate thickness of 1 mm, the safe voltage limit is 120 volt. This corresponds to a maximum piezo thickness variation of 0,1 μm, which defines the upper limit for the thermal expansion of the ring.

Given a mirror separation of 25 cm, an Invar ring would expand 0,1 μm when heated by just 0,4 K. To relax this severe condition, a form of thermal compensation is introduced: the mirrors are mounted on the inside of the ring, with some aluminium, which has a high expansion coefficient (23.10^{-6} K^{-1}), placed between the ring and the mirror. The respective thermal effects of the Invar and aluminium components tend to cancel out and with a proper choice of aluminium thickness a very small effective expansion coefficient can be attained. In computing this aluminium thickness, the expansion of the other components should be explicitly taken into account.
With an 23,7 cm Invar ring, ZnSe mirrors of 3 mm, and a 1 mm piezo element, the change in mirror separation per kelvin as a function of total aluminium thickness becomes:

$$\Delta d[\text{in nm}] = 176 - 24.d_{Al}[\text{in mm}] \tag{7.2}$$

and thermal compensation is attained for a total Al thickness of 7 mm. This thermal compensation relation assumes a uniform heating of the interferometer by the plasma. As the plasma is cold and at low pressure, conduction will be the most important heat transfer process. As the electromagnetic excitation field cannot penetrate far into the plasma, most heat will be generated in the plasma region immediately above the quartz window in the bottom flange. This will be given off to the window and from there the heat will be conducted to the aluminium vessel walls and the interferometer ring. The Invar ring is in more direct contact with the vessel, and the small thermal conductivity of Invar gives rise to a temperature gradient between the ring and the mirror mountings. The expansion of the ring will therefore be relatively larger than that of the other components.

Still, thermal compensation is a valid design consideration as it does reduce the effect of slow variations in room temperature, to which the interferometer would otherwise be extremely sensitive.

7.2.2 Vibrations

Vibrations can be reduced by adopting a solid, symmetrical construction, and using highly rigid materials. Because of the plasma in between the mirrors, the mirrors cannot be connected by straight rods. In the past, a heavy aluminium "C" was employed to minimize vibration effects (*jansen84*).
In our interferometer set-up, we have chosen to use a complete ring of Invar instead, to increase the symmetry of the whole.
The ring sits on three Invar studs, which are screwed to the bottom flange of the vacuum vessel. To isolate the ring from vibrations of the vessel, teflon ball bearings are placed between the ring and the studs. The position of the studs can be adjusted so the balls rest in the centre of holes created in the ring, ensuring a stable equilibrium position for the ring as a whole. The small thermal conductivity of teflon also reduces the effect of heating of the ring by conduction through the vessel walls.

The best way to avoid vibration effects is to avoid sources of vibration and other mechanical instabilities as much as possible. However, as the interferometer is situated within a vacuum vessel, the pumps of the system will be a unavoidable source of vibrations. These vibrations will be harmonic, and even in very rigid system large displacements will occur in case of resonance. A resonance problem can be solved by adding ballast mass to the ring, which will change the resonance frequency of the construction.

Even for small vibrations, care should be taken that all components return to their original equilibrium positions after perturbations. This can be accomplished by applying spring loads against adjustment threads.

7.2.3 The Invar ring

The ring has been cut in one piece from a 9,5 mm thick plate of Invar. Its dimensions are largely dictated by the geometry of the vessel: the inner diameter of the available space for the ring is 23 cm, while the outer diameter is the vessel diameter, which is 26 cm. Some free space should be kept between the ring and the vessel cylinder as that moves up and down to open and close the reactor.
In view of these restrictions, we decided on a ring with outer diameter 250 mm, and inner diameter 222 mm.
On this ring, two Invar plates were placed opposite one another, to accommodate the interferometer mirrors and their adjustment provisions. Each plate was flanked by two protection rods, which can be used to handle the interferometer. These structures were applied to the ring by vacuum-soldering. To remove residual mechanical stresses, the entire ring was subsequently stress relieved by a heat treatment. This resulted in a deformation which was removed by grinding. The grinding procedure led to a small decrease in overall ring thickness. The final rectangular cross section for the ring is 9,5 mm x 14 mm, which should give the structure sufficient rigidity.

As the actual plasma cavity has a smaller diameter than the antenna accommodation in the bottom flange, the mirrors, which stick out above this protuberance, can be placed further inwards. This relaxes the construction demands on the mirror adjustment provisions, which shall be discussed in the next section.

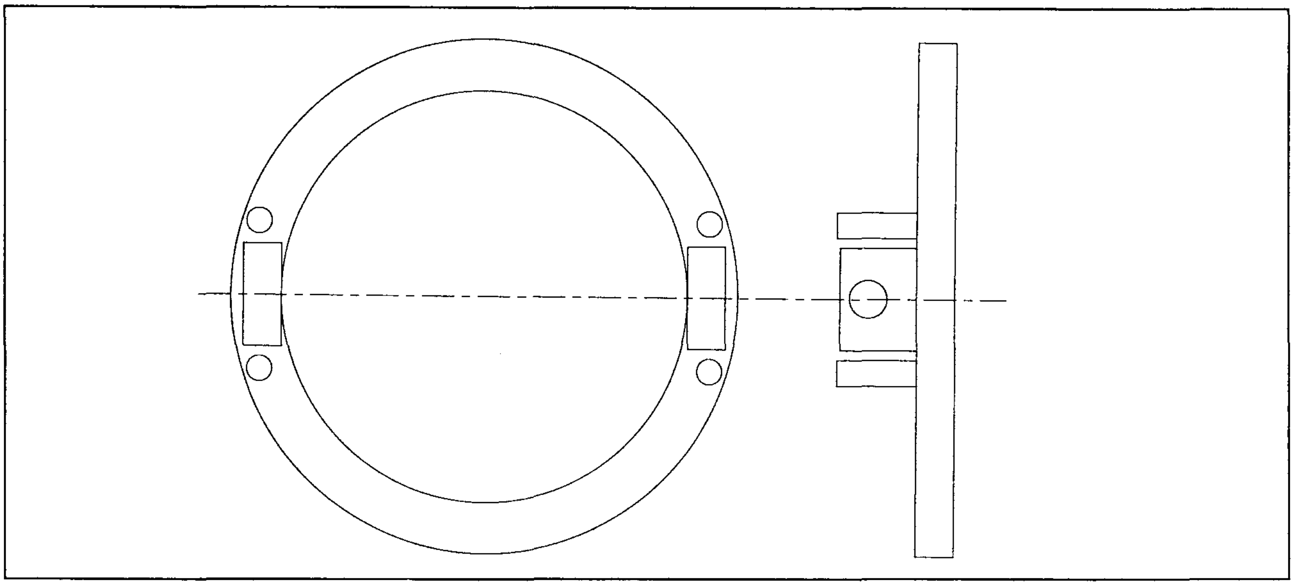

Figure 7.1: Outline of the Invar ring. The mirrors are to be placed on the inside of the central structures

7.3 The Fabry-Perot mirrors

In a Fabry-Perot interferometer high demands are made on mirror quality. They should combine a high reflectance with a finite transmission. When using a thin metal reflecting layer however, reflectance is increased with thickness, but at the same time the transmission decreases due to absorption. Thus for a Fabry-Perot employing metal coated mirrors, a compromise between finesse and signal yield must be found.

Dielectric coatings are not used beacause of their narrow wavelength band; for such mirrors one can combine a high signal yield with a reflectivity close to unity.

Besides the above considerations, the surface roughness of the mirrors should be within a fraction of a wavelength. In an etching plasma environment, the mirror surface should also be chemically inert to prevent damage by reactive radicals.

7.3.1 Mirror materials

Fabry-Perot mirrors are manufactured by working and polishing some substrate material to the desired shape and surface quality, and subsequently depositing a reflecting coating. The substrate material should be stable and hard to allow high precision working.

The condition of finite transmission imposes restrictions both on the substrate material and on the thickness of the reflecting metal layer. Standard optical materials like glass or saphire, become opaque at wavelengths above 2 µm (*optics guide 5, melles griot*), and thus cannot be used as substrates.

ZnSe remains transparent up to 18 µm, it is stable and can be worked to high precision. It is commercially available at relatively low cost. In addition, its transmission extends down to below 600 nm, permitting easy alignment with a visible HeNe laser.

A drawback of ZnSe is that it is soft compared to glass. This means it deforms easily and must be handled very carefully.

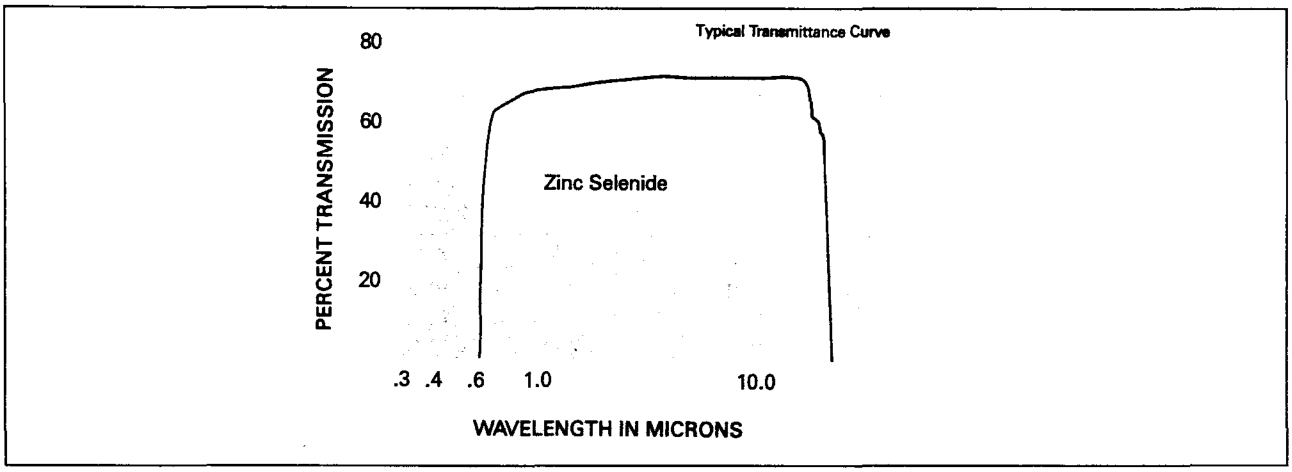

Figure 7.2: transmission of ZnSe (from Optics Guide 5, Melles Griot)

Gold (Au) is chosen for the reflecting coating, as it is chemically inert and gives a high reflectance. The thickness of the gold layer determines both the reflectance and the transmission of the mirrors. Apart from the layer thickness, the reflectance is a function of the real part of the refractive index of gold, while the attenuation is a function of the absorption coefficient, or the imaginary part of the refractive index. These are both highly dispersive quantities, so for each wavelength there will be a different optimum thickness.

7.3.2 Design of the mirrors

Most commonly, flat mirrors are used in Fabry-Perot interferometers, as flat surfaces are easiest to produce with the high precision required. If the mirrors are set far apart however, they have to be set parallel to an extremely high degree, and the divergence of the laser beam must be small. A confocal Fabry-Perot is much less sensitive to errors in parallelism, which appears only as a perturbation of the confocality. Furthermore, the spherical mirrors act as focusing lenses, which reduces the losses due to beam divergence.
As the beam divergence of the diode laser is 0,1 mrad, optical losses preclude the use flat mirrors, and we have to use spherical mirrors.

The separation between the mirrors is dictated by the dimensions of the reactor vessel. To allow room for mirror adjustments screws, the mirrors are set 220 mm apart. A confocal cavity is then created by using mirrors with a focal length of 110 mm, or a radius of curvature of 220 mm.

To maintain spatial resolution the diameter of the mirrors should be kept small. The physical diameter of the mirrors is 10 mm, allowing 0,5 mm of the edge for mounting, resulting in an effective mirror diameter of 9 mm. This is sufficient to accommodate the entire laser beam, which is approximately 5 mm in diameter.

7.3.3 Finesse and optical losses

In designing the interferometer, we initially aimed for a reflectivity finesse $F_r \geq 100$ and a surface defect finesse of $F_d \geq 100$, resulting in a total finesse higher than 60. This defect finesse corresponds to a surface roughness below $\lambda/200$. However, according to the manufacturer, such a high surface quality could not be attained in ZnSe, and we had to settle for a surface roughness of 100 nm, or $\lambda/50$ for 5 μm. This corresponds to a defect finesse $F_d=25$ for 5 μm.

Generally speaking, it is not useful to have a reflectivity finesse that is much higher than the defect finesse. As a rule of thumb, $F_{r,max} \approx F_d$. The available surface quality thus limits the meaningful reflectivity finesse to F_r=25.

However, absorption effects also must be taken into account. Signal level considerations impose a limit on the optical losses in the interferometer: the attenuation factor should be less than 4 orders of magnitude, as stated in section 7.1. The attenuation depends on several parameters: scattering due to surface irregularities, absorption in the mirror substrate and the gold coating, absorption in the plasma, and parasitic reflections.

Neglecting scattering, and assuming the plasma as well as ZnSe to be fully transparent for the wavelengths used, the attenuation is determined by parasitic reflections and absorption within the thin gold layer. Parasitic reflections at the back-sides of the ZnSe mirrors lead to a decrease in transmission of 30% for wavelengths of 5 to 10 µm.

For a confocal Fabry-Perot, a finesse of 25 is achieved by a reflectance R=94%, which corresponds to a gold layer thickness of about 20 nm for 5 µm light. With this coating thickness the mirror would transmit 1,4% of the incident beam intensity. Substituting these values in equation 4.9, and correcting for the back-side reflections, gives a Fabry-Perot transmission of 0,1%. This is just equal to the detection limit.

For a wavelength of 10 µm, a reflectance of 94% corresponds to a gold coating of 15 nm, and a single mirror transmission of 0,91%. The transmission of the Fabry-Perot would then become 0,04%, which falls below the detection limit. In order to maintain a reasonable detector signal level, the coating thickness should be below 20 nm for 10 µm; the reflectivity finesse then becomes F_r=10. Obviously, to attain a high enough transmission at a reasonably high finesse, the 5 µm laser diode should be used.

7.3.4 The mirror mountings

The two mirrors are mounted on the Invar ring, facing each other. Their exact separation can be controlled by varying the position of one of the mirrors with a piezo element, while the other mirror remains fixed.

ZnSe is a soft material and deforms easily, resulting in a distortion of the spherical shape. Therefore the mirrors are placed in square aluminium holders with sides 30 mm, and gently secured by ertalyte caps. The effective aperture of the mirrors is 9 mm, which is smaller than the maximum aperture, as given by eq. 4.55 ($\rho^s \leq 13$ mm for λ=5µm and F_r=25). A central hole of diameter 6 mm is drilled in the holder to allow free passage of the light beam.

Further mounting and aligning is carried out on the holder: at three corners, threaded holes are made to accommodate Invar adjustment screws for alignment of the mirrors. This permits angular adjustment as well as horizontal displacement over a few millimeters.

The mirror holders are made of aluminium to compensate for the thermal expansion of the Invar ring. The holders are 3 mm thick, resulting in a total amount of aluminium of 6 mm, which gives nearly perfect thermal compensation (see section 7.2.1).

To control the mirror separation, a piezoelectric element is placed behind one of the mirrors. A Philips PXE5 grade piezoelectric ceramic is used, which is 1,0 mm thick and has an electrical expansion coefficient of $4,6.10^{-5}$ V^{-1} (*philips93*); its thermal expansion coefficient is $0,5.10^{-5}$ K^{-1} (*philips94*).

The piezo element is cylindrical in shape with diameter 16 mm. Both disc surfaces are coated with silver electrodes to provide good electrical contact. As the light beam has to pass through the piezo element, a 6 mm hole is drilled in the centre of the disc.

The piezo is mounted directly behind the mirror within the aluminium holder. The element is insulated from the aluminium by 1 mm of ertalyte. As it proved to be impossible to solder electrical contacts onto the silver electrodes, the piezo voltage was applied by very thin wires, which were pressed against the electrodes.

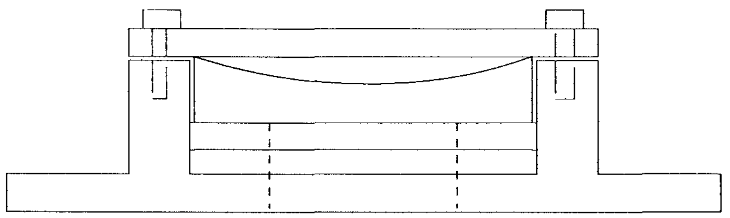

Figure 7.3: aluminium holder including piezo element and insulating layer behind the mirror

Care should be taken to avoid electrical breakdown over the piezo element. At pressures in the mtorr region, a discharge will strike at much lower voltages than at atmospheric pressure. For a given piezo thickness, the breakdown voltage is a function of the gas composition and its pressure. This function has a specific minimum for each gas, which is called the Paschenminimum. As the interferometer will be operated at different pressures, the piezo voltage should be kept below the voltage corresponding to the Paschenminimum.

For argon, the breakdown voltage at the Paschenminimum is above 120 volt (*frouws57*). This corresponds to a piezo expansion of 55 nm. As the voltage can also be reversed in sign, the total piezo length variation becomes 110 nm.

7.4 Laser stabilization

In chapter 3, we saw that the coherence length of the laser should be large compared to the largest optical path length difference between the interfering beams. In a Fabry-Perot, the effective number of interfering beams can be taken equal to the reflectivity finesse, and the maximum optical path length difference is equal to the optical path length difference between succeding orders of interference times the reflectivity finesse.
For a confocal Fabry-Perot with mirror separation 220 mm and reflectivity finesse F_r=25, this becomes:

$$\Delta(OPL)_{max} = 4\,.220.10^{-3}.25 = 22 \text{ m}$$

The stability of the laser, in terms of wavenumber, must then be better than 10^{-4} cm^{-1} (eq. 3.15). To achieve this level of stability in the diode laser system, an external feedback loop is required to control the laser frequency by regulation of the current through the diode.

For this purpose, a second Fabry-Perot etalon is designed, optically identical to the plasma interferometer, but operated in atmospheric air. To reduce the effect of room temperature variations, the entire etalon is enclosed within a thermally isolated box.
With a beamsplitter, part of the laser beam is diverted to the reference etalon. The etalon is tuned to a maximum in transmitted intensity by applying an appropriate piezo voltage. Drifting of the laser frequency results in a change in the piezo voltage. This voltage change is fed back to a control circuit, which subsequently changes the diode current so that the piezo voltage returns to its initial value. The practical implementation of the control circuit will be outlined in the next section.

7.5 Principle of operation

7.5.1 Measuring protocol

A schematic overview of the experimental set-up is given in figure 7.4. The optical components are aligned with a HeNe laser, which can be set parallel to the diode laser beam.

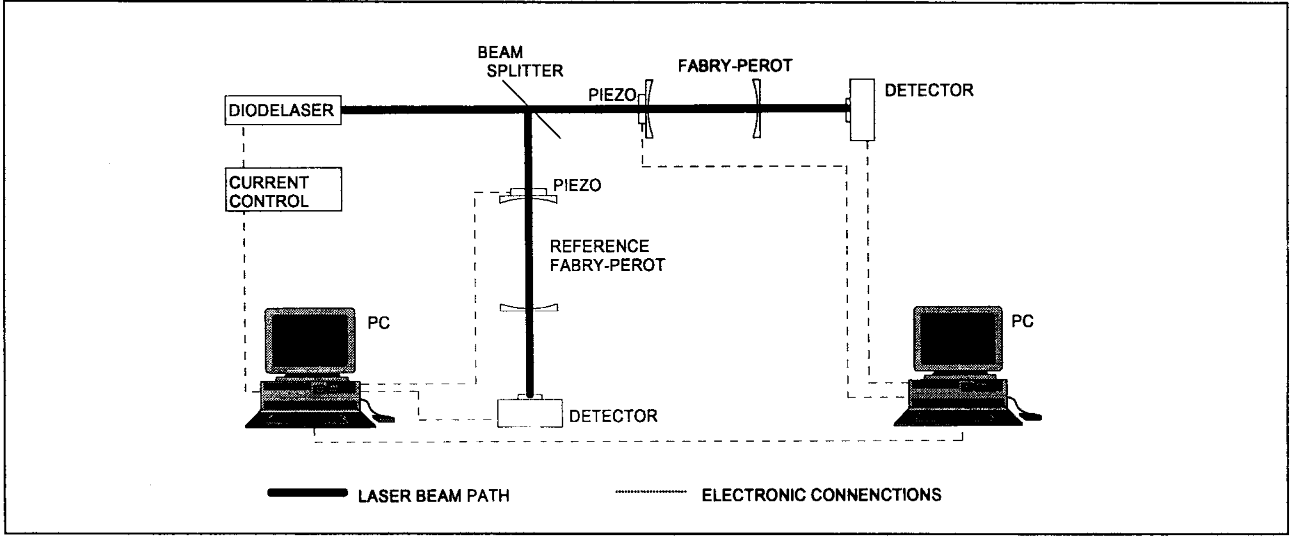

Figure 7.4: experimental set-up

A variation of the plasma electron density results in a change in refractive index. This alters the optical path length of the Fabry-Perot cavity, and the positions of the fringe peaks will shift. As discussed in chapter 5 however, determination of the change in the refractive index from the absolute peak positions gives rise to non-linearities and inaccuracies.
Therefore an alternative technique is adopted: the optical path length between the Fabry-Perot mirrors is kept constant by neutralizing any change in refractive index of the plasma with a corresponding variation of the mirror separation. As outlined in section 7.3.4, the mirror separation can be controlled by the voltage over the piezo element.

To increase the sensitivity, instead of measuring the direct intensity profile, a lock-in technique is used to measure the zero passing of the first derivative. The derivative of the Airy profile is sketched in figure 7.5. The derivative is approximately linear near its zero passing, which corresponds to a maximum in intensity. The slope is proportional to the reduced finesse of the Fabry-Perot.
The frequency of the laser diode is modulated by modulation of the diode current. The detector signal is fed to a lock-in amplifier and the filter frequency of the lock-in is set equal to the modulation frequency. The lock-in output is then proportional to the first derivative of the transmitted intensity profile.

Because of electrical breakdown, the principal Fabry-Perot cannot be scanned over more than 0,1 μm. This is less than the free spectral range for 5 μm light, and the wavelength of the laser will have to be tuned to a fringe peak for the Fabry-Perot.
This can be done by changing the diode current, until a maximum in the transmitted intensity of the Fabry-Perot is found. Once a maximum is found, this laser frequency is locked by the stabilization loop, as described in section 7.4. The dynamic range of the reference Fabry-Perot is much larger as the piezo voltage can be much higher in atmospheric air as in vacuum. Several fringe orders can be scanned and the etalon can always be tuned.

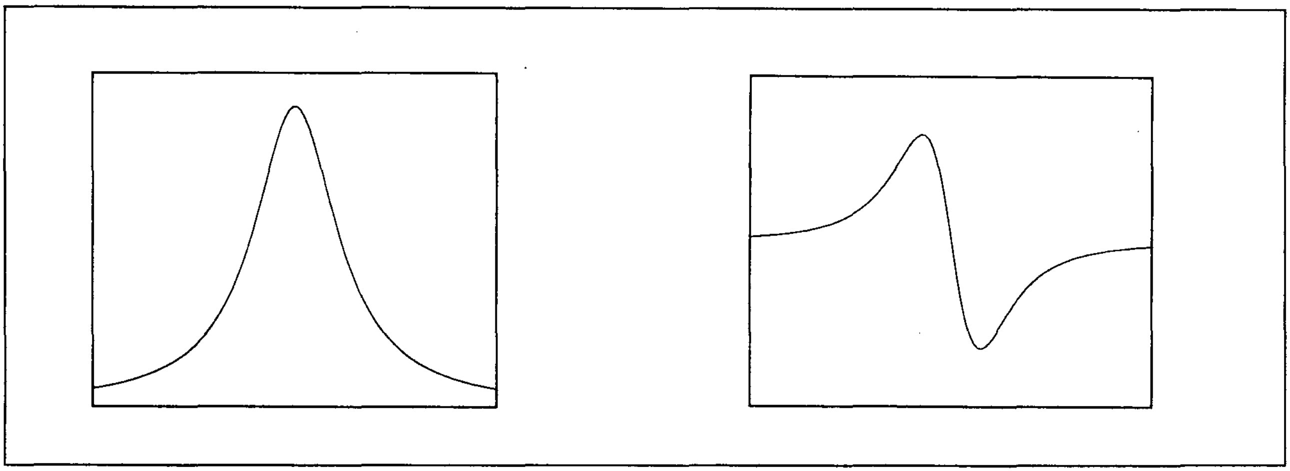

Figure 7.5: Airy profile and its derivative

7.5.2 Electron density detection limit

Adopting the Rayleigh criterion as the resolving limit, we can measure shifts in peak position of the order of the fringe width. This is given by the free spectral range divided by the finesse. Combining equations 2.42 and 4.54, and substituting numerical values we get a detection limit of:

$$\langle N_e \rangle_{min} = \frac{2{,}3.10^{13}}{F}\frac{1}{\lambda_0} \quad [illegible] \quad 10^{20} \quad = \qquad (7.3) \quad (22)$$

For λ=5 μm, the defect finesse is 11, and for a reflectivity finesse of 25, the reduced finesse becomes approximately *F*=9.

This results in a detection limit of 5.10^{17} m^{-3} for λ=5 μm and mirrors with 20 nm gold coating. At this wavelength the contribution of the atomic polarization contribution can be neglected (see section 2.3.1).

The Rayleigh criterion gives a very conservative estimate of the resolving power. Using a lock-in technique and measuring the derivative intensity profile should improve the detection limit by a factor of about 10, making it possible to detect changes in the electron denstiy well below 10^{17} m^{-3}.

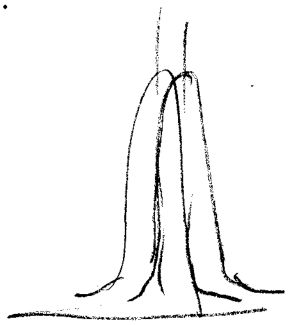

FSR $\frac{o}{4nd}$

$\mathcal{F}$

$\Delta\varphi = c\lambda(\Delta N_e l)$

$\frac{FSR}{\mathcal{F}} = c\lambda(\Delta n_e l)$ in λ,

$(\Delta n_e l) = \frac{1}{\lambda}\,\frac{FSR}{\mathcal{F}}\cdot\frac{1}{c}$

8 What went wrong: the mirrors

In the previous chapter, the design of the Fabry-Perot interferometer and its proposed use as a plasma diagnostic were discussed. Unfortunately, in practice things did not quite work out the way we had planned it. This was mainly due to problems with the mirrors, which had to be customer made to fit our particular demands.
Firstly we had a number of misunderstandings with the dealer, Fairlight, which all in all led to a delay of more than two months. Then, when we finally received the mirrors, they proved to be not according to specifications: the thin gold layer was much too thick, resulting in a negligible transmission. Futhermore, the back-side of the mirrors was extremely rough, leading to high scattering losses. The experiments to measure the transmission and establish the gold thickness are outlined in section 8.1.
By sputtering in Ar gas, which is discussed in section 8.2, we managed to decrease the gold layer thickness to 50 nm, with a good prospect of creating exactly the right thickness.
At that point however, we discovered that the shape of the mirrors was not spherical at all: they were cylindrical. Section 8.3 describes how this was established. No solution could be found for this error in mirror shape, and this proved to be the endpoint of the project.

8.1 Transmission measurements

In our order for the mirrors, a gold layer thickness of 40 nm was specified, corresponding to a reflectivity finesse of 65 at 5 μm, and 67 at 10 μm. The transmission through a single mirror would be 0,17% at 5 μm and 0,07% at 10 μm. The transmission for HeNe light would be 13,1%.

The mirror surface was to be polished to a surface roughness of better than $\lambda/50$ for 5 μm, or 100 nm, over the mirror diameter (10 mm). Because of economic considerations we had decided not to have the back-sides polished as well. As scattering is far less important in the infrared than in the visible range, we did not expect this to be a big problem.

When the mirrors arrived, the Fabry-Perot interferometer was assembled to perform some tests prior to mounting it inside the reactor vessel. However, using the diode laser, we did not manage to get any signal at all with the detector placed directly behind the interferometer. We removed one of the mirrors, thus effectively measuring the transmission of a single mirror. Still, the signal was below the detection limit.

<u>polishing</u>
Such a large attenuation might be caused to scattering losses at the unpolished back-side, and it was decided to polish these. This proved to be quite hard in practice, as we had to very careful not to damage the upper gold coated surface. The top side therefore could not be used to grip the tiny mirror and a pincet had to be used to pinch the sides of the mirror gently. Initially however, we were unable to prevent contamination of the gold surface with polishing particles. This problem was solved by applying a temporary coating of Opticlean over the gold coating. Opticlean is a polymeric fluid originally designed to clean off organic contaminations from optical components. The fluid solidifies after a few minutes, but can easily be removed using a

special sticker. Opticlean was applied, allowed to harden, and then the mirror's back-side was polished. Afterwards the Opticlean, with the contamination, was removed, leaving a pristine gold surface.

This polishing technique is not too accurate and bound to introduce some shape defects in the back-sides. These might result in a small angular misalignment, but as we saw in section 4.4 that is not a big problem for spherical mirrors. It was not possible to achieve a perfect surface for the back-sides, but with prolonged polishing, a back-side surface quality was attained that should give only small scattering losses, especially at larger wavelengths.

However, even with polished mirrors the attenuation was much higher than expected. Measurements with the HeNe laser still showed an attenuation of about 4 orders. Scattering could not be responsible, so these large optical losses had to be caused by absorption within the reflecting gold layer. It was proposed that perhaps this was due to a difference in the optical properties of a thin gold coating from those of bulk gold (see also section 4.1). However, the deviations from bulk structure for thin layers give rise to an increased transmission, instead of a decrease.

Apart from the absorption coefficient, the other parameter governing absorption, is the thickness of the coating. Assuming absorption to be the only loss mechanism, the measured transmission for a single mirror corresponds to a gold coating thickness above 150 nm, which would be a factor 4 higher than specified.

transmission measurement set-up

In order to determine the transmission as a function of gold thickness, a set-up was built, consisting of a HeNe laser, a fixed attenuator, a focusing lens, a pin-diode detector, a lock-in amplifier and a beam chopper. A ridge was made in front of the detector to accommodate the mirror holder and ensure a reproducible mirror position. To avoid multiple reflections within the optical system, the mirror was set to a slight angle. The set-up is outlined in figure 8.1.

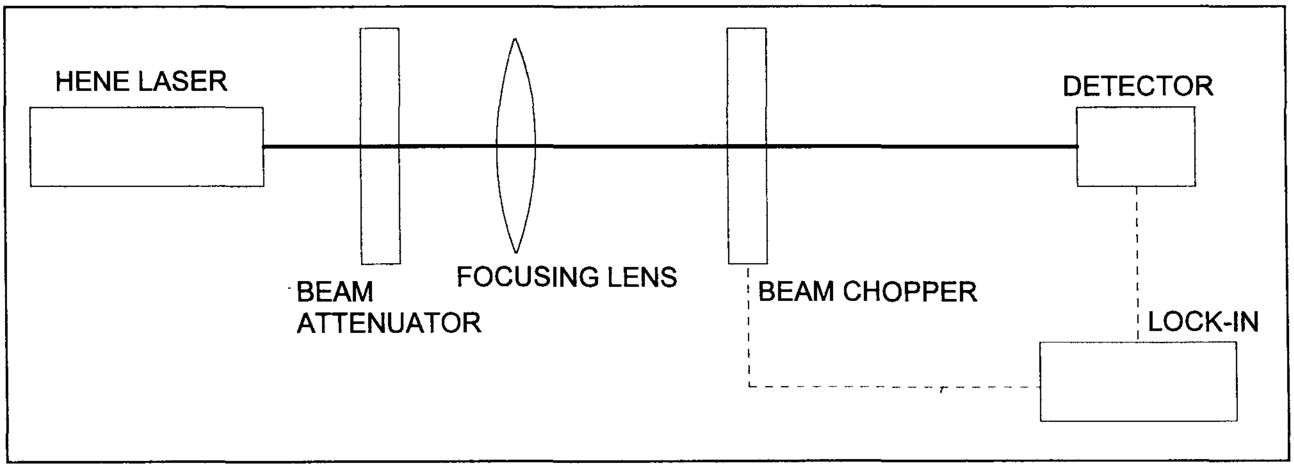

Figure 8.1: experimental set-up for transmission measurements

The laser beam is modulated by the beam chopper, and the corresponding signal of the detector is displayed on the lock-in amplifier. The signal is first measured without the mirror in front of the detector, and then again with the mirror present. The attenuation factor of the mirror is defined as the ratio between these two values.

A single mirror can be modelled by a four-layer system: vacuum-Au-ZnSe-vacuum.

As the thickness of the gold coating is small compared to the wavelength, the interfaces at this layer have to be considered as one system, with a transmissivity and a reflectivity dependent on the gold layer thickness. The thickness of the ZnSe substrate (d=3mm) is large relative to the wavelength, and the transmission at the ZnSe-vacuum interface is 80,2% at 632,8 nm, independent of the other interfaces.

The theoretical transmission for different gold layer thicknesses was computed by a computer simulation of the vacuum-Au-ZnSe interface, using the program ELSIMSPC (*ligthart94*). The values for the refractive index and the absorption coefficients were taken from Palik (*palik85*). By comparing these data to the measured transmission values, after correction for the ZnSe-vacuum interface, the thickness of the gold layer was established.

8.3 Sputtering

To reduce the thickness of the gold coating, low-energy ion sputtering was employed. This gives a uniform erosion of the mirror surface, which is linear in time. Ion sputtering is a stochastical process, which introduces small imperfections in the mirror surface. These are of the order of a nm, which is small compared to the surface roughness, and can therefore be neglected.
The sputtering reactor was a RF driven argon plasma, operated at 50 W power (reflected power was 5 W). The pressure was 50 mtorr, and the argon flow was 40 sccm. The sputter rate was estimated to be approximately 1-3 nm per minute.
The mirror was placed at the centre of the lower electrode, which was large relative to the size of the mirror.

The first mirror was sputtered for 30 minutes, but that proved to be too long: the entire gold coating had been removed. Obviously our estimate of the sputter rate was too low.
A second mirror was subsequently sputtered for 60 seconds, and its transmission was measured. This cycle was repeated, and the cycle time was stepped up to 120 seconds. The first measurements were incorrect due to problems with the settings of the lock-in amplifier, and these were discarded. The results of the transmission measurements for the sputtered mirror are given below:

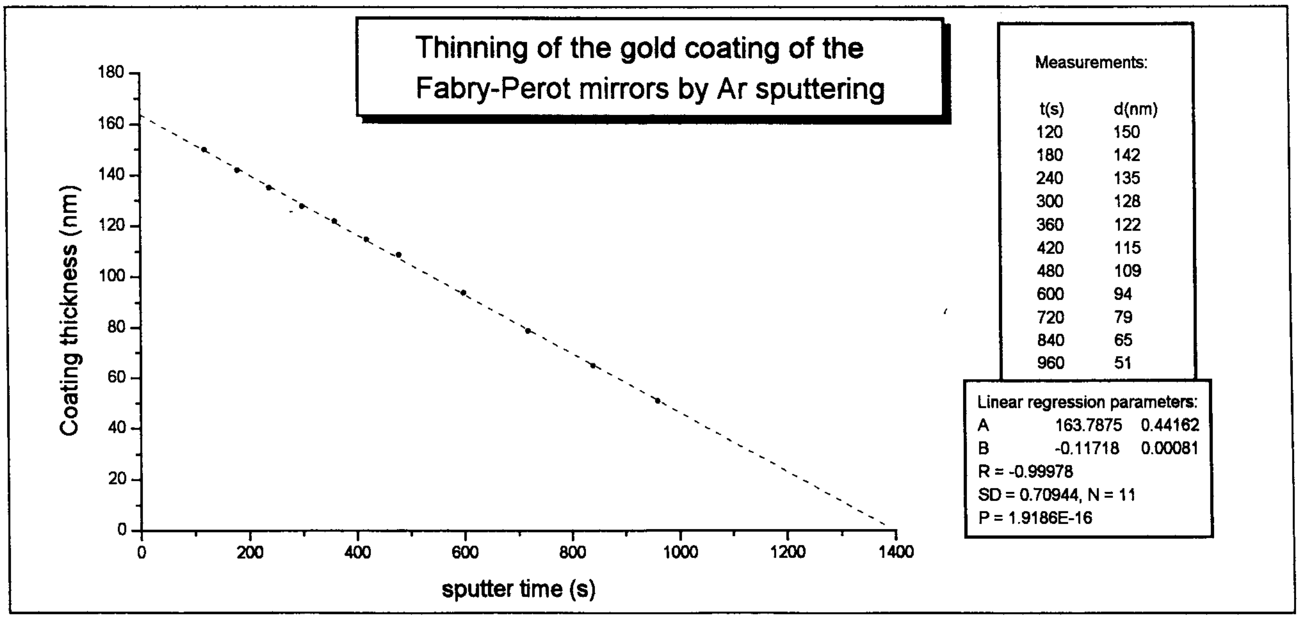

Measurements:

t(s)	d(nm)
120	150
180	142
240	135
300	128
360	122
420	115
480	109
600	94
720	79
840	65
960	51

Linear regression parameters:

A	163.7875	0.44162
B	-0.11718	0.00081

R = -0.99978
SD = 0.70944, N = 11
P = 1.9186E-16

Figure 8.2: gold layer thickness as a function of total sputtering time

The degree of linearity is exceptionally good, and the sputtering process is indeed linear in time, with a sputter rate of 7 nm/min. Furthermore, these results validate the computer simulation used to compute the layer thickness.

Extrapolating the straight line to t=0 gives the original gold coating thickness of the mirror as delivered by Fairlight. This is 160 nm, which is a factor of 4 higher than specified in our order.

8.4 The shape of the mirror

Using the sputtering technique, outlined in section 8.3, it had proven to be possible to make any particular gold thickness. By then we had come to the conclusion that even for the coating thickness originally specified, 40 nm, the infrared transmission would be too low (see section 8.4). To maintain a sufficiently high signal level, a maximum thickness of 20 nm should be used, corresponding to a reflectivity finesse of 29.

During a discussion on exactly how thick the coating should be made, our technician Lambert Bisschops looking by chance at the reflection of a light tube in the mirror observed an asymmetry, which he thought looked like a cylindrical shape error. This was tested more objectively by looking at the reflection of a HeNe laser in the mirror, which was indeed collimated in one direction only, resulting in an elongated spot. Rotating the mirror resulted in a corresponding rotation of the line orientation, and it was concluded that the mirror was not circularly symmetric.

A rigorous examination of the surface shape was performed at the group Precision Engineering at the university, using a Michelson interferometer and a laser profilometer.

The interferogram of an ideal spherical surface should consist of a set of concentric circular fringes, with a decreasing fringe separation away from the centre. Surface and shape defects would appear as a broadening and a deformation of the fringes.
In practice, the interferogram displayed a set of parallel straight fringes. The spacing between the fringes was maximum at the centre of the mirror and decreased towards the edges. As one fringe spacing represents one half wavelength of surface contour variation, this is indicative of a purely cylindrical surface shape.
The surface contour of the mirror was also measured by a laser profilometer, which scans the surface over one dimension. Figure 8.3 shows the surface contour for two orthogonal orientations of the mirror, as measured by the profilometer.

These measurements show conclusively that the mirrors are not spherical at all, but cylindrical. A Fabry-Perot with such mirrors will have essentially different optical characteristics in the two orthogonal planes defined by the optical axis and the cylindrical orientation. Furthermore, because of the "flatness" in one plane, losses due to beam divergence will be prohibitive, as was already noted in section 7.3.
As it is not possible to rework the surface to a spherical shape, we were forced to conclude that these mirrors are unsuitable for our Fabry-Perot interferometer.

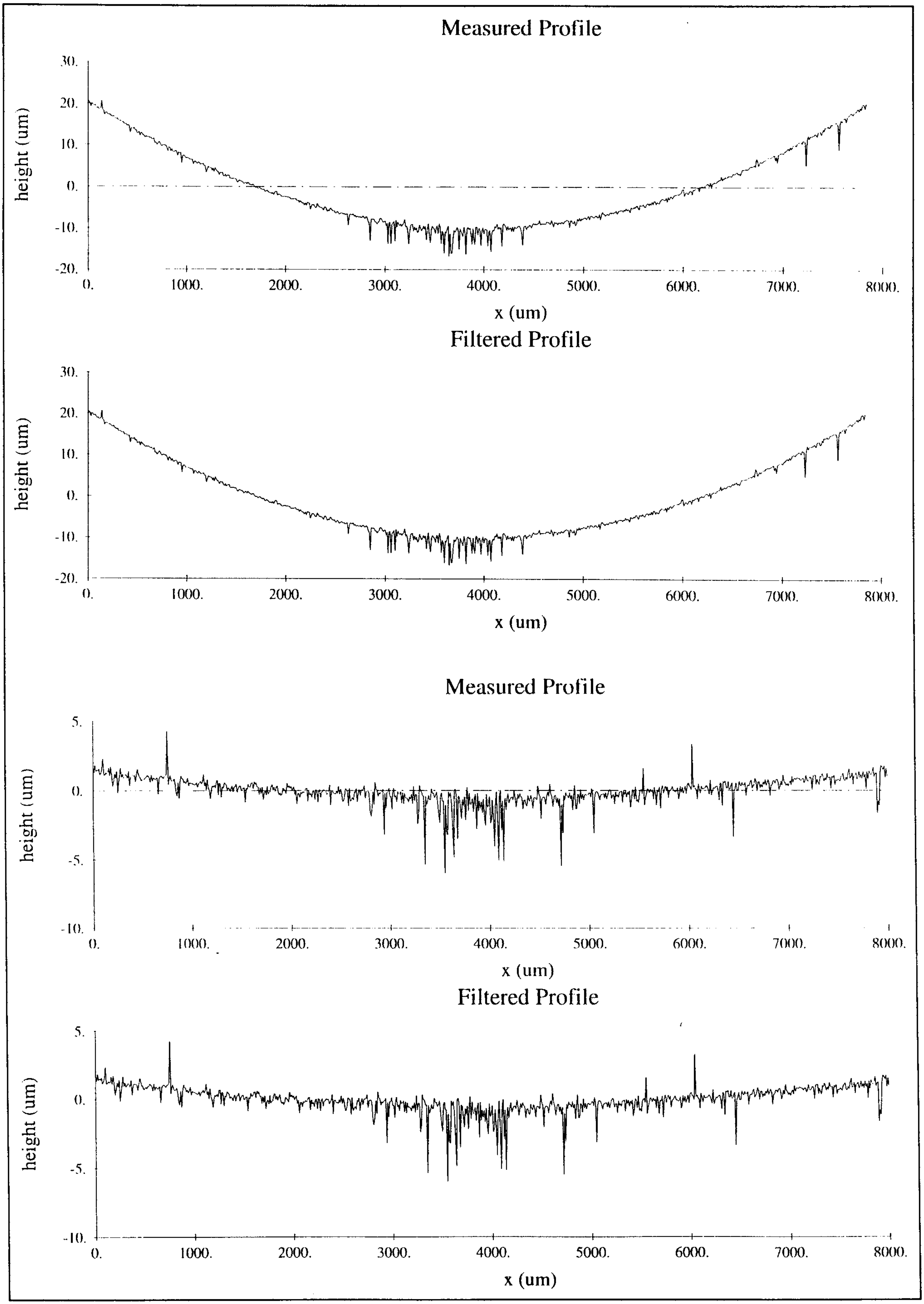

Measured Profile

Filtered Profile

Measured Profile

Filtered Profile

Figure 8.4: contour of the mirror surface in two orthogonal directions

9 Conclusions and suggestions

9.1 Concluding remarks

The fault in the gold coating thickness was due to an error in the production procedure. This was acknowledged by the manufacturer, and they did offer to rework the mirrors to the specified gold thickness.

In contrast to the coating fault however, the cylindrical shape could not be blamed on the manufacturer: in the technical drawing which had accompanied our order, the mirror was indeed drawn as cylindrical by mistake.

As it is not possible to rework the surface in order to change the shape to spherical at the university, the only way to attain spherical mirrors would be to order new ones. In view of the delivery time of approximately two months, it was decided not to order new mirrors, and to finish the project as it was.
This meant of course that, regrettably, nine months of work had not resulted in a functioning plasma diagnostic. Hopefully however, this project will serve as a basis for further research into an optical diagnostic for RFI plasmas.

9.2 Suggestions for further research

In the course of this project it has become clear that the absorption in the gold layer is a major factor in reducing the overall tranmsission of the Fabry-Perot, especially at higher wavelengths.

The electron density detection limit, as given by the Rayleigh criterion of resolving power is (see section 7.5.2):

$$\langle N_e \rangle_{min} = \frac{2,3.10^{13}}{F} \frac{1}{\lambda_0} \qquad (1)$$

For higher wavelengths this improves, because of the increase in λ, but also because surface defects become less important and the resulting finesse increases.

Therefore, it would be advantageous to use 10 μm instead of 5 μm, but for this wavelength the gold absorption is prohibitively high.
This problem can be overcome by using mirrors with a dielectric coating, which display very low absorption, even for high finesses. To achieve some freedom in the wavelength, an appropriate multilayer coating should be used. Of course, care should be taken that the dielectrics are transparent for the wavelengths used.

As the gold coated mirrors we have now are useless for a Fabry-Perot anyway, it is recommended to design new mirrors with a dielectric coating, with a high reflectivity around 10 μm. The reflectivity of these mirrors should be matched to the surface defect finesse available, and for a surface roughness of 100 nm (λ/100 for 10 μm), the reflectivity should be 97%. This should be easy to attain using a multi-layer coating.

The control software for the experimental set-up did provide a user-friendly interface to the set-up, but still suffers from a few minor imperfections. These should be remedied as soon as possible to create an ergonomic laboratory environment.

As for the plasma source, the matching network should be modified to function reliably in automatic mode. Changing the value of the fixed capacitances or replacing some fixed inductance in the network might help.

References

baum75	Interferometric measurement of particle densities in cascaded arcs at atmospheric pressure D. Baum et al, Plasma Physics 17, p79 (1975)
born75	Principles of optics M. Born and E. Wolf 5th ed. Pergamon, New York (1975)
bisschops92	Ets II, beschrijving van experiment en faciliteiten L. Bisschops internal report Eindhoven University of Technology VDF/NG 92-04 (1992)
chen84	Introduction to plasma physics and controlled fusion, volume 1: plasma physics F.F. Chen Plenum Press (1984)
CRC94	Handbook of Chemistry and Physics 1994-1995 CRC Press Inc (1994)
frouws57	Paschen curves in neon-argon mixtures S.M. Frouws in: Proceedings of the third International Conference on Phenomena in Ionized Gases, p341 (1957)
hecht79	Optics E. Hecht and A. Zajac Addison Wesley (1979)
hercher68	The spherical mirror Fabry-Perot interferometer M. Hercher, Appl. Opt. 7(5), p951 (1968)
hopwood92	Review of inductively coupled plasmas for plasma processing J. Hopwood, Plasma sources Sci. Technol. 1, p109 (1992)
hopwood93	Electromagnetic fields in a radio-frequency induction plasma J. Hopwood et al, J. Vac. Sci. Technol. A 11(1), p147 (1993)
hopwood94	Planar RF induction plasma coupling efficiency J. Hopwood, Plasma Sources Sci. Technol. 3, p460 (1994)
hugenholtz90	Microwave interferometer and reflectometer techniques for thermonuclear plasmas C.A.J. Hugenholtz Ph.D. thesis, Eindhoven University of Technology, Dep. of Physics (1990)
hutchinson87	Plasma diagnostics I.H. Hutchinson Cambridge University Press (1987)
jackson75	Classical electrodynamics J.D. Jackson 2nd edition, John Wiley & Sons (1975)

jansen84	Nanometer-interferometrie met een gestabiliseerde HeNe-laser A.W. Jansen internal report Eindhoven University of Technology VDF/NT 84-09 (1984)
kroesen91	Spatially resolved high resolution interferometry G.M.W. Kroesen et al, Meas.Sci.Techn. 2, p293 (1991)
kroesen93	In-situ diagnostics for plasma surface processing G.M.W. Kroesen, F.J. de Hoog, Appl. Phys. A56, p479 (1993)
ligthart94	Simulations of infrared absorption spectra W. Ligthart internal report Eindhoven University of Technology VDF/NG 94-06 (1994)
luhmann84	Instrumentation for magnetically confined fusion plasma diagnostics N.C. Luhmann, Jr. and W.A. Peebles, Rev.Sci.Instrum. 55(3) (1984)
meulenbroeks94	Four ways to determine the electron density in low-temperature plasmas R.F.G. Meulenbroeks et al, Phys. Rev. E 49(3), p2272 (1994)
meuth89	Microwave Diagnostics H. Meuth and E. Sevillano in: Plasma Diagnostics Vol.1, Academic Press (1989)
palik85	Handbook of optical constants of solids E.D. Palik Academic Press (1985)
philips93	Data Handbook MA03: piezoelectric ceramics Philips Components, edition 1993
philips94	Private communication with mr. Van Dijk, service engineer Philips Components (1994)
roosmalen91	Dry etching for VSLI A.J. van Roosmalen c.s. Plenum Press (1991)
rosado81	An investigation of non-equilibrium effects in thermal Ar-plasmas R.J. Rosado Ph.D. thesis, Eindhoven University of Technology, Dep. of Physics (1981)
sanders85	Metingen met een verbeterde Michelson interferometer aan CF4 en Ar RF-ontladingen R. Sanders internal report Eindhoven University of Technology VDF/NT 85-11 (1985)
sambeek93	Massa-opgeloste ionenenergieverdelingen op de elektroden in 13,56 MHz Ar, CF4 en N2 plasma's M. van Sambeek, internal report Eindhoven University of Technology VDF/NG 93-05 (1993)
say73	Electrical engineers reference book M.G. Say Buttersworths (1973)

sijde89	Inleiding plasmafysica B. van der Sijde lecture notes, Eindhoven University of Technology (1989)
snijkers93	The sheath of an RF plasma: measurements and simulations on the ion energy distribution R.J.M.M. Snijkers Ph.D. thesis, Eindhoven University of Technology, Dep. of Physics (1993)
sloggett84	Fringe broadening in Fabry-Perot interferometers Sloggett, Appl. Opt. 23(14), p2327 (1984)
steel83	Interferometry W. H. Steel Cambridge University Press (1983)
stoffels94	Electrons, ions and dust in a radio-frequency discharge E. Stoffels and W.W. Stoffels Ph.D. thesis, Eindhoven University of Technology, Dep. of Physics (1994)
sturrock94	Plasma physics P.A. Sturrock Cambridge University Press (1994)
timmermans82	Inleiding interferometrie en toepassing in de plasmafysica C.J. Timmermans internal report Eindhoven University of Technology VDF/NT 82-20 (1982)
vaughan89	The Fabry-Perot interferometer J.M. Vaughan IOP Publishing (1989)
veron79	Submillimeter interferometry of high-density plasmas D. Véron in: Infrared and millimeter waves Vol.2, Academic Press (1979)

Appendices

Appendix A: Derivation of the RFI plasma excitation skin depth

In RFI plasmas, the electron density is typically above 10^{16} m^{-3}, and the electron plasma frequency will be above 10^{9} Hz. This means the plasma frequency is higher than the frequency of the RFI excitation field, and the electromagnetic field will decay exponentially within the plasma with a characteristic penetration depth.

In chapter 2 the dielectric constant of a plasma was derived:

$$\varepsilon = \varepsilon_0 \left(1 - \frac{\omega_p^2}{\omega^2 + i \nu \omega} \right) \tag{A.1}$$

in which ω_p is the electron plasma frequency and ν the electron-neutral collision frequency, which describes damping in a cold plasma.
The penetration depth is related to the dielectric constant through the imaginary part of the propagation number:

$$\delta = \frac{1}{\mathrm{Im}(k)} = \frac{1}{\mathrm{Im}(\sqrt{\varepsilon \mu \omega^2})} = \frac{c/\omega}{\mathrm{Im}(\sqrt{\varepsilon/\varepsilon_0})} \tag{A.2}$$

As the dielectric constant is complex, computing its square root is not completely trivial. The dielectric constant must be separated explicitly into its real and imaginary parts:

$$\varepsilon = \varepsilon_0 \left\{ \left(1 - \frac{\omega_p^2}{\nu^2 + \omega^2} \right) + i \left(\frac{\nu \omega_p^2}{\omega (\nu^2 + \omega^2)} \right) \right\} \tag{A.3}$$

The imaginary part of its square root then becomes:

$$(\mathrm{Im}(\sqrt{\varepsilon}))^2 = \frac{\varepsilon_0}{2} \left(\frac{\omega_p^2}{\nu^2 + \omega^2} - 1 + \sqrt{ \left(\frac{\omega_p^2}{\nu^2 + \omega^2} \right)^2 . (1 + \frac{\nu^2}{\omega^2}) - \frac{2 \omega_p^2}{\nu^2 + \omega^2} - 1 } \right) \tag{A.4}$$

For RFI plasmas $\omega_p >> \omega$, and this can be approximated by:

$$\mathrm{Im}(\sqrt{\varepsilon}) = \frac{\sqrt{\varepsilon_0} \omega_p}{\omega} \left(\frac{\sqrt{1 + \frac{1}{4} (\nu/\omega)^2}}{\sqrt{1 + (\nu/\omega)^2}} \right) \approx \frac{\sqrt{\varepsilon_0} \omega_p}{\omega} \left(1 - \frac{3}{8} (\frac{\nu}{\omega})^2 \right) \tag{A.5}$$

assuming the collision frequency is small compared to the excitation frequency. The penetration depth then becomes:

$$\delta = \frac{c}{\omega_p} \left(1 + \frac{3 \nu^2}{8 \omega^2} \right) \tag{A.6}$$

In contradistinction to the treatment of polarization processes in chapter 2, the condition $(\nu/\omega)^2 \ll 1$ is not always satisfied for RFI fields, and the equation only holds for cold, low-pressure plasmas. Electron-neutral collisions lead to decrease in conductivity, and the penetration depth should increase with rising pressure, as the electron-neutral collision frequency is proportional to the density of neutrals.

For very low pressures, the plasma can be considered to be collisionless, in which case the penetration depth is given by:

$$\delta = \frac{c}{\omega_p} \qquad \text{A.7}$$

Equation 6 is in marked contrast to the expression derived by Hopwood (*hopwood93*). In my opinion, this is due to the fact that the approximation Hopwood uses for the conductivity which applies for the case $\nu \gg \omega$, instead of $\omega \gg \nu$ (*jackson75 page 287*). In cold, low-pressure plasmas therefore, the equation derived in this thesis is correct, and Hopwood's is not.

Appendix B: The antenna coil inductance

The coefficient of self-induction, or inductance, of a infinitely long solenoid without core material is:

$$L = \mu_0 N^2 A/l \qquad \text{B.1}$$

with A the cross-sectional area of the coil and l the length. If all the dimensions are in metres, the inductance will be in henry.

The inductance of a coil of finite dimensions is less than that given by equation B.1, because the flux will not link all the terms. If the ratio of length to diameter is less than 10, a better approximation is given by (*say73, page 2-37*):

$$L = \frac{6{,}4\,\mu_0 N^2 D^2}{3{,}5D + 8l} . \frac{D - 2{,}25d}{D} \qquad \text{B.2}$$

in which N is the number of coils, and the other dimensions are as set out in the figure. The values for our particular antenna coil are N=3, D=116 mm, d=6 mm and l=35 mm. Equation B.2 gives an approximate inductance for the antenna of:

$$L = \frac{6{,}4 . 4\pi . 10^{-7} . 3^2 . (0{,}116)^2}{3{,}5 . 0{,}116 + 0{,}28} . \frac{0{,}116 - 2{,}25 . 0{,}006}{0{,}016} = 1{,}2\mu H$$

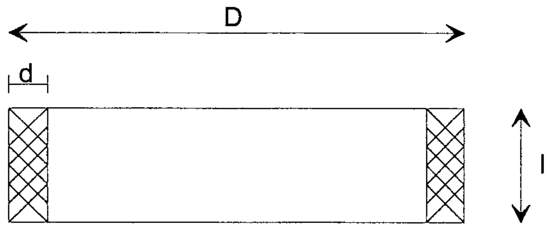

Dimensions in the antenna coil equation

Appendix D: Operation manual for ETS-I

Starting up

Upon switching on, the PC automatically starts up Intouch Windowviewer. This is a dedicated program which visualizes the state of the set-up and controls the set-up through the PLCs; it gives an excellent overview, is user-friendly and mouse-controlled. The program is largely self-explanatory.

Intouch can be toggled between two modes of operation: manual and auto. At this moment only two routines are implemented, pumping down and shutting down. In future more routines may be added, for instance to allow automated plasma control.

In manual mode, the operator has the possibility to control the vacuum system from behind the PC. As yet, it is not possible to control the plasma settings.

Pumping down of the reactor vessel

In auto mode, Intouch has a routine to pump the reactor down to high vacuum. Besides checking whether all the flanges are sealed, and all the pups are connected, this requires no further operator action. Sometimes however, especially when pumping down right after an alarm or shut-down, the routine will not run correctly. This is mostly because of the turbo pump which requires a certain cooling-off period after shutting off. Resetting the pump-down routine (not the computer!), and waiting a few minutes before restarting, normally results in a succesful run.

Plasma generation

When the pressure in the reactor is low enough, plasma can be generated. For this the undermentioned procedure should be followed:

1 Recalibrate the Baratron against the Penning gauge
(1 mbar = 0,76 mmHg)

2 Open the Ar-bottle
(set secondary pressure to 10-15 psi)

3 Open gas valves
(first open the main valve, then open the specific valve)

4 Check whether the valve controller is set at EXT (or AUTO)

5 From Intouch, set the pressure with "Set pressure chamber"

6 From Intouch, set the flow controller to the desired value

7 Check whether the flow and pressure settings are compatible
(if the flow is too low the pressure may drop below the setpoint, if the flow is too high the pressure may rise above it)

8 From Intouch, turn on the RF generator mains power

9 Turn on the matchbox control unit

10 Turn on the power meter

11 Set RF power level on the generator front panel

(using the up and down adjustment arrows)

12 Activate pulsing program (optional)
(see operator's manual of the generator for programming)

13 Switch on RF power on the front panel ("RF on/off")

14 Minimize reflected power with the matchbox controls
(only necessary if the automatic matching does not function properly)

When applying high power levels, the thermal load on the system, and especially on the quartz window and its sealing rings, should always be born in mind. A thermocouple should be placed underneath the window to monitor the temperature. As a maximum temperature, 150 C should be taken, to prevent melting of the plastic rings.

Shutting down the plasma

The procedure for shutting down the plasma is outlined below:

1 Turn off RF power on generator front panel ("RF on/off")

2 Turn off the powermeter

3 Turn off the matchbox control unit

4 From Intouch, turn off the Rf generator mains power

5 From Intouch, set flow control to zero

6 From Intouch, close the gas valves
(first close the specific valve, then close the main valve)

7 From Intouch, set pressure chamber to zero

8 Switch the valve controller to MANUAL and set switch to OPEN
(this prevents damage to the throttle valve should the system be exposed to atmospheric shock)

9 Close the Ar-bottle
(always close the bottle to prevent loss of gas due to small leaks)

Opening the reactor vessel

To ensure a good vacuum quality, the reactor should be kept at vacuum as much as possible. It should only be brought up to atmospheric pressure in case of prolonged disuse or to open the vessel.
An automated routine is included in Intouch to bring the system back up to atmospheric pressure. The system is vented with nitrogen gas, and the operator should check beforehand that the nitrogen bottle is not empty or closed.

Following these procedures strictly, might help against forgetting small but sometimes important details, but it can never be a substitute for common sense!